UNIVERSITÀ DEGLI STUDI DI ROMA "TOR VERGATA"
DIPARTIMENTO DI FISICA
DOTTORATO DI RICERCA IN FISICA (XXX CICLO)

PH.D. THESIS

Development of the control and data handling software for the High-Energy Particle Detector and preliminary data analysis

CANDIDATE:
Alessandro Sotgiu

SUPERVISOR:
Prof.ssa Roberta Sparvoli

COORDINATOR:
Prof. Roberto Benzi

A.A. 2017/18

Author's address:

Dipartimento di Fisica
Università degli Studi di Roma "TorVergata"
Via delle Ricerca Scientifica, 1
00133 Roma
Italia

Introduction

The present thesis summarizes my activity as a PhD student in the framework of the China Seismo-Electromagnetic Satellite (CSES) experiment and in particular of one of its scientific payloads, the High-Energy Particle Detector (HEPD).

The CSES space mission involves an international collaboration between China and Italy and aims at monitoring the perturbations originated by electromagnetic emissions in the ionosphere, magnetosphere and in the Van Allen radiation belts, and at investigating possible correlations with seismic events. For these purposes, the Chinese satellite houses several instruments for the measurement of the electric and magnetic field components, the measurement of plasma disturbances and the measurement of energetic particle fluxes and spectra.

The HEPD is the only non-Chinese scientific payload and was developed by the Italian components of the CSES mission (CSES-Limadou collaboration). Four models were developed (Electrical Model, Structure and Thermal Model, Qualification Model and Flight Model) in order to test and verify the final performances and capabilities of the apparatus. People participating to the design and realization of the HEPD belong to various sections of the Italian National Institute for Nuclear Physics (INFN) and Physics Departments of Italian Universities.

The HEPD detector is composed by a set of subdetectors designed to measure electrons, protons and light nuclei fluxes with the possibility to discriminate the extra-galactic component from the trapped component of the cosmic rays by means of a precise reconstruction of the incident particle direction. For this reason, the subdetectors that compose the HEPD are a silicon tracker, a trigger plane, an electromagnetic calorimeter and a veto system. The instrument is optimized to study electron and proton fluxes in the energy range from 3 MeV to 100 MeV and from 30 MeV to 200 MeV respectively.

The final space qualification campaign of the Flight Model of the apparatus was completed in October 2016, and was followed by performance tests with electron and proton beams. After this, the apparatus was delivered to the DFH Company Ltd. in Beijing (China) for the integration on board CSES.

The satellite is scheduled to be launched from the Jiuquan satellite launch center in the Gobi Desert (inner Mongolia, China), by the Chinese rocket Long March 2C, in February

2018.

The Author's Contribution

During the three years of my Ph.D. course, I participated to the development of the HEPD detector with several contributions.

I started working in the CSES-Limadou collaboration during a post degree fellowship from January 2014 to October 2014, focused on the realization of the Electrical Model of the High-Energy Particle Detector (HEPD). In this period, I started the development of the software for the communication between our detector and the Chinese satellite and participated to the realization of the Electrical Ground Support Equipment (EGSE) for the emulation of the CSES satellite.

At the beginning of my Ph.D. course, I continued this work and personally tested the software of the HEPD-EM, at first in Rome by means of the EGSE, and later in Beijing at the DFH Company, responsible of the CSES satellite construction.

In the following period, I started working on the implementation of a Monte Carlo software with the Geant4 tool-kit. I simulated the geometry of the HEPD detector in its Flight Model version, including most of the mechanical structures, and studied the performances such as the energy resolution and the geometrical factor.

I was also involved in the design phase of the electronics for the Flight Model of the HEPD, in particular for what concerns the DAQ board and the use of the Digital Signal Processor, whose functionalities are the data compression, the calibration of the silicon and scintillator detectors and the transmission of the data to the satellite. I personally developed the software for the DSP of the DAQ board and I contributed to the development of the CPU software regarding the definition of the in-flight operations and working procedures and the implementation of the communication protocols with the satellite.

From January 2014 to September 2016 the Qualification Model (QM) and Flight Model (FM) of the detector were realized and assembled. I participated to the optimization, test and integration, at first for the electronics subsystem, and finally of the whole apparatus, in the laboratories of the 'Roma 2' INFN Section at the 'Tor Vergata' University in Rome (Italy), where all the subsystems were assembled together.

During these months, I was engaged in the space qualification and acceptance tests for both the QM and the FM models. These tests included the mechanical qualifications, the thermal balance and the thermal-vacuum tests required to verify the ability of the detector to survive strong accelerations during the satellite lunch and the temperature conditions present in the low earth orbit. In particular, during the thermal and thermo-vacuum tests, I was in charge of the software procedure definition, the implementation of these procedures within the electrical ground support equipment and the preliminary data analysis to monitor the detector status after the tests. These acceptance tests were performed at the SERMS laboratory in Terni (Italy), where thermal-vacuum and thermal chambers are available, as well as shakers for any type of vibrational tests.

In October and November 2016 two beam tests were carried out with electrons (Beam Test Facility, Frascati, Italy) and protons (Proton Therapy Center, Trento, Italy) to characterize the FM of the apparatus and determine the performances and the experimental characteristics of the HEPD.

Once completed the beam tests, I performed an analysis on the collected data and on some cosmic-ray data acquired in the INFN Roma 2 clean rooms after the final assembly of the FM. This preliminary analysis, partly reported in this thesis, was mainly focused on the optimization of the in-flight data handling software.

During the last months of my Ph.D., I started working on the event reconstruction software and on the development of a pipeline for the HEPD data processing and storage. The pipeline was designed to produce immediately usable HEPD data (called level2) starting from the raw data (downlinked from the satellite) and to store them in a database. The reduction from the raw data (including for example the ADC counts of the subdetectors and all the configuration information), to the level2 data, that contains a higher level information such as the energy released in each plane of the detector or the particle arrival direction, foresees the calibration of the subdetectors and a precise knowledge of the detector response. At the moment of the writing of this thesis, I am still working on the level2 data reconstruction with the rest of the Limadou collaboration.

Outline of the Thesis

The first two chapters of the present thesis are a general introduction to the CSES mission and the HEPD detector. Chapter 1 illustrates the scientific objectives of the mission and a description of CSES, including the other scientific payloads on board the satellite. A brief introduction of the ionosphere environment and trapped particle motion is reported as well. The last sections are dedicated to the HEPD physics and the presentation of correlated results from previous experiments.

Chapter 2 is dedicated to the description of the HEPD apparatus in its Flight Model. The subdetectors that compose the apparatus are described in dedicated sections.

Chapter 3 deals with the HEPD electronics, with specific attention to the DAQ board to whose design and tests I contributed, and to the Digital Signal Processor.

Chapter 4 is focused on the main part of my personal contribution. The chapter contains the description of the online software (the CPU control software and the DAQ data handling software), that I personally developed and tested. The chapter is divided into main sections, with a description of the software developed for the Digital Signal Processor of the CPU board and the software developed for the DSP of the DAQ board.

Chapter 5 concerns the description of the vibration, thermal-vacuum and thermal tests the Qualification Model and the Flight Model of the HEPD underwent in order to complete the space qualification and acceptance campaign. It also describes two preliminary methods I developed for the data analysis, in order to correct the response of the silicon detector (independently on the hit position of the incident particle) and to equalize the response of the scintillator detectors. This preliminary analysis was performed on data acquired during the proton beam test and on cosmic-ray data collected when the detector was assembled in the Roma 2 laboratory.

Contents

List of Figures

List of Tables

Chapter 1

The CSES Mission

The CSES (China Seismo-Electromagnetic Satellite) mission is a scientific program dedicated to monitoring electromagnetic field and waves, plasma and particle perturbations of the atmosphere, ionosphere and magnetosphere induced by natural sources and anthropocentric emitters, with the aim to study their correlations with the occurrence of seismic events. More in general, the CSES mission will investigate the structure and the dynamics of the ionosphere, the coupling mechanisms with the lower and higher plasma layers and the temporal variations of the geomagnetic field, in quiet and disturbed conditions. Data collected by the mission will also allow to study solar-terrestrial interactions and phenomena of solar physics, namely Coronal Mass Ejections (CMEs), solar flares and cosmic-ray solar modulation.

The launch of CSES is foreseen for February 2018, from the Jiuquan Satellite Launch Center located in the Gobi Desert, Inner Mongolia, by means of a Long March 2C Chinese rocket.

The first chapter of this thesis presents the general characteristics of the CSES satellite and an overview of the CSES mission, with particular attention to the Italian High-Energy Particle Detector and its scientific objectives.

1.1 Overview

The CSES mission is part of a collaboration program between the China National Space Administration (CNSA) and the Italian Space Agency (ASI), and developed by China Earthquake Administration (CEA) and Italian National Institute for Nuclear Physics (INFN), together with several Chinese and Italian universities and research institutes. CSES is the first satellite of a space monitoring system, proposed in order to investigate the ionosphere with the most advanced techniques and equipment and designed in order to gather world-wide data of the near-Earth electromagnetic environment.

The lithosphere-atmosphere-ionosphere coupling is a complex subject involving many physical effects and interactions that occur from the Earth surface up to the magnetosphere. The investigation of such coupling mechanisms, and in particular of the partially unknown behaviour of the iono-magnetosphere transition region, is of fundamental importance for Earth remote sensing, monitoring of the near-Earth electromagnetic environment and studying of natural hazards. A great part of these effects is caused by natural non-seismic and anthropogenic electromagnetic emissions, but of particular relevance are the electromagnetic disturbances associated with the seismic activity that can produce ionospheric perturbations as well as the precipitation of particles from the Van Allen belts, observed before, during and after earthquakes of medium and strong magnitude. All of these phenomena must be distinguished from those induced by sources external to the geomagnetic cavity and by atmospheric events. In fact, an important role in controlling the dynamics of the topside ionosphere is played by the Sun that generates (regular and irregular) variations of the lithosphere-ionosphere-magnetosphere parameters by impulsive events as solar coronal mass ejections and solar flares, as well as by tropospheric activity (for example lightning). Many experimental observations have been performed and theoretical models have been proposed in order to analyse and discriminate ionospheric disturbances caused by natural terrestrial events, such as earthquakes and volcanic eruptions, and by anthropogenic activities.

The study of the physical conditions which give rise to an earthquake, as well as of the processes that precede a seismic rupture, constitutes the basis of earthquake prediction approaches. An original way, in order to study seismic precursors, is to carry out measurements of the ionospheric anomalies by instruments installed on board satellites. Currently, only the dedicated DEMETER French mission (2004-2010) has collected detailed data; other previous results were obtained by analysing observations of some not dedicated space experiments.

The main objectives of the CSES mission is to study the ionospheric disturbances induced by seismic activity and earthquake preparation mechanisms. It is based on long-term systematic and detailed measurements performed by specifically designed detectors. In particular, the mission aims at analysing the temporal correlation between seismic events and the occurrence of electromagnetic perturbations in the upper ionosphere and precipitations of Van Allen particles. Furthermore, CSES will provide important information on ionosphere parameters and on the unknown behaviour of the ionosphere-magnetosphere transition region, in order to develop physical models of lithosphere-atmosphere-ionosphere coupling mechanism.

The CSES mission will also monitor the solar impulsive activity and cosmic-ray solar modulation, by detecting proton and electron fluxes from a few MeV to hundreds of MeV. In fact, the solar activity varies strongly with time (approximately over 11 years) from a minimum level, when the Sun is quiet, to a maximum of activity. Cosmic rays of galactic

origin respond to this activity, that significantly modifies the original differential spectra depending on particle energy, species, sign of charge and time, when measured at Earth. The resulting solar modulation effect is evident in neutron monitor data, showing a clear anti-correlation between particle intensities and solar activity. Particles with rigidities up to at least 30 GV are mainly affected and the effect becomes progressively larger as the rigidity decreases. The solar activity is also characterized by a number of transient phenomena such as solar flares (i.e. sudden flashes of particles observed on the Sun's surface) and coronal mass ejections (i.e. a huge amount of matter and magnetic field emitted by the solar corona). The ejected particles can be accelerated at an energy ranging from a few tens of keV to a few GeV (Solar Energetic Particles - SEP) and escape the Sun's magnetic field; transported through the heliosphere they can reach the Earth causing geomagnetic storms by interacting with the outermost layers of the magnetosphere. The CSES measurements will provide an extension up to very low energy of the range of the particle spectra that are monitored, by the PAMELA and AMS experiments, in the current 24th solar cycle. It will also be possible to compare the measured spectra with those from other space missions, such as GOES and ACE.

The data will contribute to provide an observational sharing service for the scientific community.

1.2 Science Background and Scientific Objectives of the Mission

Earthquakes are one of the most dangerous natural disasters. Very strong earthquakes happen approximately 20 times a year over the globe. The energy released by such earthquakes in several minutes is comparable with the energy produced by a big nuclear explosion or by the greatest electric power plants during a year.

An earthquake is a deformation, fracture, structure and phase transformation event which releases suddenly a large amount of the elastic energy stored in the medium (Earth's lithosphere) and is accompanied by a substantial fraction of energy radiated as seismic waves. To quantify the size of the earthquake, seismologists use the concepts of magnitude (M) and energy release (E). The relationship between the magnitude, determined from seismic surface waves M_s, and the energy (in erg) was given by Gutenberg and Richter:

$$logE = 1.56M_s + 11.8. \tag{1.1}$$

They also proposed the relation between the earthquake size and the frequency of occurrence, in the form:

$$logN = a - bM_s, \tag{1.2}$$

where N is the number of earthquakes with magnitude in a fixed range around magnitude M_s, and a, b are constants.

There are many models and interpretation on the problem of how earthquakes take place. All of them suppose that the fracturing of the rock is preceded by accumulation of deformation in the fault zone. The strain increase is accompanied by other natural phenomena in the vicinity of the preparing fracture which are the so-called earthquake precursors. These precursors include the seismogenic electromagnetic emissions (SEMES) that are one of the most significant earthquake precursors and can be studied with both ground based and spacecraft experiments.

The EMEs of seismic origin are presumably connected to lithospheric earthquakes (i.e. seismic events which occur in the elastic lithosphere). The most reliable models describing EME generation mechanisms invoked effects as piezoelectricity, piezomagnetism and electrokinetic effects.

Piezoelectricity is a property that arises from the crystal anisotropy of the material. A piezoelectric substance shows an electromagnetic response against mechanical stimulations on electric polarization caused by deformation of the crystal lattices. Similar to piezoelectricity, the piezomagnetism consists of the magnetization of a material obtained by applying a stress to the crystal. Furthermore in the earthquake preparation phases, crustal deformation and fracturing processes occur, causing a change of porosity, that causes a change of fluid motion and of the associated electric current. The electrokinetic phenomena are related to the existence of a double layer formed at a solid liquid interface where the ions are held to the solid and a mobile layer extending into the liquid. The difference of the electrical potential between the solid-liquid interface and the bulk of the liquid is the so-called electrokinetic potential.

During their propagation through the solid crust, the higher frequency content of the seismic EME waves are attenuated and only the ULF/ELF (Ultra Low Frequency/ Extremely Low Frequency) waves are supposed to reach the Earth's surface and propagate further into the near Earth space. In particular, if the hypocenter is at a depth of 10 km from the ground surface, only ULF ($\omega \simeq 10$ Hz) can reach the Earth's surface with an attenuation less than 10 dB. Furthermore, an important source of background are the perturbations in the ionosphere caused by the EMEs with an anthropogenic origin. For example, ground-based transmitters in the 10-20 kHz (VLF frequencies) are used for radio-navigation and communications and their strongest interaction region is around the geomagnetic equator. Also the broadcasting stations, at HF frequencies, utilise powerful transmitters which can heat the ionosphere and change the temperature and the density.

The interaction of these EMEs with the ionospheric environment can cause different

kinds of perturbations, in the plasma component as well as in the electromagnetic field and trapped particles in the Van Allen radiation belts.

These belts are zones of energetic charged particles, most of which originate from the solar wind, that are captured by the Earth's magnetic field. The Earth has two such belts (inner and outer) that extend from an altitude of about 500 to 58000 km above the surface. They are mainly composed of energetic electrons (1 MeV $<$ E $<$ 50 MeV) and ions (10 eV $<$ E $<$ 1 GeV) which move along the field lines and oscillate back and forth. The trapping mechanism arises from the interaction between the moving energetic charged particles and the static geomagnetic field. The motion of trapped particles is assumed to be as a superposition of three periodic motions: a gyration around the local magnetic field lines, a bouncing along field lines between conjugate mirror points in the northern and southern magnetic hemispheres, and a drift around the Earth. Adiabatic invariants, that are conserved under the condition of small magnetic field variations during the period of the motion, and in absence of energy loss, nuclear scattering and radial diffusion, are associated with each type of motion the particle can perform.

The first adiabatic invariant is the magnetic moment μ that is associated with the cyclotron motion of particles around the geomagnetic field (see Fig. 1.1 (a)). The gyrofrequency, or cyclotron frequency ω_B of a charged particle q with mass m in a magnetic flux density B, and the corresponding radius of gyration (gyroradius) r_B are defined as:

$$\omega_B = \frac{qB}{m}$$

and

$$r_B = \frac{mv_\perp}{qB},$$

where $v_\perp$ is the particle velocity normal to the field line.

The second adiabatic invariant, called *integral invariant*, is associated with the oscillation or bouncing motion with a certain bounce frequency (see Fig. 1.1 (b)) of particles between mirror points and along the magnetic field. Since the Lorentz force is perpendicular to the velocity, it cannot change the energy of a charged particle moving in it. Thus the particle's kinetic energy, and so the magnitude of the total velocity, remains constant. In the approximately dipole field of the Earth, the magnitude of the field is greatest near the magnetic poles, and least near the magnetic Equator. Because of the constance of the magnetic moment defined as:

$$\mu = \frac{mv_\perp^2}{2B}, \tag{1.3}$$

when the particle moves toward the poles (increasing B), the velocity component transverse to the field increases. As a consequence, the velocity component parallel to the local field must decrease. The mirror points are the positions where the particle's

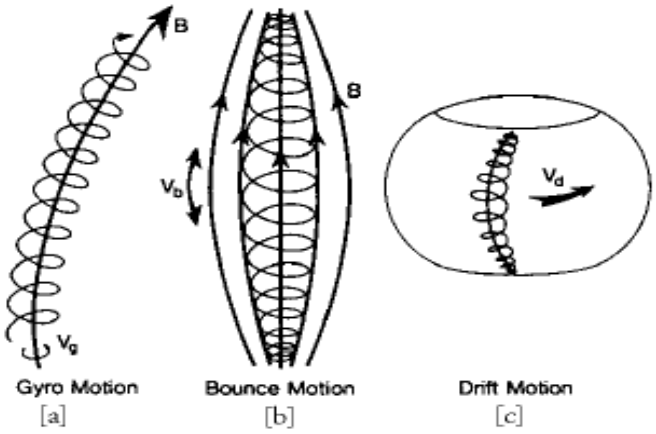

Fig. (1.1) *The trapped particle motion is a superposition of three different motions: the gyro motion around the magnetic field line (a), the bouncing motion along the magnetic field line (b) and the drift motion around the Earth (c).*

velocity vector in the direction of the field reaches zero, and the particles reverse their motion.

If the particles strike the top of the atmosphere during this bouncing motion, they can be scattered by atoms in the air, lose energy and be lost from the radiation belt. For a given particle, the position of the mirror point is determined by its *equatorial pitch angle* defined as follows:

$$\alpha_{eq} = tan^{-1}\frac{v_{\perp}}{v_{\parallel}}.$$

This is the angle between the velocity direction and the magnetic field line, calculated in the equatorial plane (see Fig. 1.2). It is possible to define a *loss cone* as all the equatorial pitch angle values for which the mirror points lie too deep in the atmosphere and the corresponding particle will be lost.

The third kind of motion is the particle drift around the Earth. This is caused by a gradient in the geomagnetic field intensity which provokes a change in the gyration radius, giving rise to a lateral shift of the orbit with opposite direction for positive and negative particles (see Fig. 1.1 (c)).

The anomalous particle fluxes detected by several space experiments in coincidence with earthquake occurrences, are thought to be due to ULF/ELF EME interaction that can cause the precipitation of the trapped particle in the Van Allen radiation belts. A possible diffusion mechanism is the bounce resonant interaction between ULF Alfven waves of seismic origin and particles that have bouncing frequencies in the ULF band (i.e. electrons with E $>$ 1 MeV and proton with E of the order of some tens of MeV). When the bouncing frequency and the wave frequency match, the particle experiences the wave electric field E at every passage in the perturbed zone. This produces a variation

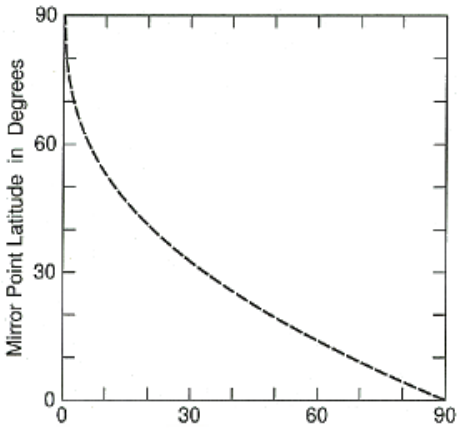

(a) *Latitude of the mirror point as a function of the equatorial pitch angle in degrees.*

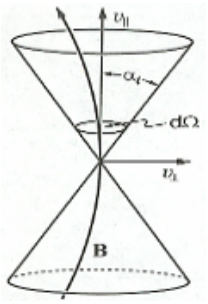

(b) *Equatorial loss cone. If the equatorial pitch angle is inside the loss cone, the mirror point lies too deep in the atmosphere and the particles will be absorbed by collision with atoms.*

Fig. (1.2) *Mirror point position and equatorial loss cone.*

$\Delta\alpha$ in the particle pitch angle that can cause a lowering of the mirror points and, as a consequence, the precipitation of the affected particles. An estimation of $\Delta\alpha$ is given by Akeshina et al.[6]. A qualitative representation of the phenomenology is described in Fig. 1.3.

The CSES mission aims to establish a space-based observation system for detecting electromagnetic anomalies and ionosphere perturbations. For this purpose, several payloads are installed on board the satellite, such as two particle detectors sensitive to particles bursts. The big advantage of satellite experiments, in contrast to ground experiments, is the possibility to cover most seismic zones of the Earth, increasing the statistics because of the much larger number of events that can be recorded.

1.3 The Italian Contribution: CSES-Limadou

Italy participates to the CSES satellite mission with the Limadou[1] project, funded by ASI (Italian Space Agency), in collaboration with different INFN (Italian National Institute for Nuclear Physics) Divisions (Bologna, Naples, Roma Tor Vergata and Trento), the INGV (Italian National Institute of Geophysics and Volcanology), the INAF-IAPS (Italian National Institute of Astrophysics and Planetology) and several Italian Universities.

The Italian contribution to the mission consists in the realization of the High-Energy Particle Detector (HEPD) in four different models, and the support to the development of the Electric Field Detector (EFD). The INAF-IAPS "Plasma Chamber" in Rome was also

[1]Limadou is the Chinese name of the Italian Jesuit priest Matteo Ricci (1552-1610), who performed a lot of missionary works in China at the end of the 16th century.

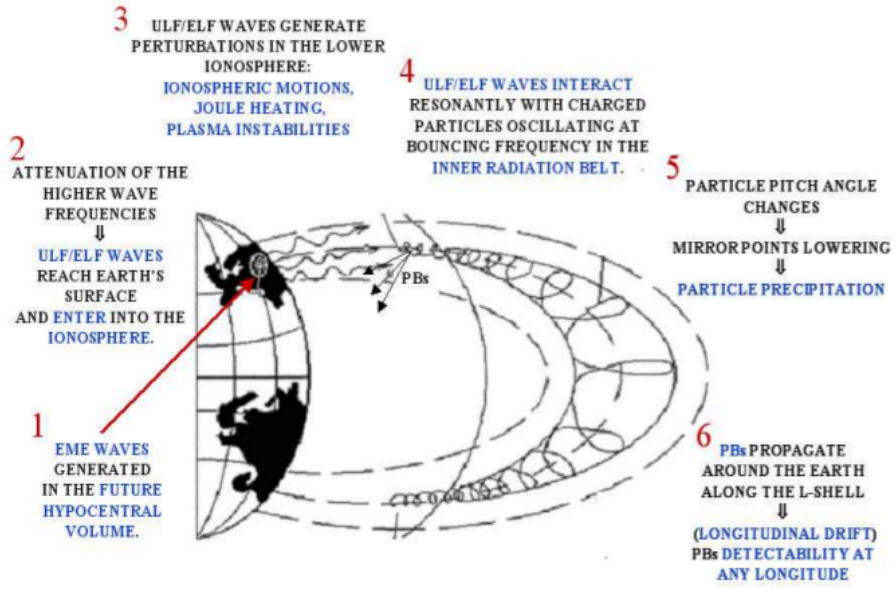

Fig. (1.3) *A scheme illustrating the precipitation of the trapped particles due to interaction with seismogenic EMEs. Adapted from Sgrigna 2001[1]*

used to test several Chinese payloads in order to study the response of the sensors and verify their compatibility with ionospheric plasma, in environmental conditions similar to those met by the satellite in orbit.

1.4 The CSES Satellite

The CSES satellite is based on the Chinese CAST2000 platform (see Fig. 1.4). It is a 3-axis attitude stabilized satellite that will have a polar sun-synchronous orbit with a 507 km altitude and a 97° inclination. It will have a recursive period of 5 days in such a way the ground track is strictly repeated after 5 days, as can be noted in Fig. 1.5. The CSES main body, in the launch configuration, has a dimension of 145 cm (Y)×144 cm (Z)×143 cm (X) that increases after the deployment of the solar panel and the booms with the detectors placed at the tip.

The satellite is composed by several scientific payloads and platform subsystems. These subsystems include the Attitude and Orbit Control subsystem (AOC), the On-Board Data Handling subsystem (OBDH), the Tracking, Telemetry and Command subsystem (TTC), as well as the Power Supply (composed of 80Ah Li-ion battery and solar panels) and the Thermal Control subsystems. Tab. 1.1 summarizes the main specifications of CSES.

The Satellite AOC uses earth oriented 3-axis stabilization, and attitude sensors (3 star

trackers, 2 groups of gyros and 1 digital sun sensor) are used to measure the attitude, reaction wheel and magnetic torque in order to maintain the zero-momentum control.

Housekeeping data between payloads and subsystems are exchanged via the CAN bus, where the On Board Data Handling system is the host and all other apparatus are the guests.

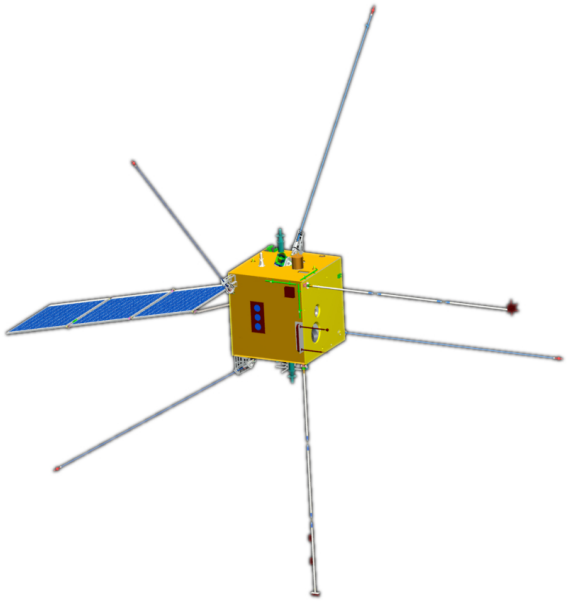

Fig. (1.4) *The mechanical design of the CSES Satellite in the orbit configuration, as can be noted by the deployed solar panel and booms.*

Once in orbit, the satellite flies towards the X axis, while the Z axis points to the nadir. A solar panel is located on one side of the satellite and could rotate around the Y axis.

To reduce the possibility of interference for the scientific payloads induced by the solar panel rotation or the AOC adjustments, the satellite defines two working regions: the payload working zone with latitudes between $-65°$ and $+65°$ and the platform adjustment zone at latitude $>65°$ or latitude $< -65°$, where the payloads stop working.

1.4.1 On-board Scientific Payloads

The scientific payloads hosted by CSES are the following (see Fig. 1.6):

- a Search-Coil Magnetometer (SCM), a High-Precision Magnetometer (HPM) and an Electric Field Detector (EFD) placed at the boom tips, for measuring the three components of the magnetic and electric fields;

ITEM	Specification/Parameter	
Mass	$\simeq$ 700 kg	
Data Transmission	Band	X
	Downlink Rate	120 Mbps
	Mass Memory Size	160 Gbit
Life Span	$\geq$ 5 years	
Orbit Type	Sun-Synchronous Orbit	
Orbit Altitude	507 km	
Orbit Inclination	97°	
Orbit Period	94 min	
Circels per Day	15 +1/5	
Recursive Period	5 Days	

Table (1.1) *Main specifications and orbit parameters of the CSES satellite.*

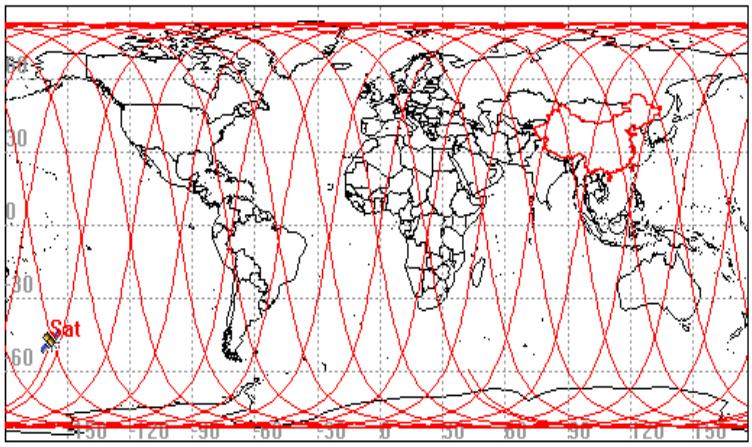

Fig. (1.5) *Satellite ground track after 1 day. The distance between neighbouring tracks in one day is around 2650 km that is reduced to 530 km in the 5 day repeating period.*

- a Plasma Analyser Package (PAP) for the measurements of local plasma disturbances by the analysis of the plasma parameters including the ion density, ion temperature, ion drift velocity and ion composition;
- a pair of Langmuir Probes (LP) for the measurements of the electron density and temperature in the plasma;
- a GNSS Occultation Receiver and a three frequency (VHF/UHF) Transmitter for the study of plasma profile disturbances;
- the High-Energy Particle Package (HEPP) and the Italian High-Energy Particle Detector (HEPD) for the measurement of energetic particle fluxes and spectra with particular attention to those precipitating from the Van Allen radiation belts (with a value of the equatorial pitch angle inside the loss cone).

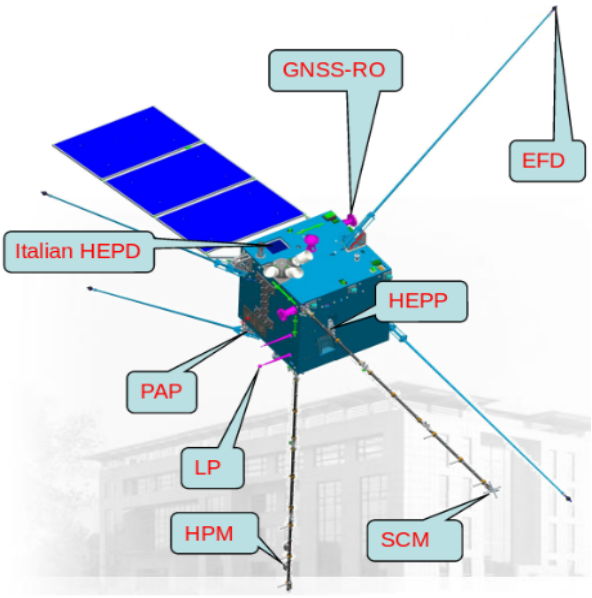

Fig. (1.6) *Position of the instruments on board CSES.*

Thanks to the variety of instruments, CSES has the capability to address several scientific topics, such as the monitoring of the electromagnetic near-Earth space environment, the study of plasma perturbations in the ionosphere, the measurement of electron and proton fluxes, the study of the radiation environment around the Earth in quite solar conditions and during phenomena of solar physics. CSES can complement the cosmic-ray measurements of other flying space missions like PAMELA and AMS in the low energy range, up to few hundreds of MeV. For its specific nature, CSES will be a powerful instrument for the Space Weather forecasting in the incoming solar cycle.

1.5 HEPD Scientific Objectives

The High-Energy Particle Detector (HEPD), built by an Italian collaboration including several sections of the Italian National Institute for Nuclear Physics (INFN) and various Universities, is the only non-Chinese payload on board CSES. The detector has several aims, including the study of the temporal stability of the Van Allen belts, the investigation of the trapped particle precipitation induced by ionospheric and tropospheric EMEs or the study of the acceleration mechanism of solar energetic particles.

The HEPD detects electrons in the energy range between 3 MeV and 100 MeV and protons in the energy range between 3 MeV and 100 MeV, as well as light nuclei.

The instrument consists of several detectors. Two planes of double-side silicon microstrip sensors placed on the top of the instrument provide the direction of the incident particle. A thin segmented layer of plastic scintillator is placed just below the silicon tracker and gives the trigger. This trigger plane is followed by a calorimeter, constituted by other 16 scintillator planes and a layer of LYSO crystals. A scintillator veto system completes the instrument. The power supply and electronics are inserted in a box placed at one side of the detector. The HEPD is contained in an aluminum-honeycomb box installed on the CSES satellite and pointing toward the zenith (see Fig. 1.6).

Four different models of the HEPD have been realized and fully tested: the Electrical Model (EM), the Structural and Thermal Model (STM), the Qualification Model (QM) and the Flight Model (FM).

After almost four years of intensive work, the FM is now completed and installed on board the Chinese Seismo-Electromagnetic Satellite, as shown in Fig. 1.7.

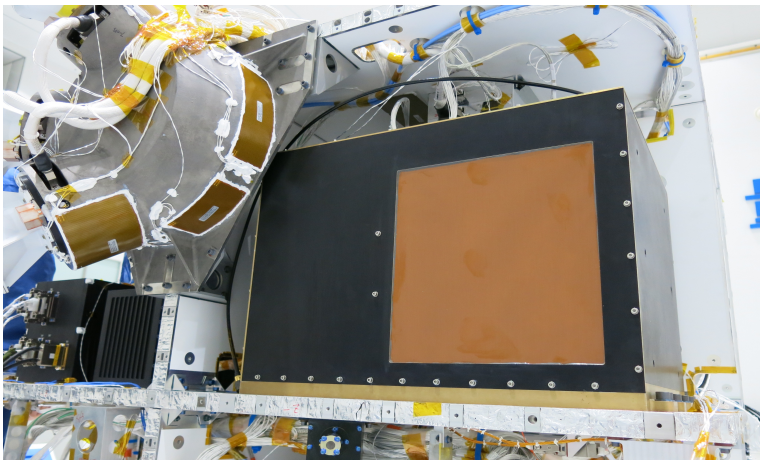

Fig. (1.7) *A picture of the HEPD installed on board CSES. The HEPD window is covered with a Pyralux layer (copper + kapton) to assure thermal insulation.*

1.5.1 Cosmic Rays and Solar Physics

For long duration space missions like CSES, the measurements of cosmic-ray particles need to be related to the ever-changing environment in which the detector operates. The heliosphere, i.e. the region shaped by the presence of the solar wind flowing from the upper atmosphere (the corona) of the Sun, presents different levels of variability, some of them still poorly understood. This variability of the solar wind leads to the insurgence of dynamic phenomena on all spatial and temporal scales [7]. By the time of the launch, the HEPD will be operative during the solar minimum of the 25^{th} cycle, offering ideal conditions to study the propagation mechanisms inside the heliosphere. Nevertheless, such a quiet environment could help to obtain an undisturbed description of solar transients like solar particle events (SPE); these events are rare during the minimum activity phases of the Sun, but the acceleration and propagation of solar energetic particles (SEPs) can be studied with fewer uncertainties caused by a turbulent heliosphere (like during the maximum phases of the Sun's activity cycle). The powerful X-class event of 2006 December 6^{th}[8] together with the Ground Level Enhancement (GLE) of 2006 December 13^{th}/14^{th} represents a perfect example[9]. Moreover, during the maximum activity, SEPs from the Sun become more frequent and a wide variety of data can be accumulated and compared, grouping different events by some of their characteristics such as duration, spectral index or intensity. The HEPD on board CSES could hopefully register a wide number of solar events, in a range of energy between the *in situ* observations by ACE, STEREO, GOES etc. [10] and the high-energy data from AMS02[11] and neutron monitors [12] on ground, thus filling the void left by PAMELA [13, 14]. The $>$30 MeV threshold for protons, together with the polar orbit, allows detection in regions where the geomagnetic cutoff is considerably low and even energetic particles from weak solar events can be measured. The study of the relation between the spectral index and the roll-over energy of a SEP event could also explain the acceleration process that took place; in fact, whether the Sun accelerates particles at low altitudes through magnetic reconnection or in higher regions in the corona through coronal mass ejection-driven shocks (CME-driven shocks) is still a matter of study due to some modification happening during the transport within the interplanetary space [15]. Medium-term transients like Forbush decreases [16], caused by the passage of a CME through the Earth that shields galactic particles, is another possible topic of interest. Large CMEs heavily affect the geomagnetic cutoff [17], shrinking the portion of the magnetosphere facing the Sun and allowing more particles to pour inside regions at lower latitudes. The HEPD energy range is well suited to partially follow the evolution of such decreases, obtaining information on the magnitude of the decrease itself and some information on the recovery time of the galactic particles to a normal condition. On longer time scales, observations of electron and proton energy spectra and their variation during one or more solar cycles will be extremely helpful to understand the processes

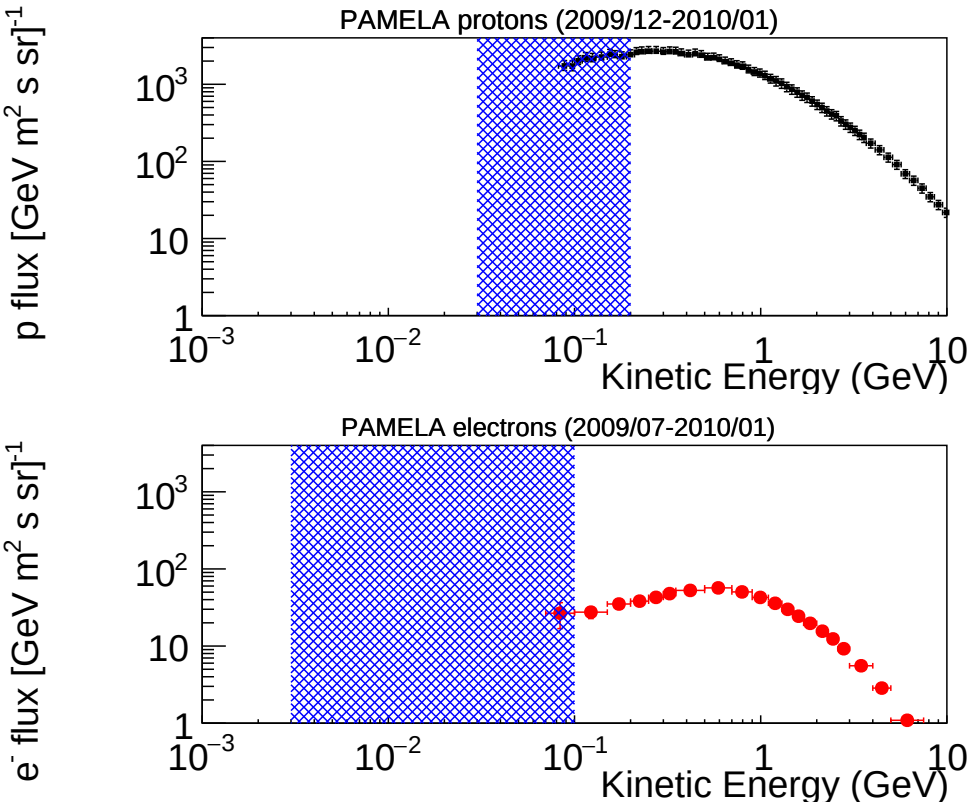

Fig. (1.8) *Comparison between PAMELA protons (upper panel) and PAMELA electrons (bottom panel). Data from [2] and [3] respectively. The blue box refers to the energetic range of the CSES HEPD.*

that dominate the transport inside the heliosphere. Low-energy data from the HEPD could be used to establish a full three-dimensional numerical model [18] based on the numerical solution of Parkers transport equation [19]. Each particle spectrum possesses peculiar features regarding transport mechanisms; moreover many drift models [20] predict a clear charge-sign dependence for the modulation of cosmic rays, so that an electron/proton joint measurement is important. The role of these observations could also gain value if the 25^{th} solar minimum will be unusual like the 23^{rd}, offering a unique opportunity of study such mechanisms in an unconventional situation. Scientific goals aside, the CSES mission comes in a period when the problematics associated with the Space Weather are being recognized as urgent, so that it could also embrace a role of space monitor of the vicinity of the Earth and to help developing further countermeasures against possible future dangerous phenomena coming from the Sun.

1.5.2 Magnetosphere studies

The magnetosphere of the Earth, created by its magnetic field, is not a closed system. Its shape and composition is continuously affected by the flowing solar wind bursting from the Sun and in some cases extreme solar events can temporarily heavily modify its structure [17].

The outer and inner Van Allen radiation belts are extremely variable in composition and this variability is emphasized when powerful SEPs encounter the magnetic field lines. This kind of interactions [21] between cosmic radiation and magnetosphere originates particles called albedo (upward-going direction) which can be further identified as re-entrant if their trajectory is bent by the geomagnetic field allowing them to remain trapped with a downward-going direction, and splash albedo if they are able to escape the magnetosphere [22]. The first family comprises quasi-trapped and un-trapped particles, if they are confined in the equatorial region below the inner Van Allen belt or not [23, 24]. A new and accurate measurement of the high-energy ($>$ 70 MeV) cosmic radiation at low Earth orbits has been reported in [25] as a function of energy and angle between the magnetic field and the direction of the incoming particle. The HEPD silicon tracker system (providing the incident direction) could measure albedo re-entrant protons up to $\sim$200 MeV comparing results with previous experiments.

Thanks to the orbit of CSES through the SAA and the HEPD large angular acceptance (sensitive to different values of pitch-angle), together with the precise measurement of the particle direction provided by the silicon tracker, the HEPD also allows the observation of geomagnetically trapped particles from the inner Van Allen belt and to study the variation of their composition.

1.5.3 Particle Bursts as Short-Term Earthquake Precursors

For the coupling between the lithosphere and the lower magnetosphere, we have seen that the most considered energy carriers are the seismic electromagnetic emissions (SEME) in the form of low-frequency waves. The remote sensing from space is the most efficient method, if not the only one, to search for these couplings, because the monitoring of large areas and simultaneous measurements of many observables are required.

Correlations between short-term variations (bursts) of high-energy charged particle fluxes in near-Earth space and seismic activity have been at first pointed out on the basis of results obtained from several satellite measurements. High-energy charged particle fluxes have been obtained on board of various spacecrafts: MIR orbital station (20 MeV $< E_e <$ 200 MeV), METEOR-3 ($E_e \leq$ 30 MeV), GAMMA ($E_e \geq$ 50 MeV) and SAMPEX ($E_e \leq$ 15 MeV) by different instruments, and have been processed and analyzed with the goal of search for temporal and spatial correlation between particle bursts and

strong earthquakes[4], [26]. As already mentioned, the explanation of this phenomenon is based on the local disturbance of radiation belt particle flux caused by ultra-low frequency (ULF) electromagnetic emissions of seismic origin[6]. This EMEs can be generated in the earthquake zone several hours before the main shock and can propagate through the ionosphere, be captured in the geomagnetic field and then propagates as Alfvén wave along the geomagnetic field lines. The Alfvén wave interacts with trapped particles in the inner belt, causing their precipitations. The main characteristic of this process is that, due to the drift of the trapped particles around the Earth, the particle burst of seismic origin can be observed not only above the epicenter but at any longitude where satellite crosses the disturbed L-shell[2].

Aleksandrin et al. [4] performed an analysis on data from different instruments. They used the MARIA and MARIA-2[27] magnetic time-of-flight scintillator spectrometers installed on board the SALYUT-7 and MIR orbital stations (51° inclination, 400 km altitude), the ELECTRON instrument (a stack of scintillator detectors and a Cherenkov counter) installed on board the METEOR-3 satellite (82° inclination, 1250 km altitude), the gamma-ray telescope GAMMA-1 [28] on board the astrophysical station GAMMA (51° inclination, 350 km altitude), and the PET [29] silicon detector on board the SAMPEX satellite (82° inclination, 600 km altitude). Fig. 1.9 shows the temporal correlation the authors obtained, between particle bursts and a set of earthquakes with M $>$ 4, after selecting satellite positions with L-shell less than 2 (the main part of earthquakes is located in the near equatorial region) and excluding the South Atlantic Anomaly region. The value of ΔT was defined as:

$$\Delta_T = T_{EQ} - T_{PB}, \tag{1.4}$$

where T_{EQ} and T_{PB} are the times of occurrence of the earthquake and particle burst, respectively. The positive value of all the peaks (2-5 hours) means that the particle bursts can be a short term earthquake precursor. In the analysis, sharp short-term increases of particle counting rates, from tens of seconds to a few minutes, were selected as particle bursts if the current counting rate exceeded 4 standard deviations from the average value of the background. Thr authors also investigate the spatial correlation between the burst and the earthquake by studying the variation of the temporal distributions using

$$\Delta L = L_{EQ} - L_{PB}$$

as an additional parameter. The term L_{EQ} is the L-shell of the earthquake (i.e. the L coordinate of the point at a certain altitude above the epicenter, that coincides with the al-

[2]The L-shell is a parameter describing a particular set of Earth magnetic field lines. In particular, it describes the set of magnetic field lines which cross the Earth's magnetic equator at a number of Earth-radii equal to the L-value. For example, L = 2 describes the set of the Earth's magnetic field lines which cross the Earth's magnetic equator two earth radii from the center of the Earth.

titude of the region from which the EME of seismic origin is captured in the geomagnetic field lines) and L_{PB} is the L-shell of the satellites in correspondence of the particle bursts. The analysis shows that the ΔT distributions present no peaks when $\Delta L > 0.5$, i.e. the earthquake L-shell significantly differs from the L-shell of the particle bursts, supporting that the particle precipitation and the earthquakes are correlated.

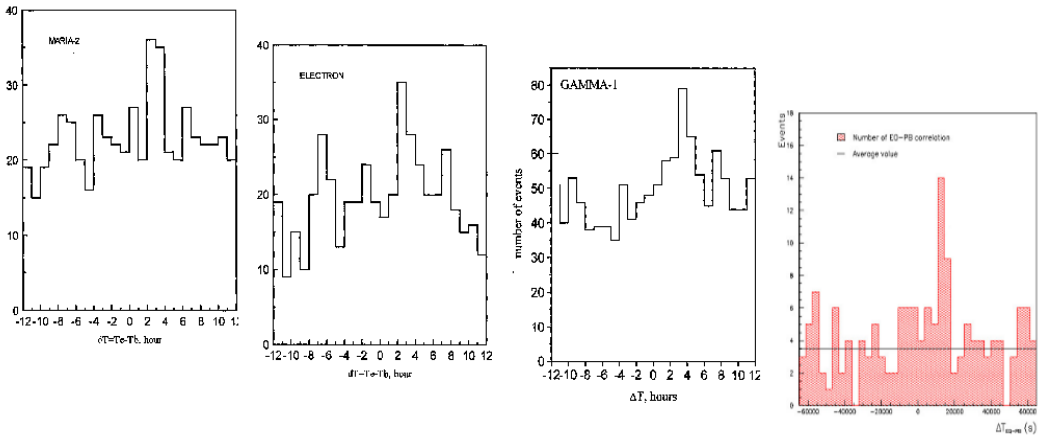

Fig. (1.9) *Histograms of the time difference ΔT between the time of the selected earthquakes and the time of the particle bursts obtained with the MARIA, ELECTRON, GAMMA-1 and SAMPEX space missions. A positive value of the peak suggests that particle bursts precede in time the earthquakes. Plots are from [4].*

1.5.3.1 The DEMETER Mission

The DEMETER mission (Detection of Electro-Magnetic Emissions Transmitted from Earth Regions) [30] was one of the first missions dedicated to the study of the ionospheric perturbations caused by natural phenomena, such as seismic activity, or human activities. The micro-satellite (110 kg) had a polar orbit with about 700 km altitude. The satellite housed several scientific payloads: an electric field detector (ICE), a magnetic field detector (IMSC), a plasma analyser (IAP), two Langmuir probes (ISL) and a particle detector (IDP) for the measurement of electron fluxes in the energy range between 70 keV and 0.8 MeV.

Several papers were published by the DEMETER collaboration to show examples of perturbations of ionospheric parameters in relation with earthquakes[31] [32]. One of the most important results is the statistical analysis of the intensity of waves measured by the Demeter electric antennas as a function of the seismic activity[5]. The results presented in Fig. 1.10 show the electric field measured during night time for earthquakes

with magnitude larger than 4.8 (left) and 5 (right) and with a depth less than 40 km. The figures show a decrease of the wave intensity measured by DEMETER (more intense when the magnitude is larger) in a frequency range between 1 and 2 kHz which starts a few hours before the earthquakes (all earthquake occurrences are at the zero time). The results are presented as a function of the frequency under the form of relative intensity normalized by the standard deviation.

For what concerns the IDP detector and particle precipitation, no clear evidence of temporal correlation with earthquakes was observed. In her Ph.D. thesis, Buzzi[33] performed a study of IDP data according to a previous work based on SAMPEX data, without finding any significant peak in the ΔT distribution (with ΔT defined as in eq. 1.4). These results confirm those obtained in previous studies of low energy particles performed by Sgrigna [34], where no temporal correlation evidence was found with low-energy electrons from SAMPEX-PET data.

The possible explanations for the absence of such correlation between the PBs measured by DEMETER-IDP and earthquake occurrences can be related to different factors, such as the IDP orientation, the low-energy range of the detected particles, or the poor statistics due to the low IDE geometric factor. In fact, the IDP direction, due to the satellite orientation, is always perpendicular to the magnetic field lines in such a way that the IDP detects mainly trapped particles (pitch angle close to $90°$). In addition, the geometrical factor of $\simeq 2cm^2sr^1$ is probably not enough to provide a good statistics. Finally, the IDP was sensitive to particles in the energy range between 70 keV and 0.8 MeV, that is significantly lower than the range measured by the MARIA, ELECTRON, GAMMA-1 or SAMPEX-PET instruments that have been used to obtain the results in Fig. 1.9.

On the contrary to DEMETER, recent studies on low-energy electrons in [35] (E $>$ 0.3 MeV) found a temporal correlation between the precipitation of low-energy trapped electrons and earthquakes with magnitude above 5 Richter scale. The data of the NOAA Polar Operational Environmental Satellites (POES), collected during a 13 year period (corresponding to about 18 thousand M $>$ 5 earthquakes), were used. In particular, the Medium Energy Proton and Electron Detector (MEPED), composed of 8 solid-state particle detectors (geometric acceptance 0.1 cm^{2}sr), was used selecting the highest energy channel and the zenith pointing direction. The authors selected electron bursts (EBs) as a fluctuation of the electron counting rate with a probability $< 1\%$ to be a background fluctuation and they observed a correlation peak at 1.25 hours before the seismic events with a 5.6 σ significance of the correlation peak.

The correlation observed with the NOAA POES data involves electrons of lower energy with respect to the previously mentioned studies[34][4], based on satellites measuring electron energies from few to several MeV. According to the authors, this fact might explain some particular features observed in the analysis, such as the fact that the correlation has been detected only within a limited geographic region or the fact that the

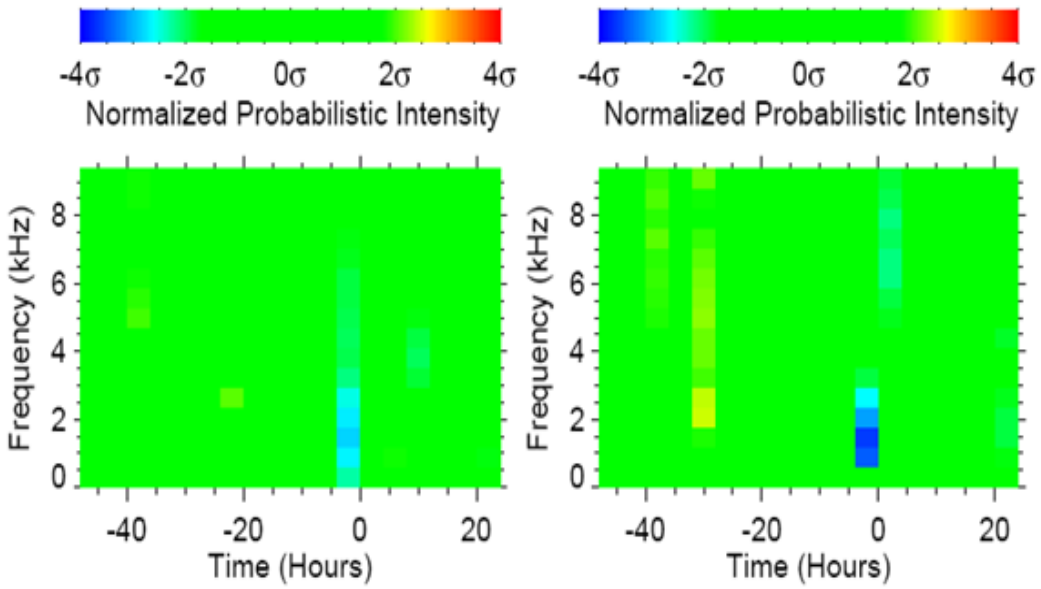

Fig. (1.10) *(left) Frequency-time spectrogram of the normalized probabilistic intensity obtained from the night- time electric field data measured within 330 km of the earthquakes with magnitudes larger than or equal to 4.8 and depth less than or equal to 40 km. Data measured for all Kp values and seasons have been included. (right) The same but for earthquakes with magnitudes larger than or equal to 5.0. Adapted from Nemec et al. [5]*

correlation involves only a small fraction of M>5 earthquakes. It should also be noted that this recent analysis on the NOAA data confirm the previous results for what concerns the absence of a correlation at electron energies < 300 keV, in the proton data, or selecting particle pith angles corresponding to trapped particles.

In this framework, the HEPD detector is perfectly suitable to investigate a correlation between particle bursts and seismic activity. In fact, it perfectly fits the energy range for electrons, it has a wide angular acceptance [36] ($>60°$ over the full energy range) and it has a total acceptance larger than 300 cm^2sr at the peak[3] that is more than 100 times the geometric acceptance of DEMETER and more than 1000 times the one of NOAA POES.

Although low-frequency EMEs have been observed on the ground close to earthquake epicenters, and in space by several satellites before strong earthquakes, their pre-seismic character and postulated contribution to the lithosphere-ionosphere interactions is far from a final experimental confirmation. Further studies on this topic are needed in order to understand the physical mechanisms of the above discussed seismo-magnetospheric correlation, particularly because of the fact that this phenomenon can be applied to the development of earthquake forecasting methods.

[3]The values of the acceptance as a function of the angle and the integrated acceptance have been calculated with a simulation by means of the Geant4 toolkit and are reported in [36].

Chapter 2

The HEPD Detector

As mentioned in chapter 1, the High-Energy Particle Detector (HEPD) was realized in four different models. The current chapter is dedicated to the description of the apparatus in the qualification and flight versions, with specific attention to the physical subdetectors. After years of intensive work, the Flight Model of the HEPD is now finally completed and integrated on board the CSES satellite.

The HEPD detector is contained in an aluminum box with dimensions $20\times20\times40$ cm^3 as shown in Fig. 2.1. The walls and the base plate are made of aluminum honeycomb plates, with the outside surface covered with an aluminized polyamide layer to assure a good thermal insulation. The detector itself, together the power supply and electronics boxes, is fixed to the base plate that is mounted on the satellite by means of 8 screws. Fig. 2.2 shows a scheme of the apparatus inside the box, where the lateral and top panels have been removed. In the figure the HEPD reference system is also shown, with the axes oriented as follows: the Z axis is directed along the longitudinal dimension of the calorimeter; the X axis is directed along the segmentation of the silicon detector and the Y axis is orthogonal to the previous two.

The detection of electrons in the energy range between 3 and 100 MeV and protons between 30 and 300 MeV, as well as the detection of light nuclei, is achieved by means of a set of specialized detectors:

- a tracking system made of 2 planes of double-sided silicon micro-strip sensors, for the reconstruction of the incident particle trajectory and the determination of the absolute value of the charge from the measurement of the ionization produced in the layer;

- a trigger system composed by one layer of plastic scintillator divided into six segments (paddles) and read-out by photo-multiplier tubes that generate an efficient trigger signal to synchronize the data acquisition for the whole detector;

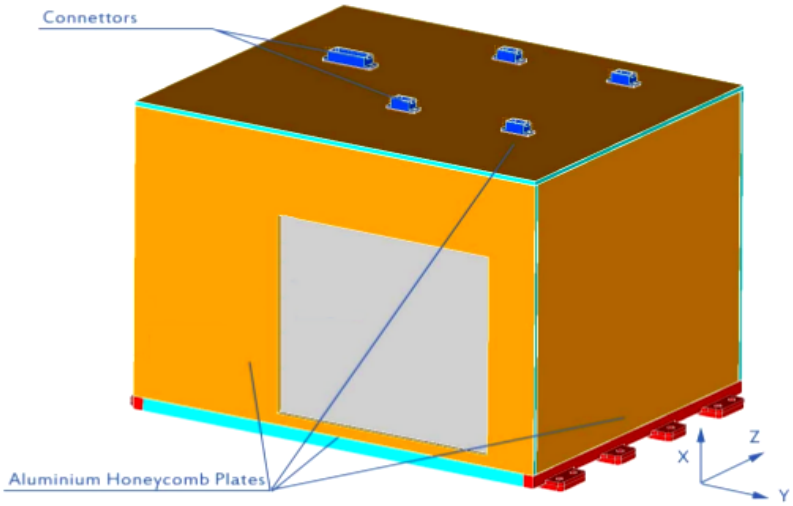

Fig. (2.1) *A scheme of the HEPD box. The connectors for the satellite interface and the base plate with the fixing holes for anchorage can be noted.*

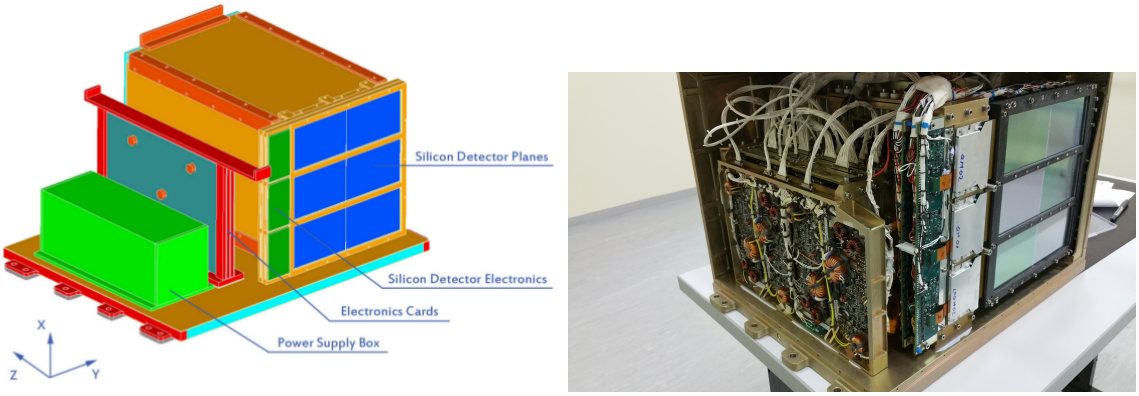

(a) **(b)**

Fig. (2.2) *A schematic view of the HEPD electronics box and detector where lateral and top panels from the aluminum box have been removed (a). A picture of the HEPD (b) with two lateral aluminum honeycomb plates removed.*

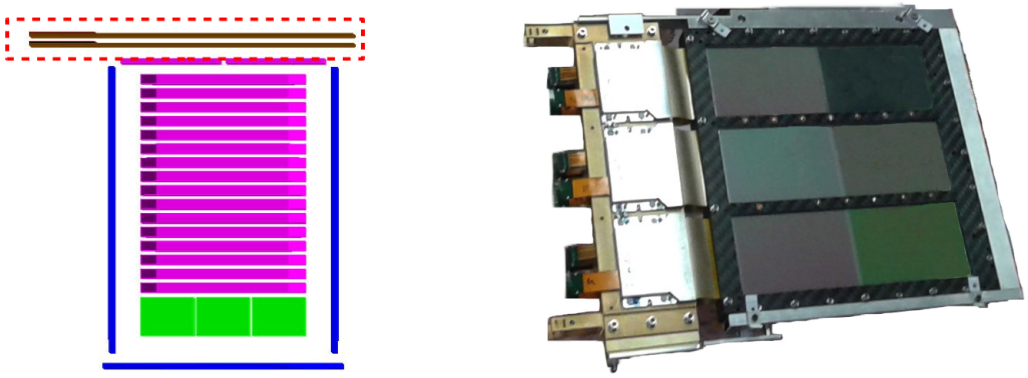

(a) (b)

Fig. (2.3) *A schematic view of the HEPD realized for the Monte Carlo simulations by means of the Geant4 software. All the mechanical structures, as well as the frontal panel of the veto system, have been removed for a better view of the subdetectors (a). A picture of the assembled silicon tracker planes (b).*

- a range calorimeter composed of a first section made of 16 planes of plastic scintillator on the top, and a layer of LYSO crystals on the bottom, for the measurement of the energy deposition and the range of the impinging particles;
- an anti-coincidence (veto) system, composed of 5 plastic scintillator planes (4 lateral and one bottom) read-out by photo-multiplier tubes, used in order to detect particles entering the apparatus from outside the acceptance or particles that are not fully contained within the calorimeter.

The total instrument mass is about 42 kg; the power consumption depends on the current status of the HEPD but is always lower than 40 W.

The following sections describe the general characteristics of the subdetectors of the HEPD apparatus.

2.1 The Tracker Detector

The tracking system of the HEPD is composed by 2 planes (called *external* and *internal*) of double-sided silicon micro-strip detectors, positioned at the top of the apparatus and with a spacing of 1 cm between them. The main characteristic of these sensors is the presence of a sensitive layer on the upper and lower side of the silicon wafer, with the implanted strips of one side orthogonal to those of the other, in order to achieve the measurement of both the X and Y coordinates of the incident ionizing particle.

The use of a double-sided micro-strip detector (see Fig. 2.4), instead of two layers of single-sided ones, offers different advantages: in particular, the smaller total thickness of material that can be achieved yields to a reduction of unwanted effects such as multiple Coulomb scattering and simplifies the mechanical structure. The sensor thickness is an important factor that must be taken into account, since a compromise between the minimization of secondary interactions or coulomb scattering and the necessity of a sufficiently large number of electron-hole pairs is required, in order to provide a good signal over noise ratio. The value of 300 μm is generally considered as an adequate value for the thickness[37] and it is also used for the HEPD silicon sensors.

When an ionizing particle traverses the sensors, the e^-/hole pairs created in the depletion region, drift toward opposite directions: holes are collected by the p strips on the X view and e^- are collected by the n strips on the Y view. From the distribution of the ionizing charge collected by the strips, it is possible to reconstruct the coordinate of the crossing point normal to the strips.

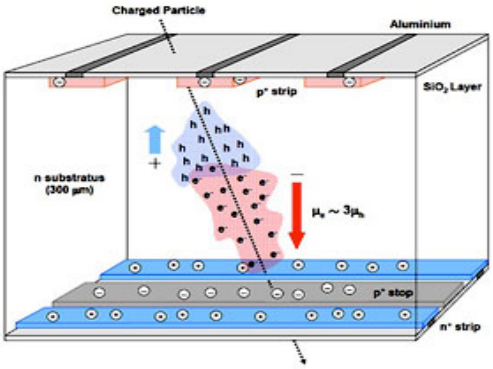

Fig. (2.4) *A scheme of a double-sided mistrostrip silicon sensor. A charged particle crossing the sensor produces e^-/hole pairs that drift toward opposite directions.*

In the HEPD tracker detector, each silicon plane, with dimension of 213.2 $\times$ 214.8 mm^2 excluding the mechanics, is divided into 3 identical independent sections, called *ladders*, along the X axis. They are called *top*, *central* or *bottom*, where the top is the one with the highest value of the X coordinate.

Each ladder is composed by 2 modules (or sensors). A single sensor, produced by FBK[38], has a dimension of 109.63 mm $\times$ 77.58 mm but with a smaller active area of 106.63 mm $\times$ 71.58 mm in order to avoid interferences caused by the support structure at the borders. As already mentioned, it is formed by a substrate of 300 μm thickness: on one side 767 p^+ parallel strips (384 read-out + 383 non read-out) are implanted with a 182 μm pitch to form p^+-n junctions with the substrate. On the opposite side there are 1151 n^+ strips (576 read-out + 575 non read-out) alternated to p^+ blocking strips (called

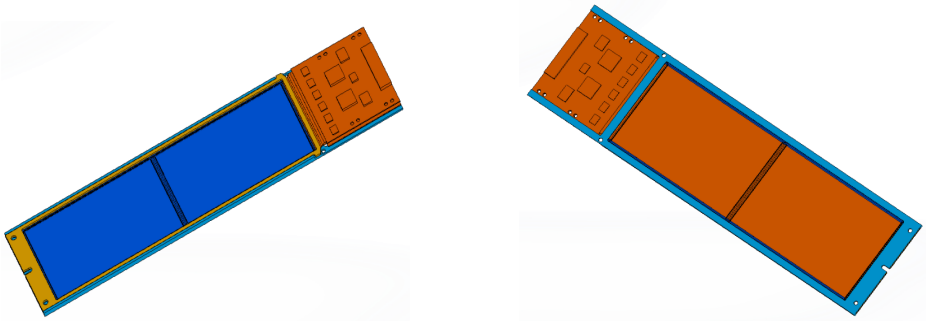

(a) (b)

Fig. (2.5) *HEPD silicon ladder mechanical drawings: S-side in a and K-side in b. The two sensors and the hybrid circuit for the read-out can be noted.*

p-stop) which ensure proper strip insulation.

The read-out strips are directly connected with the read-out electronics by means of AC pads (i.e. a capacitor is connected between the strips and the read-out amplifiers), while the non read-out strips (or *floating* strips) are used to reduce the total number of wires. In fact, the charge deposited on the floating strips can be read-out on their adjacent strips by means of capacitive coupling effect. The role of the floating strips and the consequence of their presence is better discussed in chapter 5, where a preliminary analysis on the silicon data is shown.

The strips on the sensor are surrounded by a *bias ring* that provides the 60 V to the n side, and a *guard ring* to limit edge and surface currents.

For our silicon sensors, the following convention is adopted: the p-side view is defined ”S-side” (silicon-side); the n-side view is defined ”K-side” (kapton side). An assembled ladder is shown in Fig. 2.5 (a) and (b), for the S-side and the K-side respectively. A mechanical frame made of fibre glass material provides the mechanical support for the detector assembly with the front end electronics. This is composed by two identical specific printed circuits (called hybrids), one for the S-side and one to the K-side, each one including 6×64-channel VA140 chips, for a total number of 384 (channels) × 2 (side) channels per ladder.

On the S-side, the strips of the two sensors forming a ladder are directly bonded with aluminum wires in order to reduce the total number of channels. Then they are connected to the hybrids by means of a kapton cable that is used to adapt the pitch among the silicon detector and the analog input of the VA140 chips. A detailed view of the S-side of a sensor is reported in Fig. 2.6.

On the K-side, since the total number of strips (1152) is 3 times the number of available channels (384 as for the S-side), the silicon channels are read in 3 blocks of 384 strips each (i.e. the strip #1 of the first sensor is connected with the strip #384 of the first

sensor and with the strip #192 of the second sensor) and the electrical connection of the strips are provided by an ad hoc kapton cable that brings the signal to the analog input of the hybrid read-out chips.

Considering the reference system on Fig. 2.2, the S-side corresponds to the X view and the K-side corresponds to the Y view. The ambiguity introduced by the measurement of the Y coordinate, due to the 3 strips connected together, can be easily solved by using information from other detectors, such as the trigger plane that is segmented along the Y axis. On the other hand, having the same number of channels for the X and Y views allows to have a much more compact mechanical structure because of the two identical read-out hybrids for both views.

A completely assembled plane of silicon detector is illustrated in Fig. 2.3 (b).

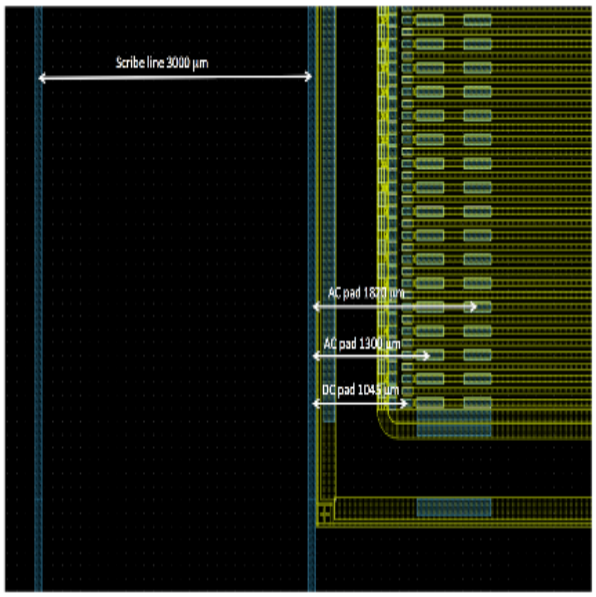

Fig. (2.6) *A detailed view of the silicon sensor on the p-side. The active area, containing the strips at 3 mm distance from the sensor border, can be seen. The presence of a floating strip (without AC pads) between two read-out strips can also be noted.*

2.2 The Trigger Plane

The trigger system is made of one thin layer of plastic scintillator ($20\times18\times0.5$ cm^3) divided into 6 segments (or paddles) with dimension $20\times3\times0.5$ cm^3, each one read by two Hamamatsu Photo-Multiplier Tubes (PMTs). The plane is positioned below the tracker system and it solves the following tasks:

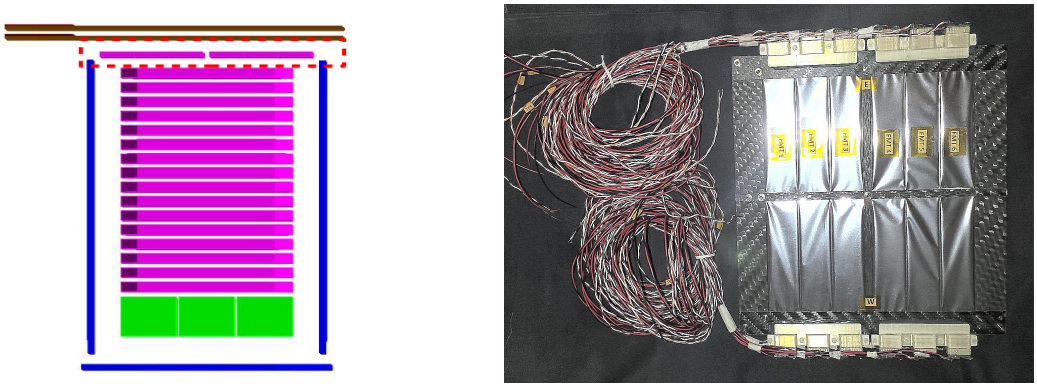

(a) (b)

Fig. (2.7) *A schematic view of the HEPD realized for the MonteCarlo simulations by means of the Geant4 software. All the mechanical structures, as well as the frontal panel of the veto system, have been removed for a better view of the detectors (a). A picture of the segmented trigger plane (b).*

- a fast trigger signal generation to start and synchronize the data acquisition for the whole apparatus;
- removal of the ambiguity on the Y coordinate position reconstruction, introduced by the tracker system;
- a possible secondary determination of the ionization energy loss produced in the layer, in addition to the more precise measurement obtained with the tracker;
- the possibility to reject events with more than one paddle hit (multi-particle events).

To generate the trigger signal, the coincidence between a signal on at least one of the trigger paddles and the signal from at least one additional calorimeter plane is required. A picture of the trigger plane can be seen in Fig. 4.6 (b).

2.3 The Calorimeter

The range calorimeter of the HEPD detector consists in two different parts. The first one, on the top and immediately below the trigger plane, is made of 16 planes of plastic scintillator. Each plane has a dimension of $15\times15\times1$ cm^3 and is read-out by two PMTs, placed at two opposite corners of the plane. The bottom part of the calorimeter consists of a 3×3 matrix of LYSO inorganic scintillator crystals, for a resulting plane with total dimension of $15\times15\times4$ cm^3.

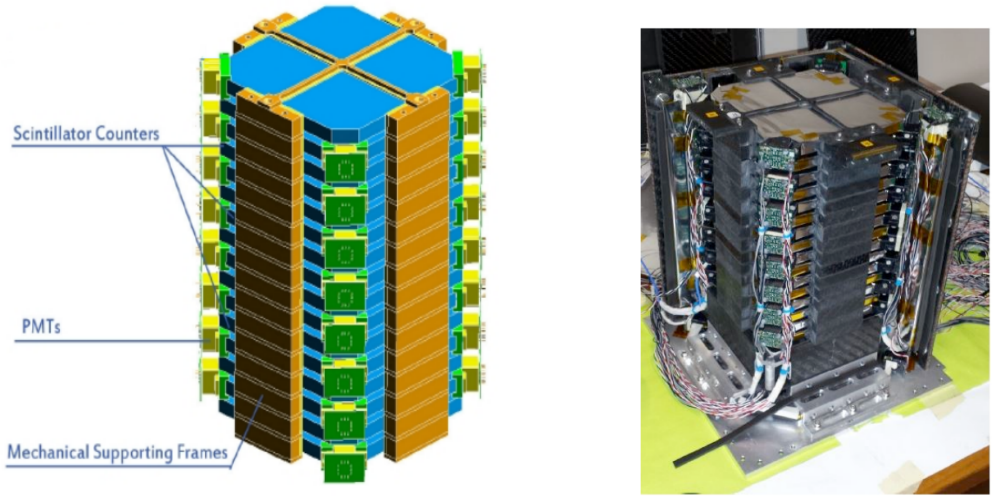

(a) (b)

Fig. (2.8) *The mechanical scheme of the scintillator tower containing the plastic scintillator planes, the photo multiplier tubes at the corners and the mechanical structure (a). A picture of the assembled scintillator tower (b).*

The stability of the system is assured by a suitable mechanical structure, which holds the detector in place and prevents any damage during the launch phase. The scintillator counters are arranged in a vertical stack and positioned by a carbon fiber frame, each one mounted on top of the other, in such a way to form a rigid tower where each counter is separated by the adjacent ones (see scheme and picture in Fig 2.8). Layers of relatively soft material open-cell Poron (the yellow structure in the mechanical scheme in Fig. 2.8 (a)), placed between the counters and the carbon fiber, prevent any stress and shock to be transferred to the counters themselves, such tp avoid damages. The high rigidity of the system provides a great safety margin against stresses and vibration shocks.

The aims of the calorimeter are the measurement of the energy deposition and the range of the impinging particles. The presence of the LYSO bottom layer provides an increase to the operational energy range by providing a larger matter thickness with high density.

2.3.1 Plastic Scintillators

A plastic scintillator material, characterized by fast response and relatively high light output, has been selected for the realization of the top calorimeter. One of the biggest advantage of plastic scintillators is their ability to be shaped into almost any desired form as well as the high durability.

A calorimeter scintillator plane can be seen in Fig. 2.9. The four corners have been cut in order to create the space to place the PMTs. Each plane contains two PMTs, placed at two opposite corners. Due to mechanical reasons, two consecutive planes have the PMTs placed at different couples of corners as can be seen in Fig. 2.8.

Fig. (2.9) *A picture of one plastic scintillator plane from the calorimeter tower.*

The external walls of the planes, with the exception of the entrance windows of the PMTs, are optically insulated by means of a thick mylar foil with about 95% reflectivity index. This foil reflects back the fraction of scintillation light escaping from the plane, thus increasing energy resolution. This is much more important in case of the trigger system, where each paddle is covered with the same mylar foil, preventing the escaped light to be detected by a PMT on an adjacent paddle, which would generate spurious pulses.

The scintillator material selected for all the plastic planes (trigger, calorimeter, veto system) is the EJ-200 by Eljen Technology[39] that combines long optical attenuation length and fast timing, which make it useful for time-of-flight systems as well. It consists of an organic polymer which is luminescent when irradiated by ionizing particles. Some properties of the EJ-200 are reported in Tab. 2.1, while Fig. 2.10 shows its emission spectrum.

2.3.2 LYSO Matrix

The bottom part of the calorimeter is made of a LYSO (Cerium-doped Lutetium Yttrium Orthosilicate) inorganic scintillator. This is a high density material (d = 7.3 g/cm^3) that,

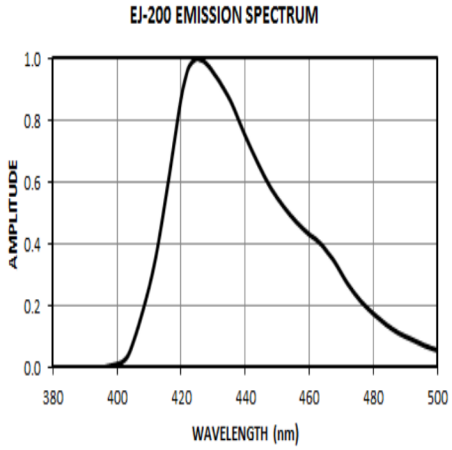

Fig. (2.10) *Emission spectrum of the EJ-200 plastic scintillator.*

PROPERTIES	**EJ-200**
Light Output (% Anthracene)	64
Scintillator Efficiency (photons/1 MeV e^-)	10
Wavelength of Maximum Emission (nm)	425
Ligh Attenuation Length (cm)	380
Rise Time (ns)	0.9
Decay Time (ns)	2.1
Density (g/cm^3)	1.023
Temperature Range	$-20°C$ to $60°C$

Table (2.1) *Some properties of the EJ-200 plastic scintillator.*

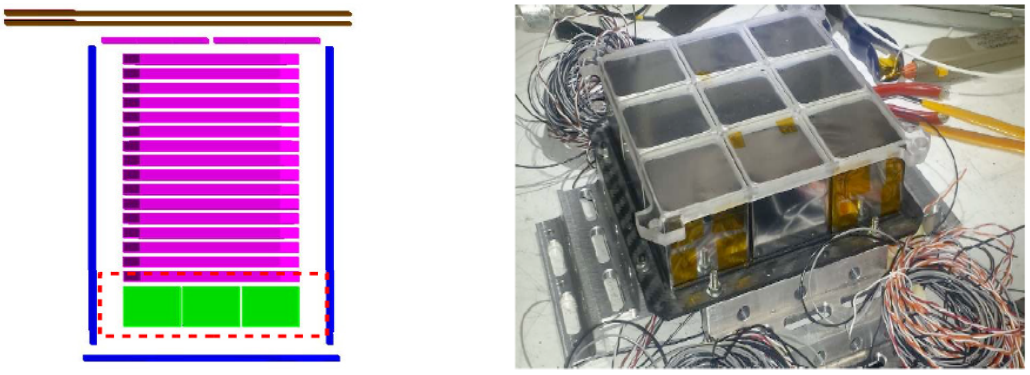

(a) (b)

Fig. (2.11) *A schematic view of the HEPD realized for the Monte Carlo simulations by means of the Geant4 software. All the mechanical structures, as well as the frontal panel of the veto system, have been removed for a better view of the detectors (a). A picture of the LYSO matrix plane (b).*

combined with the 4 cm thickness, allows to increase the operational energy range of the energy detector.

The LYSO layer is formed by a 3×3 matrix (see Fig. 2.13), where each crystal has dimensions 4.8×4.8×4 cm^3 and is read-out by a single PMT placed in the bottom side (the side opposite to the trigger plane). These crystals have the advantages of high light output, quick decay time, excellent energy resolution and low cost. The peak of the emission spectrum is at 428 nm; this makes it possible the use of the same Photo Multiplier Tubes adopted for the plastic scintillator planes, for the read-out.

2.3.3 Photo Multiplier Tubes

A Photo Multiplier Tube is composed by a photo sensitive layer (photo-cathode), which emits electrons when hit by light in a specific range of wavelengths, a set of intermediate electrodes (dynodes), and a final anode, kept at high voltages with respect to the photo-cathode. The whole structure is located in a vacuum metallic box with a glass window for the incoming light, in correspondence of the photo-cathode. The e^-, emitted by the photo-cathode, are accelerated by the strong electric field toward the first dynode stage and cause the emission of a larger number of secondary electrons. Then they are accelerated toward the next dynode until they finally reach the anode forming in such a way a current pulse.

The PMT model that has been chosen for the read-out of all the HEPD scintillator counters, is the R9880-210, manufactured by Hamamatsu[40]. As can be seen in Fig. 2.12 (a), the quantum efficiency spectrum (i.e. the ratio between the number of output electrons and the incident photons) matches the light emission band characteristic of the

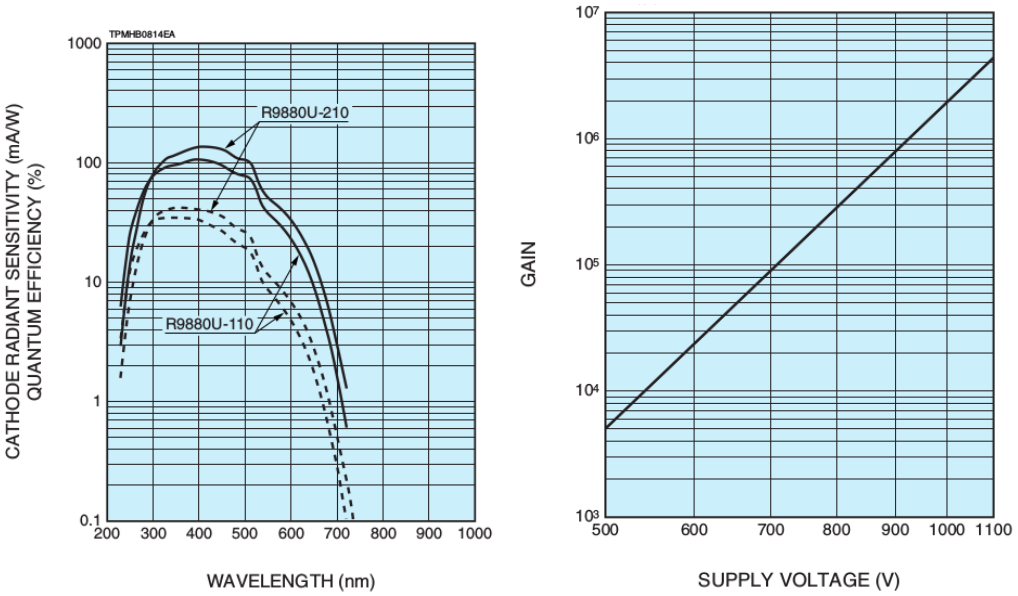

(a) **(b)**

Fig. (2.12) *PhotoMultiplier tube quantum efficiency (a) and gain (b).*

scintillator EJ-200 with a peak at 425 nm. Furthermore, the R9880-210 is a small device (with a cylindrical shape and a 8 mm diameter effective area for the entrance window) with a small weight and an operating temperature in the range $-80°C \div +50°C$ that are all important parameters to be taken into account for a space borne apparatus.

Considering the supply voltage between 750 and 900 V provided by the HEPD power supply system, the gain obtained by the R9880-210 is in the order of 10^5-10^6 (see Fig. 2.12 (b)).

The interface between the PMT and the scintillator plane is obtained through a soft optical pad.

2.4 The Veto System

The veto system with which HEPD is provided includes five thin EJ-200 plastic scintillators that completely surround the calorimeter. The veto counters are placed inside a volume created by the calorimeter structure and carbon fiber honeycomb plates located externally. A Poron thickness, placed all around the scintillators, prevents any stress and shock to be transferred to the counters themselves.

The veto subdetector is fundamental in rejecting any type of background caused by out of acceptance events. In particular, the system is design for:

- the identification and rejection of particles which do not cross the two tracking

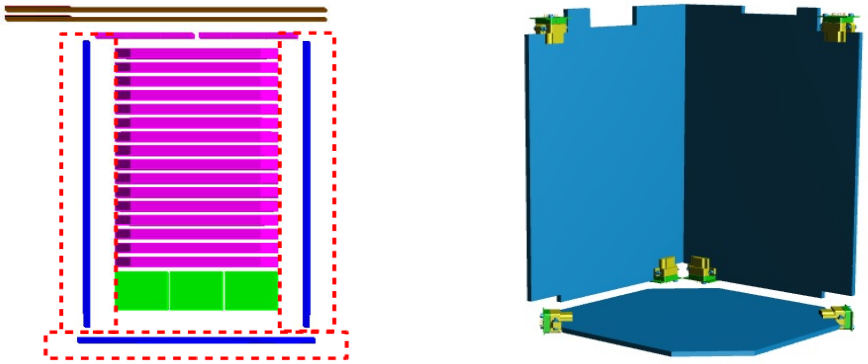

(a) (b)

Fig. (2.13) *A schematic view of the HEPD realized for the Monte Carlo simulations by means of the Geant4 software. All the mechanical structures, as well as the frontal panel of the veto system, have been removed for a better view of the detectors (a). A scheme of the bottom layer and two lateral layers of the veto system that surround the calorimeter, from the mechanical design of the HEPD (b).*

planes but generate a trigger signal (for example by entering the apparatus laterally);

- the rejection of secondary particles produced inside the calorimeter;
- the rejection of not fully contained events.

All the planes of the veto system are 5 mm thick and read-out by the same two R9880-210 Hamamatsu PMTs. Four planes are located at the sides of the calorimeter and the fifth one is below the LYSO layer, to reject particles which are not fully contained within the calorimeter, or up-going particles.

Chapter 3

Electronics of HEPD

In this chapter the most significant characteristics of the HEPD electronics are illustrated, with specific attention to the Digital Signal Processor included in the Data AcQuisition (DAQ) and CPU board, that is the main topic of this thesis. I took part in the optimization and test of these boards, and in the integration of the whole electronics subsystem, that was assembled at the "Roma 2" INFN Section and Physics Department of Rome "Tor Vergata" University.

3.1 Electrical Model

The Electrical Model (EM) of the HEPD was the first model to be developed to test all the interfaces between the HEPD payload and the Chinese satellite. The main purposes are:

- to demonstrate the software design of the platform and HEPD payload;
- to verify the compatibility between the platform and the payload;
- to verify the payload functional performances.

The Electrical Model was composed by a power supply and an electronics board, based on a Zynq Evaluation Board (ZC702). A daughter board, to plug directly to the Zynq, was developed to complete all the required electrical interfaces, such as the TM/TC (TeleMetry and TeleCommands) interface, the 2x RS-422 transceivers for the scientific data channels and the 2x CAN bus transceivers. The Zynq FPGA included a processor with a Linux-like operating system. A picture of the assembled Electrical Model can be seen in Fig. 3.1.

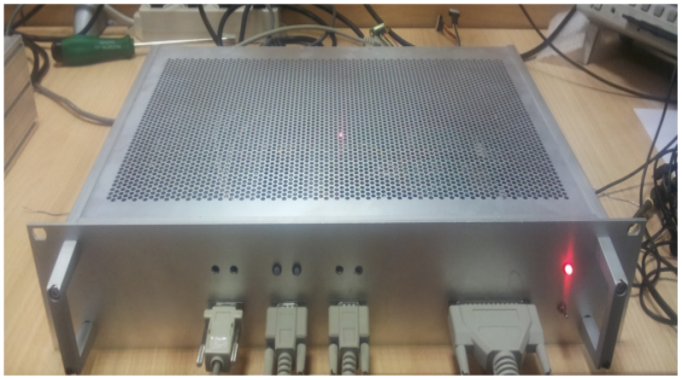

Fig. (3.1) *A picture of the HEPD Electrical Model. The box contains a space-qualified power supply and the Zynq plus the daughter boards that constitute the electrical interface towards the satellite.*

3.2 QM and FM: General Characteristics

For what concerns the Qualification (QM) and the fFlight Models (FM) of the HEPD, the electronics subsystem (ELS), as well as the whole detector, is composed by the same components. It includes the front-end electronics for the silicon detector plus the 5 following boards:

1. Power Control board: responsible of providing the power supply to all the other components of the ELS;
2. CPU board: responsible of controlling the whole detector status and to communicate with the platform of the satellite via the CAN BUS interface;
3. EASIROC/Trigger board: responsible of the trigger pulse generation for the event acquisition, and to the read-out of the PMT data;
4. High Voltage board: responsible of providing the high voltage for the two silicon planes and the 63 photo multiplier tubes;
5. Data AcQuisition board: responsible of the silicon detector read-out and of the event processing, compression and formatting of the event during the acquisitions.

A scheme of the HEPD ELS is shown in Fig. 3.2. The CSES satellite provides the 29 V to the Low Voltage Power Supply, that splits them into different digital voltages for the Power Control Board. The latter one is responsible for the power-on of the other components.

For the realization of all the HEPD boards, one of the main components is a *field programmable gate array* integrated circuit (FPGA) that was chosen for the realization of

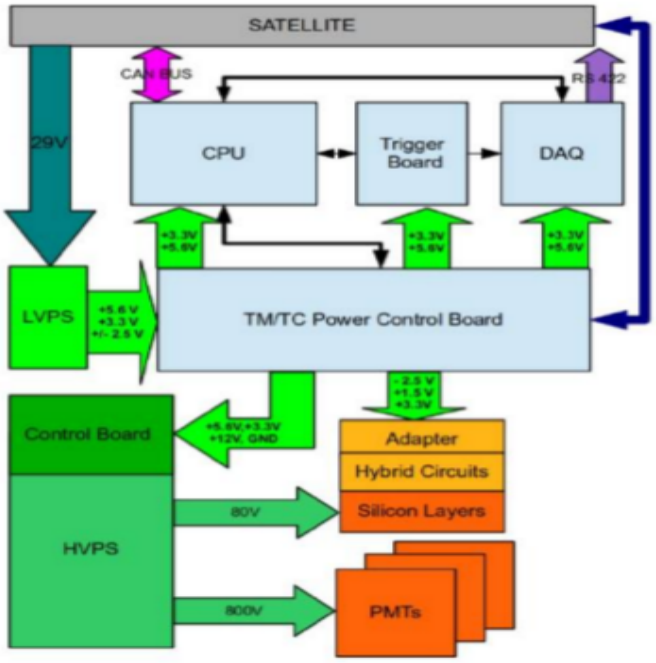

Fig. (3.2) *A general scheme of the HEPD electronics and power supply subsystems. The communication and power lines between the boards and towards the satellite are shown as well.*

a high-quality digital system. A FPGA chip contains a general purpose logical structure, that can be directly configured by the final user to obtain the desired functionalities. This leads to a decrease of the cost and to a high user configurable system with respect to an *application specific integrated circuit* (ASIC), that is a chip where the functionalities are implemented at the moment of the fabrication process with an increase of the costs and development times.

Each FPGA of the HEPD ELS, with the exception of the FPGAs on the CPU and DAQ boards (where the main logic is implemented in a digital signal processor), implements the logic needed for the functioning and control of its specific board and a slow control protocol for the inter-board communication.

3.3 Reliability in Space Experiments

The most important requirement for a space experiment electronics system is to assure a high reliability during the whole duration of the mission (5 years for CSES-Limadou) and low power consumption (< 45 W for HEPD [41]). The compromise between these two important constraints, in addition to the imposed volume occupation, had an important role in the design of the HEPD electronics.

To assure a high reliability, a possible permanent damage for an electronics component must be taken into account during the design phase. The probability of such a failure increases with the overall operating time and with the total number of performed power cycles. This effect is commonly known as *aging* of the component. Other effects, such as a mechanical damage of a board induced by the strong accelerations during the launch phase, can produce a permanent damage. For this reason, mechanical qualification tests were carried out with the whole apparatus at the SERMS facility in Terni (Italy) [42], as described in chapter 5.

In order to limit the consequences of permanent failures in the electronics subsystem for the progress of the mission, each board was developed following the method of high redundancy. Each electronics board is physically duplicated, so that an identical spare copy (or *cold* side) is available in case of failure of the main part (the *hot* side). Hot and cold sides can not be powered on at the same time. A second level of redundancy is applicated for what concerns the important components for each board. For example, in the data acquisition board, two non-volatile memories are used to store the software application for the digital signal processor. In case of a failure in one of them, it is always possible to start the program from the second one. The same strategy was taken into account for the CPU board.

It can be noted that the concept of redundancy was also considered for the subdetector components of the apparatus. For example, as shown in chapter 2, each scintillator plane

is read-out by two PMTs. The loss of one of them leads to a small decrease in the detector resolution but does not affect the entire functionality.

The drawback of this design is clearly the multiplication of the number of components, connections and wires. In fact, for the silicon detector, it is not possible to duplicate all the components due to the large amount of channels. In this case, a different design was adopted; each plane was segmented into three ladders that can be powered on/off independently on one another. A problem on a specific ladder leads only to a reduction of the HEPD acceptance.

3.4 Data AcQuisition Board

The Data AcQuisition board (DAQ), in the frame of the HEPD detector, provides the following functionalities:

- an interface with the front-end electronics of the silicon planes;
- processing and digitalization (by dedicated ADCs) of the analogue signal coming from the silicon plane front end;
- online calibration of the silicon detector;
- acquisition of the PMT data coming from the trigger board;
- compression of the data, in order to reduce the size of the events;
- formatting and transmission of the data to the satellite via the RS-422 interface (scientific data link).

To support all these functionalities, the board is mainly composed of:

- a *Digital Signal Processor* (ADSP-2189M) for all the computing operations;
- 2x FPGAs (called Main and Download);
- 2x non-volatile *Ferroelectric Random Access Memories* (FRAM) for the permanent storage of the code to be executed by the DSP and other important data required at the boot of the board;
- a *Dual-Port Random Access Memory* (DPRAM) used for the data handling between the Main FPGA and the DSP;

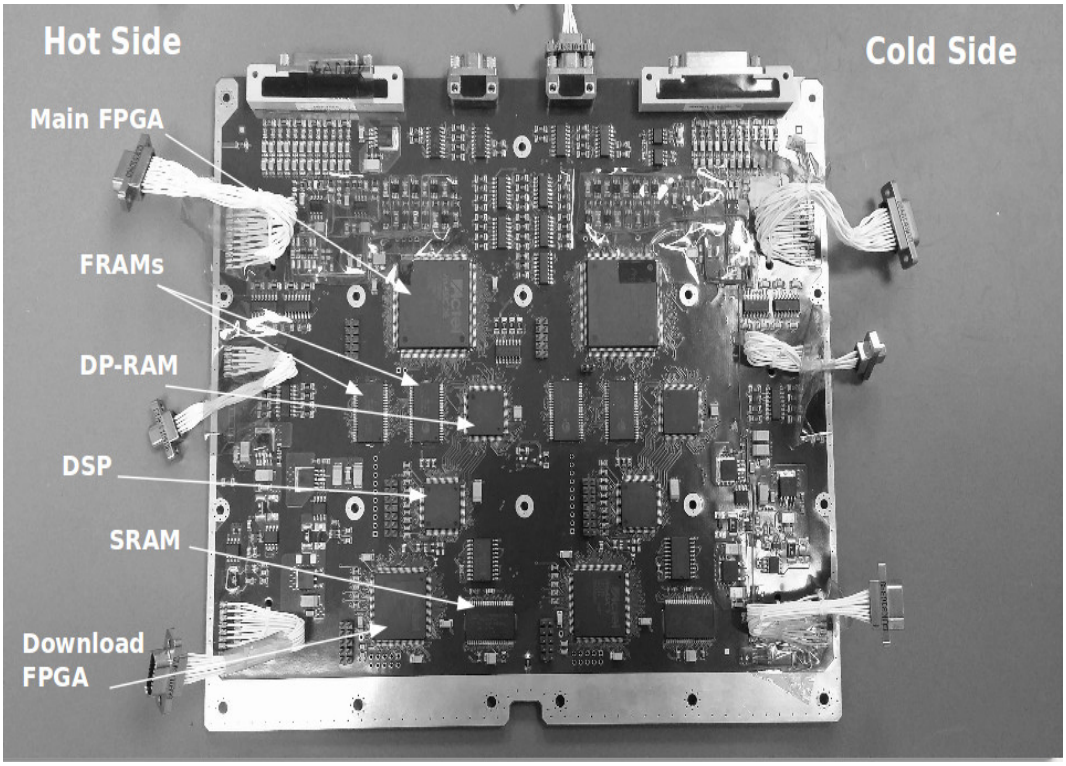

Fig. (3.3) *A picture of the DAQ board. It can be noted that the right and the left parts of the board are identical since every component is duplicated in order to assure the redundancy of the system. This is true with the exception of the top of the board, that contains the interface with the silicon detector and the two connectors for the two silicon planes. In this specific case, due to the large amount of channels, a complete duplication is not possible.*

- a *Static Random Access Memory* (SRAM) used as a FIFO[1] for the data to transfer towards the satellite;
- 8x 12-bit ADCs for the digitization of the silicon detector data.

The operating frequency of the board was set to 48 MHz, as the best compromise between the requirement of fast operations and a not too high power consumption.

Ferroelectric RAMs are random access memories that use a ferroelectric layer instead of a dielectric layer to achieve the non-volatility[2]. They offer the same functionalities as the flash memories but with several advantages. FRAM memories require low voltage to perform a write operation compared to flashes, and this translates into low power consumption. Moreover, writing operations are better in terms of speed and several tests show that SEU[3] response is very good. Another, and probably the most significant aspect to be considered, is the device endurance. The number of writing cycles that can be sustained by a flash or EEPROM device is in the order of 1×10^4, while FRAM memories can be written more than 1×10^{12} times. In the HEPD framework, the two FRAMs are used to store the code of the DSP but also the silicon calibration data calculated every satellite orbit, as it will better discussed in chapter 4. For this reason, the endurance to the write cycles is a very important aspect. The drawback of the FRAM technology consists in the lower device density compared with the flash, that translates in a bigger component dimension. In a spacecraft experiment, where the size requirement of the memory is small, FRAM memories are one of the best solutions for a non-volatile memory.

The Dual-Port RAM, is instead a volatile memory and is used for a different purpose. Its main characteristic is that it allows multiple read or write operations to occur at the same time. In the DAQ board, it is used because it can be written by the Main-FPGA, while the DSP performs read operations on different data.

A picture and a block scheme of the DAQ board with its main components can be seen in Fig. 3.4.

3.4.1 The Digital Signal Processor: DSP

The DSP microcomputer used in the DAQ board is dedicated to the elaboration of the acquired data. An Analog Device ADSP-2189M was selected because of its operative temperature range, low power consumption and high reliability. This chip combines the

[1] Acronym fot First In, First Out. It is a method for organizing data buffer, where the oldest (first) entry is processed first.

[2] A non-volatile memory is a type of memory that can retrieve stored information, even after having been powered off.

[3] A single event upset (SEU) is a change of state in a electronic device such as microprocessors or memories, caused by one single ionizing particle striking the component.

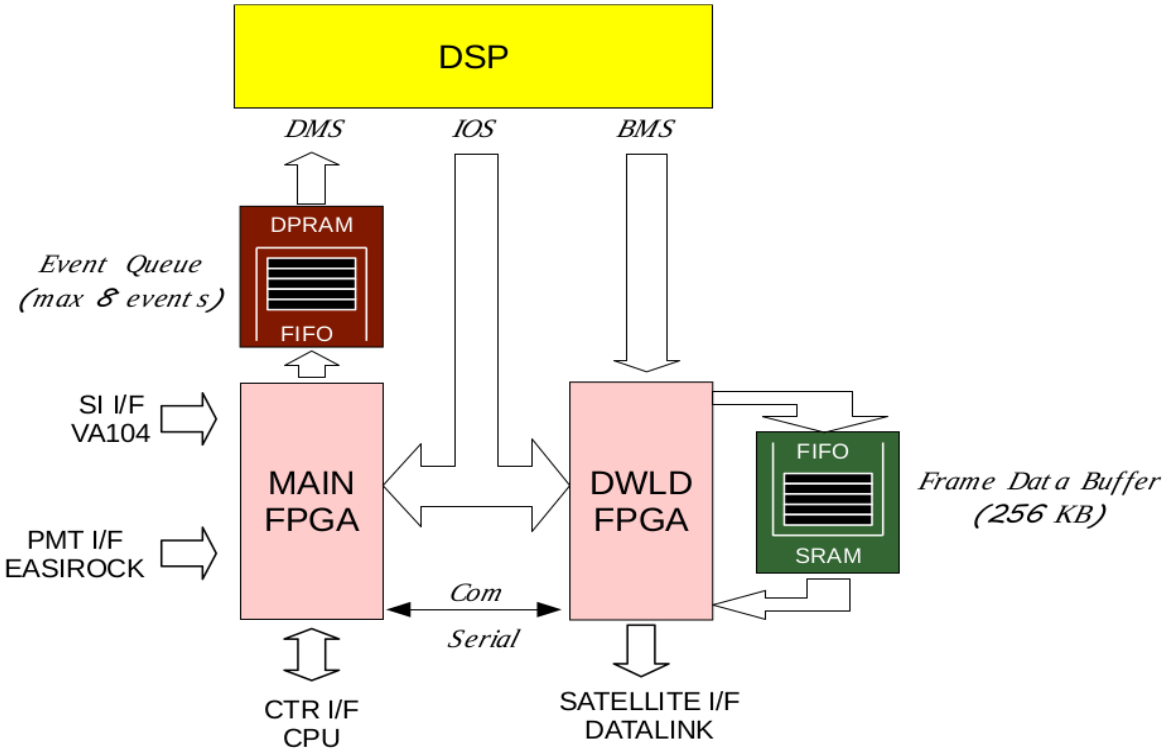

Fig. (3.4) *A block scheme of the DAQ main components and relative communication buses.*

ADSP-2100 family architecture adding a set of peripherals, including two serial ports, a set of programmable input/output lines that can be used as interrupts or as control bit (flags), an Internal 16-bit Data Memory Access port (IDMA), a Byte Data Memory Access port (BDMA) and 192 kB of on-chip memory. In Fig. 3.5 the ADSP-2189M functional block diagram is reported.

This DSP can operate up to a 13.3 ns instruction cycle time and can perform multiple operations in parallel. In one processor cycle, the ADSP-2189M can perform a computational operation, generate the next program address or perform a data move, while receiving and/or transmitting data through the DMA or the BDMA ports or decrementing the internal timer. The clock frequency is equal to half the instruction rate; a 37.5 MHz input clock yields a 13.3 ns processor cycle (equivalent to 75 MHz). For the DAQ board, the Main FPGA receives an input clock at 48 MHz and generates the clock to the DSP to half the frequency.

The internal RAM memory of the ADSP-2189M is configured as 32 kwords (24 bit) of *program* RAM and 48 kword (16-bit) of *data* RAM. The *program memory* is divided into 6 pages of *overlay*: the first one is accessible by specifying the address, while the other 5 pages (3 internal and 2 external) use the same addresses and can be accessed specifying the number of the overlay page in a specific register (PM_OVLAY). The *data memory* structure is designed in a similar way, but with seven overlay pages: 5 internal to the DSP and 2 external (see Fig. 3.7), plus the always accessible one. In the HEPD-DAQ framework, the overlay pages of the *data memory* are used as follows: two internal pages (4-5) are used to store the silicon calibration data, in order to access them faster when the DSP is in an acquisition state. Other two internal pages (6-7) are used as a circular FIFO to temporarily store the data that must be transferred to the satellite and the last internal page (0) is used during the silicon calibration phase. Only one of the two external pages is used (1), and is linked to the Dual Port RAM memory. This memory can be accessed by both DSP and FPGA at the same time and is used for the data exchange between the two components. For what concerns the *program memory* usage, the application code was stored between the pages in a way that the most used functions are written in the locations that are always accessible.

Fig. 3.6 shows the typical basic system interface for the ADSP-2189M: two serial devices, a byte-wide memory space and optional external program and data overlay memories. In the HEPD-DAQ framework, in addition to the already mentioned DPRAM (accessible with the external *data memory* page), the byte memory interface is used to connect the FRAMs and the SRAM and the I/O interface is used to access a dedicated space in the Main-FPGA.

The byte memory uses data bits 23:16 and address bit 13:0 to create a 22-bit address that allows up to 4 MB space. This size is enough to map the two 512 kB FRAMs and the 256 kB SRAM of the DAQ, as shown in Fig. 3.8. The choice to access the SRAM by

means of the BDMA space is due to the main characteristic of this circuit. It starts automatically once the destination/source address and length of the on-chip memory involved with the transfer are specified, and can work in parallel with other DSP operations. In case the processor needs the bus to access external overlay memory, this has priority over the BDMA accesses. The BDMA feature is also used to load the software code from the FRAM into the DSP program memory, once the DAQ board is powered on.

Programmable Wait-State[4] generation allows the processor to connect easily to all these slow peripheral devices.

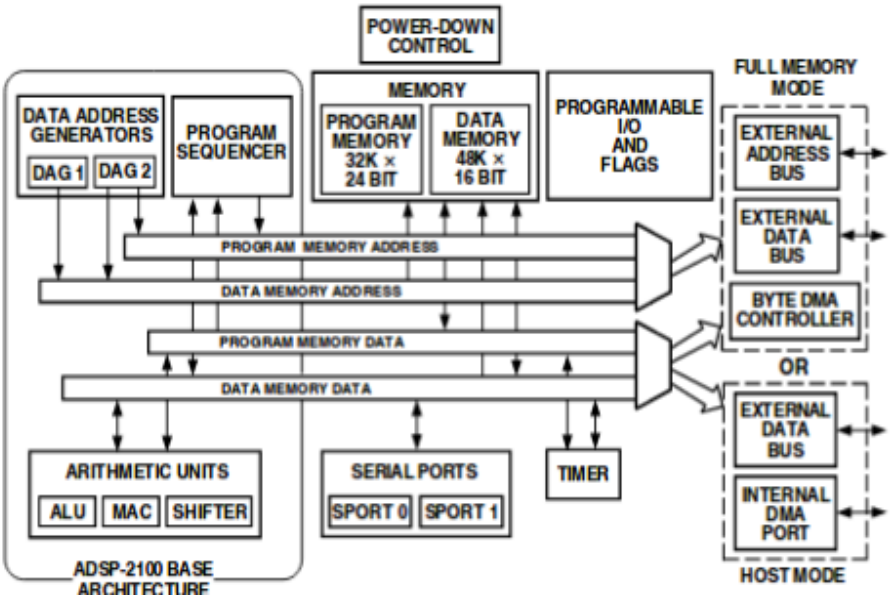

Fig. (3.5) *Functional block diagram of the digital signal processor.*

3.4.2 Main-FPGA and Download-FPGA

The Main FPGA, a Microsemi Actel ProASIC A3PE3000, is the core of the DAQ board. The choice of this FPGA was done considering the low cost, low power, and the security provided by the non-volatile flash memory incorporated. It is responsible for the general management and external interface of the board. In fact, it provides the interface for the CPU board, the trigger board and the front end electronics of the silicon detectors. It exports several registers to the CPU board (by the slow control link, as well as all the FPGA of the other electronic boards) and some registers to the DSP accessed by means of its I/O interface. It is also responsible for the acquisition of the silicon detector and the communication with the EASIROC board for the generation of the trigger pulse.

[4] A wait state is a delay experienced by a processor when accessing external memory or other type of devices that are slow compared to the processor.

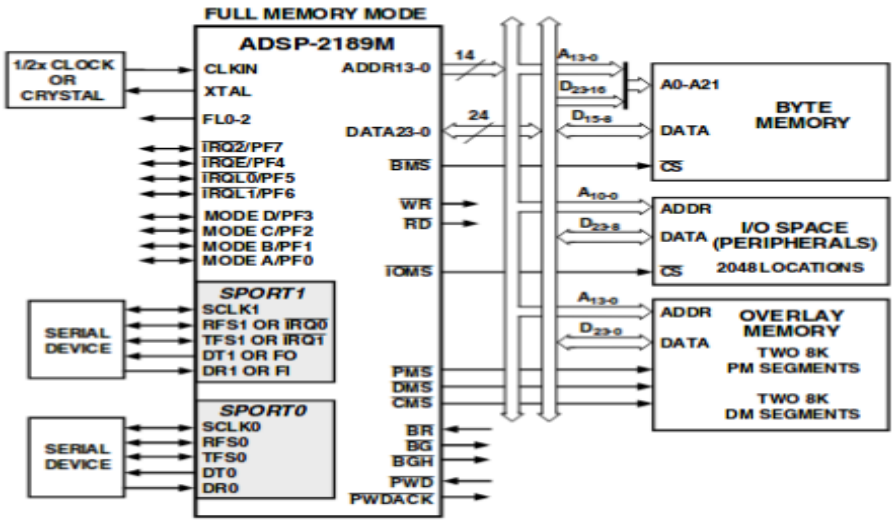

Fig. (3.6) *ADSP-2189M Basic system interface. The scheme shows the four external interrupt (IRQx), the two serial ports together with the address and data buses to access the memory spaces.*

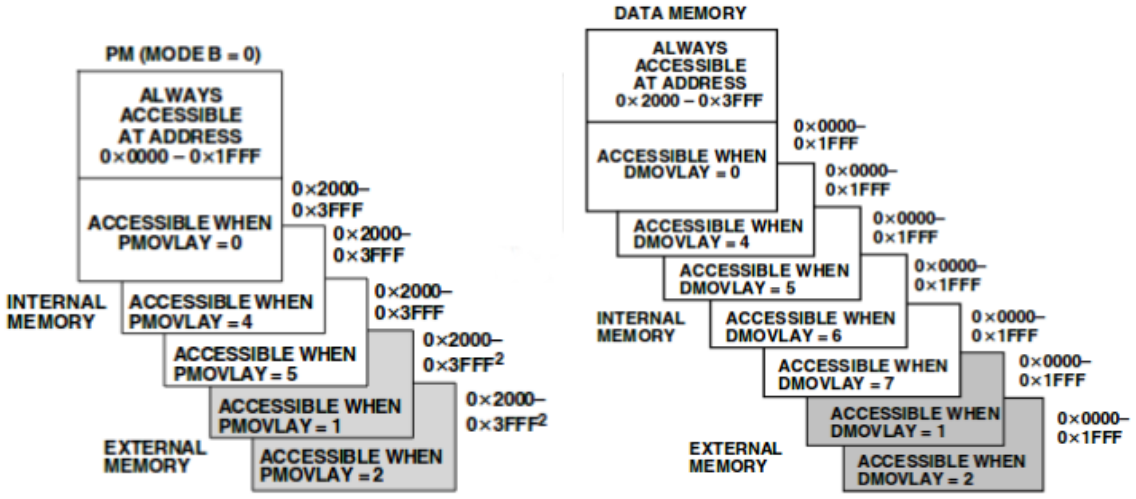

(a) *Program memory* **(b)** *Data memory*

Fig. (3.7) *Scheme of the program and data internal memories of the DSP, with the overlay page structure and relative addresses. The external pages are represented in grey. In the DAQ framework they are not used in case of the program memory, while an external data memory page is used to access the dual port RAM.*

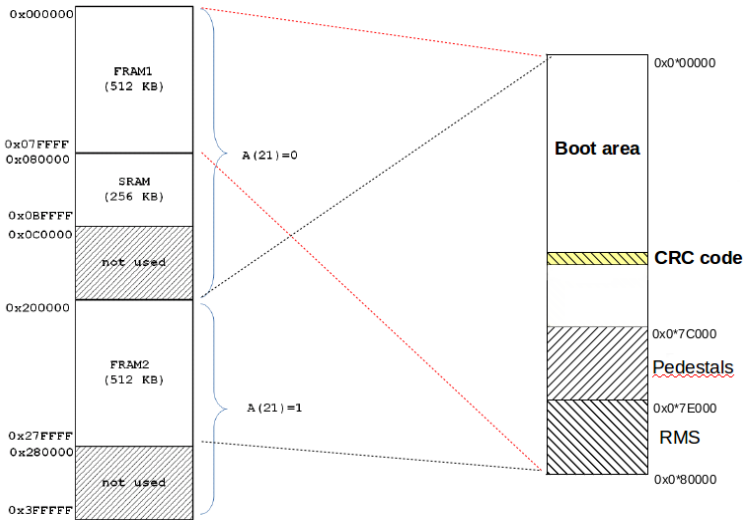

Fig. (3.8) *A scheme of the BDMA space usage for the DSP of the DAQ board. The 22-bit bus can address up to 4 MB that are mapped in the following way: at the first 512 kB there is the first FRAM (FRAM1), immediately after that there are the 256 kB of the SRAM and following an empty block the second FRAM (FRAM2) is present. The FRAM area is used to store both the DSP code and the calibration of the silicon detector.*

In Fig. 3.9 the internal functional block diagram of the Main FPGA is shown. It is divided into several blocks, each one with a precise task such as the acquisition of the silicon data (SI_BLOCK), the communication with the EASIROC (ER_BLOCK) and CPU boards (SPW), the monitoring of the DSP status (DSP_MON_FSM) and the write operation on the DPRAM memory (DPRAM_IF).

The Download-FPGA is a Microsemi Actel ProASIC A3P125, and it is used only to manage the SRAM scientific data buffer and to transfer the scientific data to the satellite via the RS-422 interface (see section 4.3.6.4 for details).

3.5 CPU Board

The CPU board is the digital subsystem that controls the detector status and communicates with the platform of the satellite via the CAN bus interface. The board manages the following functionalities:

- communication with the satellite computer (OBDH) via the 2x CAN bus interface (nominal and redundant);
- management of the Power Control board, the High Voltage control board, the EASIROC/trig-

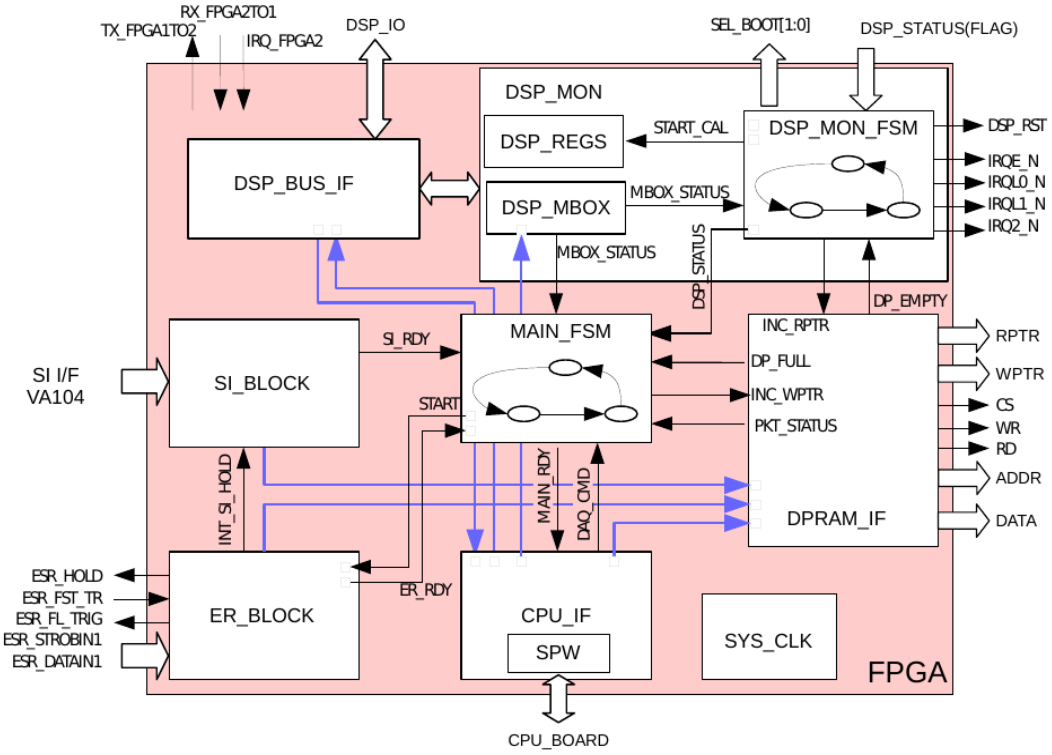

Fig. (3.9) *Internal block diagram of the Main FPGA of the DAQ board.*

ger board and the DAQ board, via internal slow control link bus;

- management of the system diagnostic routines and system configuration.

The main components of the board are:

- a FPGA (Actel ProAsic3 A3PE1500) for the safe boot management and the implementation of the slow control link;
- a digital signal processor ADSP-2189M;
- 2x CAN bus transceivers and 2x CAN bus controllers SJA1000T;
- a Read-Only EEPROM and a Read-Write FRAM used to store the application code for the digital signal processor.

Differently from the DAQ board, that contains two FRAMs, the two non-volatile memories used for the CPU are a RO-EEPROM and a RW-FRAM. This choice was taken for safety reason, since the EEPROM memory was not writable anymore, once the ELS was assembled and the EEPROM programmer was removed. In this way, the copy of the

program written on the FRAM, can be modified in a later time, while a tested and perfectly working copy is always accessible from the EEPROM memory. In order to simplify the development of the software, the digital signal processor, used in the CPU board, is the same included in the DAQ board.

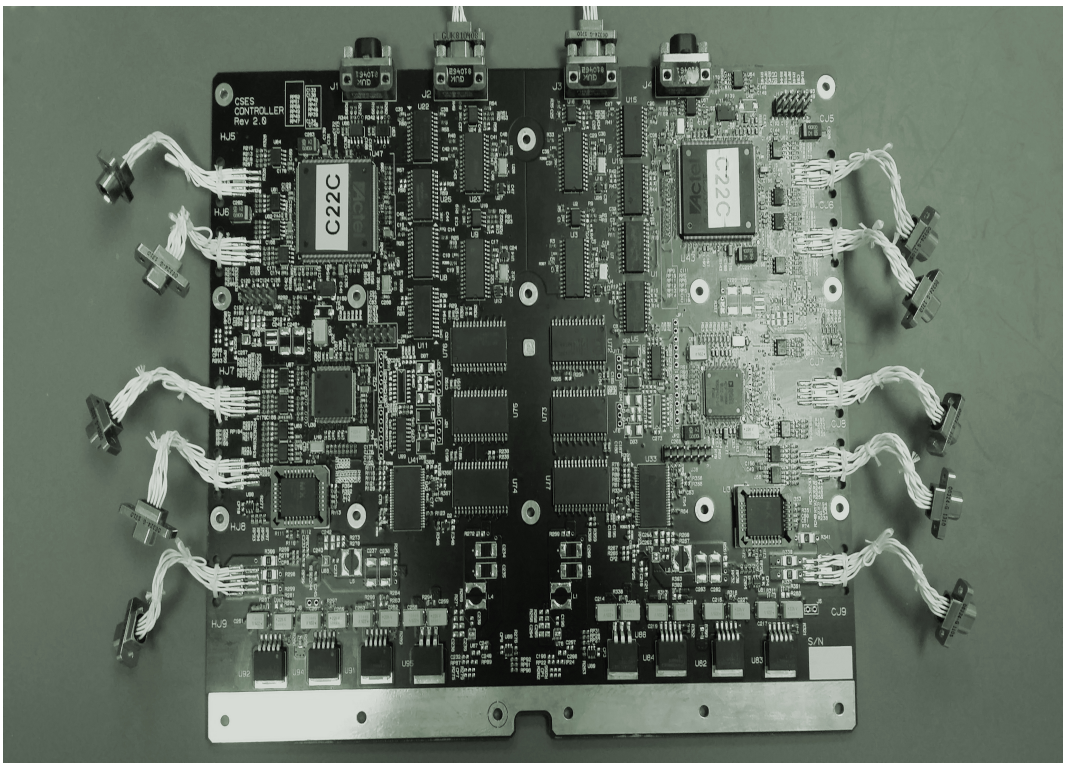

Fig. (3.10) *A picture of the CPU board.*

3.6 Trigger Board

The tasks of the trigger board are summarized as follows:

- acquisition of the 63 PMTs by means of the EASIROC chips;
- analog to digital conversion of the PMT signals and their transfer to the DAQ board;
- management of the trigger configurations and generation of the trigger pulse;
- generation of the fake trigger pulse for calibration purposes;
- measurement of the dead time and live time of the apparatus;
- measurement of the rate meter for each PMT and for each trigger configuration.

To provide all these features, each side of the board (hot/cold) is composed by a FPGA (Actel ProASIC A3PE1500), two EASIROC chips and four 12-bit ADCs.

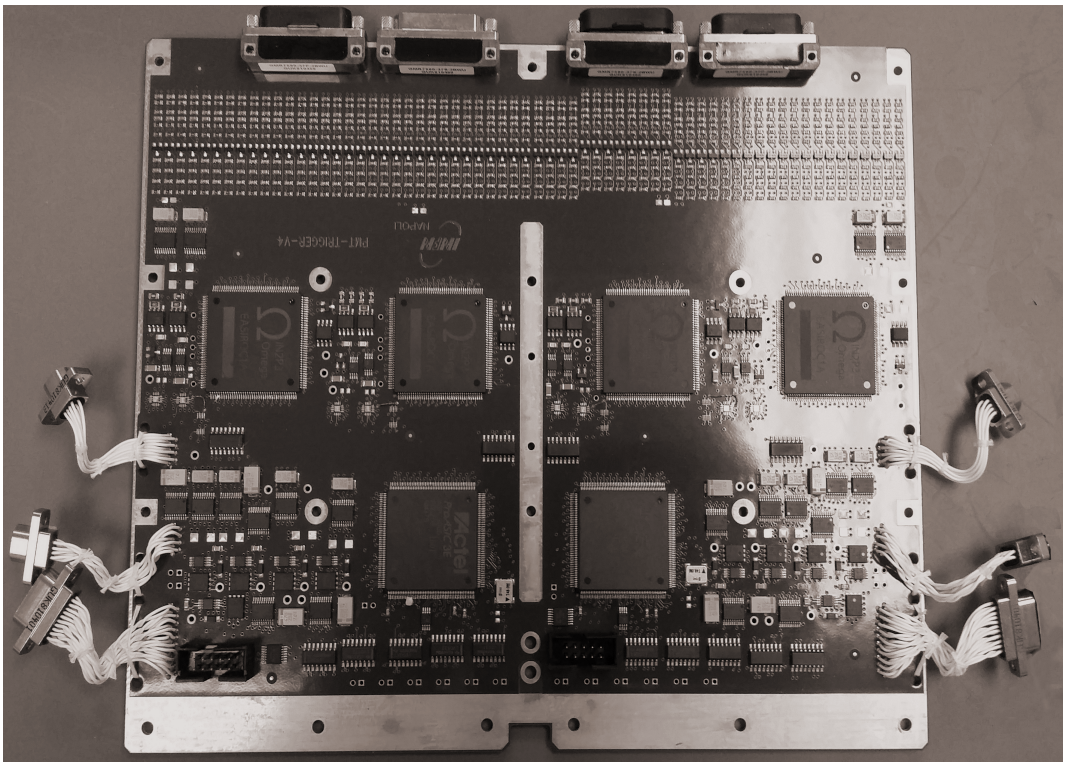

Fig. (3.11) *Picture of the EASIROC/trigger board.*

3.6.1 EASIROC Chip

The Extended Analogue SiPM Integrated Read Out Chips (EASIROC) is a 32-channel fully-analogue ASIC front end, dedicated to the read-out of SiPM or PMT detectors. For each channel, two parallel independently programmable variable-gain preamplifiers provide the low gain and the high gain output signals. The FPGA of the trigger board configures and manages the EASIROC in order to acquire the signals of all the 63 PMTs.

A trigger line is available from the high gain preamplifier and it is composed of a fast shaper followed by a discriminator. The output signal is then compared to this threshold, that can be set by an internal 10-bit DAC, and is in common to all the 32 channels. The determination of the threshold parameter has been obtained after several tests including acquisitions of cosmic muons and electrons at the DAFNE facility in Frascati (Italy). A detailed illustration of the internal EASIROC structure is reported in Fig. 3.12.

While the low and high-gain channels are multiplexed, the 32 trigger lines are available as a 32-bit output bus, and are used by the FPGA to decide whether the condition for

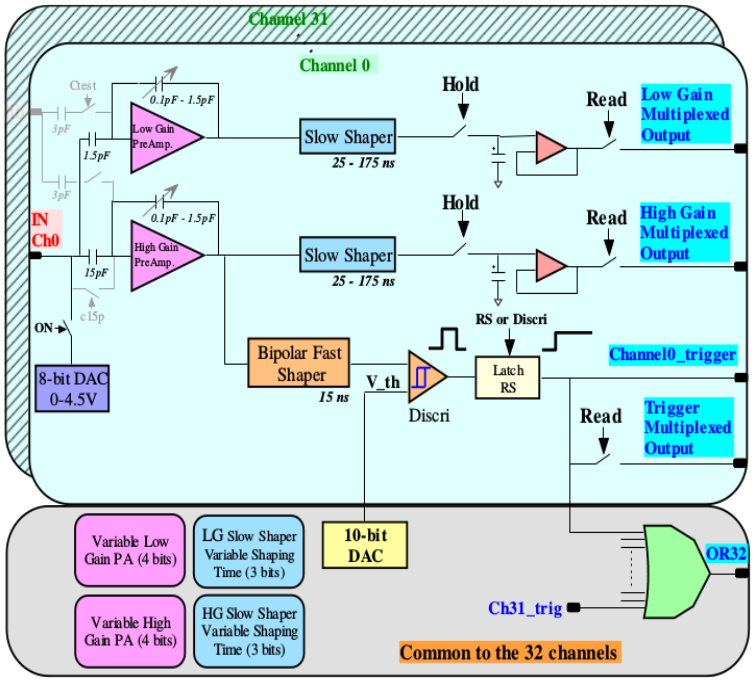

Fig. (3.12) *EASIROC chip internal structure for a single channel. The two chains for the low and high gain output can be noted, as well as the trigger line.*

the trigger signal generation is met or not. During standard operations, the selected active pattern is:

$$T \,\&\, (P1\, OR\, P2),$$

that means that the incoming particle must have produced an event signal on at least one PMT of the 12 forming the segmented trigger plane, and at least one PMT from the 4 connected to the first two calorimeter planes. There are other predefined trigger patterns, given by possible OR/AND combinations of the various PMT output that are intended for specific tasks. In Tab. 3.1 all the 8 existing configurations are reported. For example, by using the number 3 configuration ($(T3\, OR\, T4) \,\&\, (P1\, OR\, P2)$), it is possible to reduce the detector acceptance by selecting only the two central paddles of the trigger plane. On the other hand, selecting a configuration containing a signal condition on a deeper plane (like number 5 and 6 configurations of Tab. 3.1) would allow to select only more energetic particles since we are increasing the energy threshold for the detection.

It must be noted that each of these configurations can be considered:

- without veto;
- with lateral veto;
- with bottom veto;

Predefined trigger patterns	
0	T
1	T & P1
2	T & (P1 OR P2)
3	(T3 OR T4) & (P1 OR P2)
4	T & P1 & P2
5	T & P1 & P2 & P3
6	T & (P1 OR P2) & (P15 OR P16)
7	T & (P1 OR P2) & L

Table (3.1) *The eight predefined trigger configurations for the HEPD detector: T = OR of the 12 PMTs of the segmented trigger plane; T3 = OR of the 2 PMTs of the first trigger paddle (and the same for T4); P1 = OR of the 2 PMTs on the first calorimeter plane; L = OR of the 9 LYSO crystals.*

- with the whole veto (lateral + bottom).

In this way, a total number of 32 possible trigger configurations is generated. In addition to these 8×4 predefined configurations, a further pattern can be defined by any 'AND' combination of the plane signals. It is also possible to exclude bad/not functioning PMTs from any trigger configuration, by means of a PMT mask register implemented in the trigger board FPGA.

In addition to the possibility to select any possible combinations of output signals to generate the trigger condition, the measurement of the single PMT rate meters and trigger configuration rate meters performed by the FPGA allows to select the best possible trigger pattern for all the needs, and to change it according to the expected event rate.

It is important to note that, always for redundancy reasons, the two PMTs placed on the same scintillator plane/paddle are an input line for a different EASIROC chip. In this way, with the exception of the LYSO plane where each cube is read-out by only one PMT, a problem on an EASIROC chip does not totally affect the apparatus functioning.

3.7 Power Control Board and High Voltage Board

The power control board (or control low voltage board) provides the 'digital' voltages for all the other components of the ELS. The board is divided into the usual hot/cold sides, and a common section that includes the connector for a direct link with the satellite. The platform uses this to send the direct STAND_BY_ON, STAND_BY_OFF and RESET hardware commands to the HEPD. The logic of the board is implemented on an Actel FPGA (A3P125).

The High Voltage board, is instead responsible for the voltage output for the HEPD detectors. It is composed by a scintillator section, formed by 10 HV modules (that provide a voltage between 750 and 900 V), and a silicon section, formed by 2 HV modules (that provide 65 V), one for each plane.

3.8 Front-End Electronics for the Silicon Detector

The requirements of the front-end (FE) electronics for the silicon tracker are to keep the power consumption low and to minimize the noise contribution. The FE of the HEPD includes two different components: the hybrids, two for each silicon ladder (for the S-side and the K-side), and the FAN-IN/FAN-OUT boards, one for each silicon plane. The hybrid circuits are integrated within the detector ladder, while the FAN-IN/FAN-OUT are a dedicated printed circuit boards positioned in the vicinity of the planes.

The first stage of the FE electronics is composed of 12 dedicated VA140 chips [43] from IDEAS company [44], placed on each hybrid circuit (6 for the S-side and 6 for the K-side). The VA chip (see Fig. 3.13) contains 64 low noise and low power independent acquisition chains and an internal multiplexer and shift-register for the sequential read-out of all the input channels. Each chain is composed by a charge sensitive preamplifier, a shaper circuit and a sample/hold circuit. The total number of channels amounts to 64 (VA) $\times$ 6 (VA per hybrid) $\times$ 2 (hybrid per ladder) $\times$ 3 (ladder per plane) $\times$ 2 (plane).

The FPGA of the DAQ board manages all the phases of operation for the VA chips and controls the digital input lines (*hold, reset, clock, shift-in*) required to control the internal operation of the VA140.

The FAN-IN/FAN-OUT boards constitute the interface between the silicon tracker and the rest of the HEPD system. The board functionalities are:

- to pass high-voltage lines from the HV board to the hybrid circuit;
- to pass low-voltage lines from the Power Control board to the hybrid circuit;
- to pass digital signals from the DAQ board to the hybrid board;
- to enable high voltage and low voltage power for the *i-th* column.

In Fig. 3.14 and 3.15 two pictures of the FE electronics are reported: the first one shows a silicon ladder connected with its hybrid circuit; the second one shows a FAN-IN/FAN-OUT board connected to the 3 hybrid circuits of a silicon plane.

The read-out of the silicon data happens one column at a time, where with the “column” term we refer to two ladders of different planes and with the same X coordinate (with reference to Fig. 2.2 (a)). The DAQ board handles the enable line for the columns and starts the read-out from the top ladders to the bottom ones.

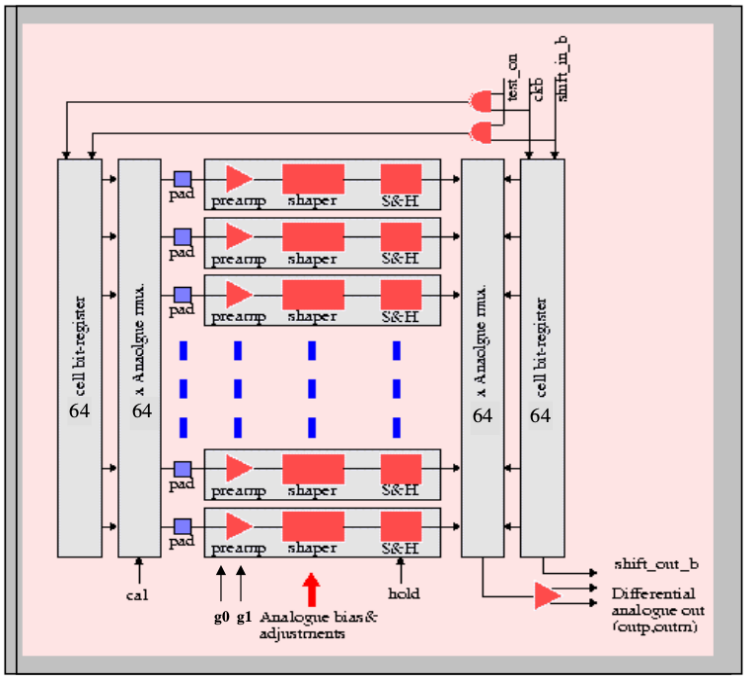

Fig. (3.13) *A scheme of the VA140 chip architecture.*

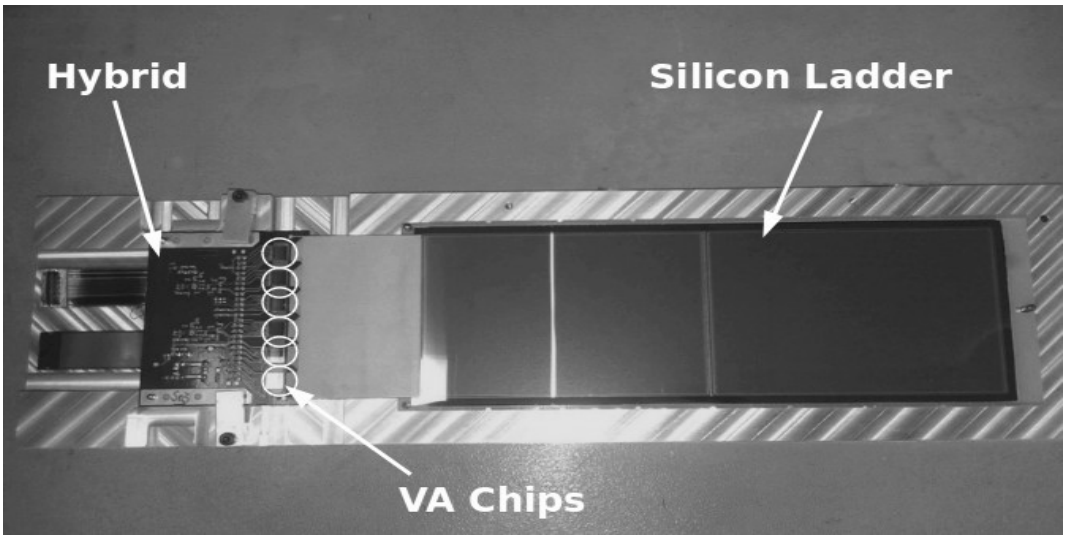

Fig. (3.14) *A picture of a hybrid circuit integrated on a silicon ladder.*

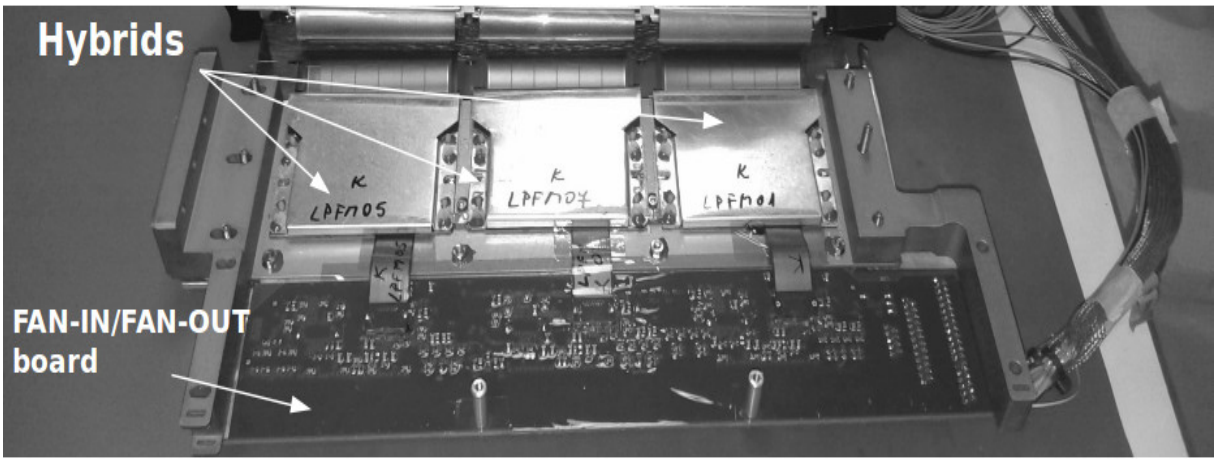

Fig. (3.15) *A picture of a FAN-IN/FAN-OUT board connected to a silicon plane with the three hybrids. The hybrids are covered by an aluminum protection box.*

The DAQ includes 8 ADCs for the digitization of the silicon data, that work in parallel. For this reason, the 6 VA chips, included in a single hybrid, are divided into two blocks, each of 3 VAs, that are read-out at the same time. Fig. 3.16 shows the read-out chain for a single column: two ladders (external and internal plane) are represented. The blu lines illustrate the 384 read-out strips of the S-side including the bonding between two silicon sensors. The 6 VAs of the S-side (represented by the blue squares) are divided into two block (va1 to va3 and va4 to va6) and their outputs are directed towards two different ADCs (aout1 and aout2). The orange lines illustrate the 1152 read-out strips of the K-side, read-out in blocks of 3 strips as described in section 2.1. The division of the 6 VAs of the K-side hybrid works in the same way as the S-side. The acquired data are written in a FPGA FIFO as shown on the right side of Fig. 3.16.

3.9 Development and Qualification of the ELS

A first prototype of each board (called *engineering* model) was initially developed and tested before the production of the qualification and flight versions. After this test phase, the qualification version, with improvements and corrections on the board layouts, was completed. The functioning of the QM-ELS were also tested in the temperature range $-30°C \div +50°C$, by means of a thermal chamber at the NEAT srl Company [45] (the company that built the CPU board). Then, the QM-ELS was assembled with the detector in order to have a perfectly working qualification model of the HEPD. As better described in chapter 5, the whole QM apparatus (ELS+detectors) was tested in a thermal chamber, thermal-vacuum chamber and with vibrational tests. After this, it was delivered to China and tested on board the CSES satellite.

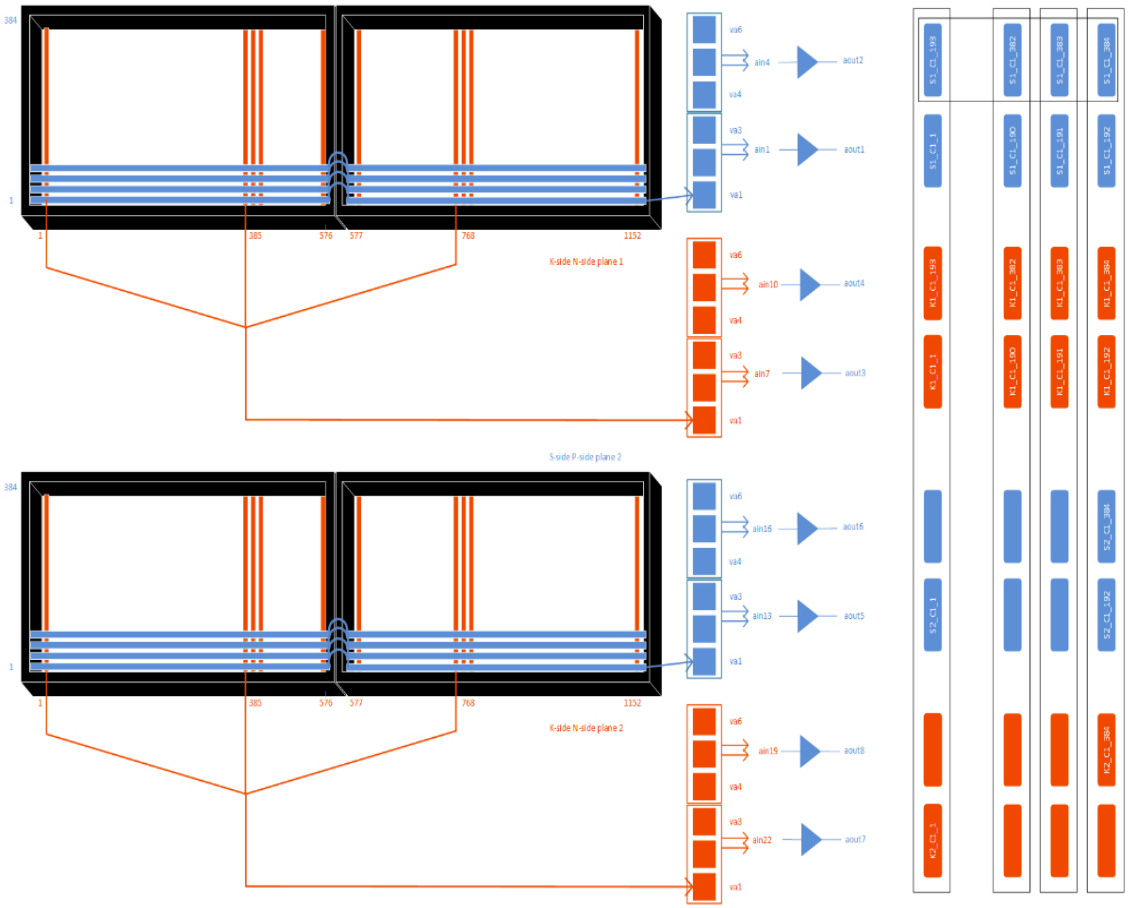

Fig. (3.16) *A scheme of the read-out chain for the silicon detector. The blu lines represent the read-out strips of the S-side and the orange lines represent the read-out strips of the K-side. The figure illustrates the parallel read-out of one silicon detector column (two ladders of different planes). The aout1... aout8 signals represent the 8 input signals for the 8 ADCs of the DAQ board.*

Finally, the last version of the electronics boards (the flight version), carrying minimal variations with respect to the qualification model, was developed, tested and integrated in the flight model of the HEPD detector. After the tests with the satellite in Beijing, the QM was delivered back to Italy, and it is now in the Roma2 “Tor Vergata” clean-rooms. It was opened and the ELS was updated to the same version as in the flight model and can be used for further tests and measurements.

Chapter 4

Control and Data Handling Software

During my Ph.D. I spent a lot of time in the development of the software for the digital signal processors of the HEPD detector, and in its optimization and test, particularly during the integration of the apparatus.

It must be noted that the development of a software for an experiment on board a satellite is very different with respect to a case where is always possible to access the hardware and modify the software afterwards. Although I foresaw the possibility to update the software once the satellite will be in orbit, this is a very delicate operation. As will be shown in detail in section 4.2.1.3, some tele commands can be sent from the ground stations to the satellite for different purposes, including the update of the online software. Each one of these commands has a dimension of few bytes, while the whole software size is around 30 kB for the CPU and more than 100 kB for the DAQ. This means that thousands of commands are required for an update, and an error on a single bit can affect the HEPD functionalities. Consequently, an intense phase of tests is strictly required and all the possible sources of errors must be contemplated and managed, as well as all the specific case that can cause a break of the normal execution.

I took part in the development and test of the CPU software and in particular I was in charge of the development of the DAQ software for the data acquisition and the in-flight data handling.

The software is written in *C* language, with few assembly instructions. The used environment includes:

- the ADSP-2189M EZ-KIT Lite, with VisualDSP++ v. 3.5;
- the EZ-ICE emulator.

The ADSP-2189M EZ-KIT Lite is an evaluation board from Analog Devices that includes the same DSP the HEPD uses in the DAQ and CPU boards, one external *interrupt* connected through a push button switch, and a 4 Mbit Flash memory where the program

can be stored and loaded by the DSP. After a phase of test lasting a few months with this hardware configuration, I started working directly on the engineering model of the HEPD electronics.

VisualDSP++ is the IDDE (Integrated Development and Debugging Environment) provided by Analog. It allows a direct access to the DSP internal memory and registers by means of a graphic user interface.

The EZ-ICE emulator system provides a controlled environment for observing, debugging and testing activities in a target system by connecting it directly to the target processor through the interface port.

The main tasks of the HEPD software are described in the current chapter with different sections dedicated to the CPU and the DAQ boards.

4.1 Electrical Model

The software of the Electrical Model was a preliminary version of the HEPD online software with reduced functionalities. It was developed to test the communication with the satellite via the CAN bus and RS-422 links, and to emulate and manage the data produced during in-flight operation, because of the absence of the detectors. All the interfaces with the hardware components, such as the two SJA1000 CAN controllers, were handled by the processor linux kernel. The most intense part of my work was to define and implement the protocol for the CAN bus link and to test the timing requirement of the communication. I also performed the test of the EM at the DFH Company Ltd[1] (in Beijing) with the electrical model of the satellite. In the current chapter, I will specifically focus in the description of the final version of the software developed for the flight model.

4.2 CPU Software: TM/TC and HEPD monitoring

As described in the section 3.5, the main components of the CPU board are the digital processor ADSP2189M and the controller FPGA. The DSP of the CPU board is in charge to manage the functionalities of the whole HEPD detector, by monitoring the status of the apparatus and also handling the communication with the CSES satellite.

Two main protocols have been developed to address all these tasks, and will be described in detail in the next paragraph:

- slow control management;
- CAN bus management.

[1] The company responsible for the CSES contruction.

The slow control is the link used for the communication between the electronics boards of the HEPD. By means of the slow control, the CPU board has to verify the correct status of all the other boards and to handle all the potential error conditions.

The CAN bus instead, is the link used for the communication with the CSES satellite.

4.2.1 DSP Software

The architecture of the software for the CPU can be summarized in different modules: a boot loader responsible for the correct initialization of the CPU, some drivers for the management of the physical buses and a main application loop responsible of the HEPD working procedures.

4.2.1.1 Boot and Main Loop

The CPU board uses two different non-volatile memory elements to store the program: a FRAM and a EEPROM. The substantial difference between them is that the FRAM can be written by the DSP while, in order to write data on the EEPROM, an external tool is required, and it can not be done after the final assembly of the HEPD electronic subsystem.

At the power-on of the board the DSP will start automatically the upload of the program application from the FRAM memory to its internal RAM, by means of its Byte Data Memory interface. This feature is provided by the DSP itself by properly configuring the BDMA port. If the upload is successful, an FPGA watchdog that forces the boot from the EEPROM will be disabled. In case of a failure in the boot, the FPGA will set the EEPROM to be the source for the upload.

The previous boot status of the system is saved in the FRAM memory as well. It will be restored as soon as the boot is completed, in order to set the HEPD in the same configuration before the precedent power-off. This configuration is saved in two different location on the FRAM with a CRC code (see 4.3.7) to check the correctness of the data. In case both configurations result corrupted, a predefined configuration saved in the program application is used.

Immediately after the boot, the program running on the CPU is responsible of the complete power-on of the HEPD; DAQ, PMT and HVPS boards, as well as high voltages for PMT and silicon detectors, are powered on with a proper sequence, and their status and basic functionalities are checked. Once the system is in the nominal status, the main loop of the application is started.

During the main loop the software cyclically invokes several functions as reported in Fig. 4.1. As can be noted, there is a function in charge to take care of each electronics board of the apparatus. During the execution of these board control tasks (cpu_task,

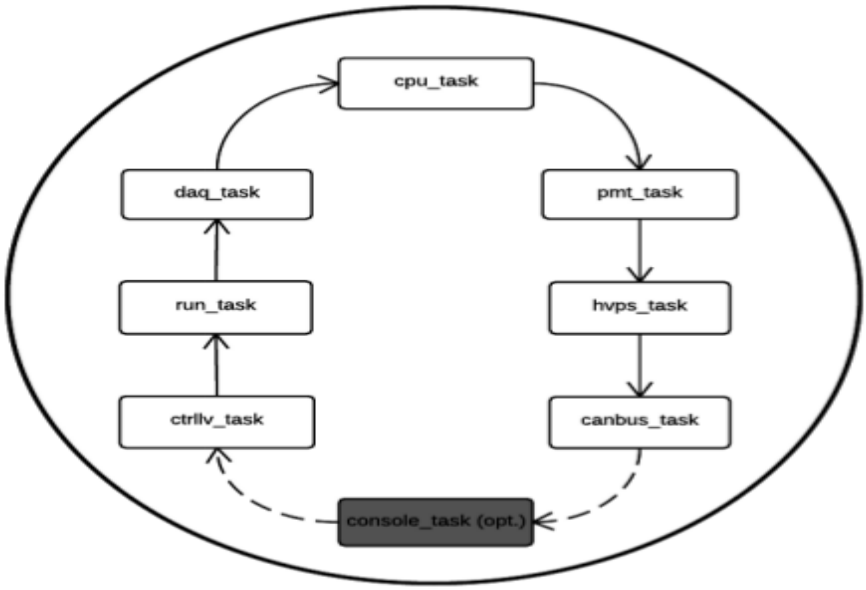

Fig. (4.1) *Scheme of the main loop for the software running on the DSP of the CPU board. All the tasks are cyclically executed according to this order.*

daq_task, pmt_task, $hvps\_task$ and $ctrllv\_task$), the CPU checks the status of the whole electronic system by reading, via the slow control protocol, specific registers mapped in the FPGA present in each board. In the same time the CPU updates the configurations and collects information from the other boards that will be sent to the satellite via the CAN bus link in specific packets called *telemetry*.

The run_task, instead, is responsible of the start and stop acquisitions or calibrations for the detector. During this task the CPU properly configures the apparatus, and sets the DAQ and trigger boards in an acquisition state. The operations during this tasks will be better discussed in the section of the DAQ software.

Besides these operations repeated in the main loop, there are some occurrences that can cause the interruption of the task the DSP is executing, to accomplish a more urgent operation. These occurrences, mainly related to a new message from the satellite, will generate an *interrupt* signal for the DSP.

4.2.1.2 Slow control link

The slow control link is used for the communication between the different HEPD electrical boards. The channel is based on the SpaceWire Light[2] standard where the controllers

[2]The SpaceWire is a spacecraft communication network coordinated by the European Space Agency in collaboration with international space agencies. The nodes of the network are connected through a serial link with low latency and allowed speeds between 2 Mbits/s and 400 Mbits/s.

are implemented in the FPGA present in every board. The DSP accesses a register map in the CPU-FPGA by means of the I/O memory interface. Four channels are provided to manage the DAQ board, the HVPS board, the Power Control board and the PMT board; specifying the correct channel the DSP can access the reserved register area dedicated to the slow control and write on those registers.

During the power on of the HEPD, the Power Control board and the CPU board are automatically powered on, then the DSP will access the FPGA of the Power Control board by means of the slow control link and will force the power on of the other electronics components.

In the main loop application the slow control link is continuously used to read the status and error register and to configure each board.

4.2.1.3 CAN bus protocol manager

One of the main tasks for the DSP of the CPU board is to manage the CAN bus protocol, the link used by the CPU to communicate with the satellite. In fact, all the payloads on board the CSES satellite can be considered a node on the CAN network.

The CAN bus is a serial bus with a multi-master architecture, mainly used in the automotive framework. The CAN specifications use the concept of dominant and recessive bits to establish the priority of a message. This means that if a node connected on the bus transmits a dominant bit (0) and another node transmits a recessive bit (1), the dominant bit ”wins” and there is no delay for the transmission of the higher priority message. The transmission of the lower priority message will be stopped and resumed after the message with the higher priority is received.

In Fig.4.2 an example of a CAN bus frame is illustrated, according to the standard format CAN 2.0 used in this implementation. The frame is composed by an identifier field (ID) that represents the message priority (green), four bits for the data length (yellow) and eight bytes for the data field that compose the message (red). The light blue field is a bit used to specify if the current frame is a data frame or a request frame, i.e. a message sent by a node to request some data from another node in the network. In the framework of the HEPD-CSES communication, this bit is always set to 0 (no request frames are available). The colored fields in the figure are the ones that can be modified by the software, while the other bits are automatically set by the CAN controller SJA1000 on the CPU board.

Although the CAN bus is thought to be a multi-master bus, in the framework of the HEPD-CSES communication the satellite is considered as the only master, and the HEPD can send messages on the CAN bus only in response to a precedent message from the satellite. The identifier field of a CAN frame is used to specify the payload that is sending the message. Considering the priority discussion previously mentioned, in order to have the highest possible priority while sending a message, the satellite system has an ID of

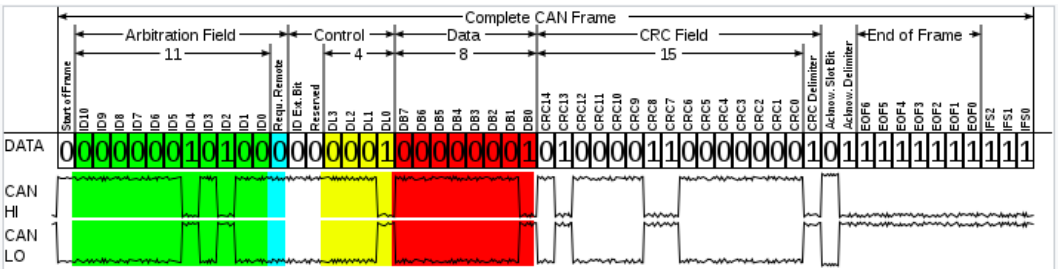

Fig. (4.2) *Example of a CAN bus frame. The first bits (green) represent the identifier and also the priority of the message, then there are 4 bits for the data length (yellow) and 8 bytes for the data field (red). The colored fields are the ones that can be modified by the software, while the rest of the frame is filled by the CAN bus controller SJA1000.*

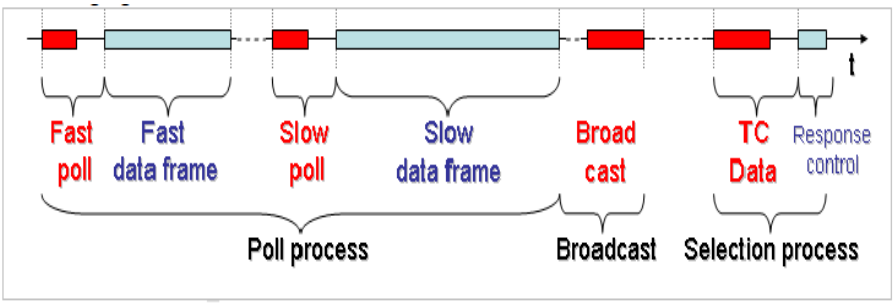

Fig. (4.3) *Scheme of a transmission on the CAN bus link. In red are represented the frames sent by the satellite, in light blu the response of the HEPD.*

eleven bits all set to 0.

The scheme illustrated in Fig.4.3 shows the transmission between the satellite and the HEPD during the in-flight operations. The red blocks represent packets sent from the satellite, while the blue blocks represent the HEPD response.

The link has to manage three different kind of packets:

- Tele Commands (TC data);
- Telemetry sequence (Slow poll/Fast poll);
- Broadcast Data.

Tele commands are used to power-on and configure the HEPD and are divided in single or multi-frames depending on the number of CAN frames that compose the command. Each TC contains an error detecting code at the end of the message. After receiving a TC

Fast Telemetry Data Content		
FIELD	**Bytes**	**NOTE**
Frame Counter	4	Number of frame sent to the satellite via RS422 (see 4.3.6.4). Used to correlate telemetry data with scientific data[3].
CPU Board Status Error	4	Status of the CAN bus, slow control link and Finite State Machine of the CPU
DAQ Board Status	2	Status Register of the DAQ board
Trigger Board Status	2	Status Register of the Trigger board
Power Control Board Status	2	Status Register of the Power Control board
HVPS Board Status	2	Status Register of the HVPS board
HVPS Status	2	One bit every DC/DC module (1 = error)
HEPD Status	2	Error Register of every board

Table (4.1) *Fast Telemetry Data Content*

the CPU has to verify the code and, whether this is correct, sends back to the satellite an acknowledge message and executes the command.

Telemetry sequences are used by the satellite to periodically collect information about the status of the HEPD detector. There are two possible processes: *fast poll* and *slow poll* that are sent with a cycle of 1 and 8 seconds respectively. When a telemetry request is received, the DSP of the CPU has to respond to the request within a fixed time window. These telemetry packets contain information like the value of the temperature sensor placed on the CPU and trigger boards, the status and error registers for each electronics board, the monitored values of the high voltages for the PMT and silicon detectors, or the last tele command received.

The format of the telemetry packets was decided in order to have the possibility to monitor the status and the operation of the HEPD detector during its working. All the acquired telemetry will be transmitted from the satellite to the ground stations once a day. It is really important to have frequent information about the status of the HEPD apparatus over time, in case there will be the necessity to investigate a possible source of malfunction or unexpected behavior.

In Tab. 4.1 the data content of the fast telemetry message is reported. The slow telemetry, that is sent with a lower frequency, contains more information like all the monitored values for the PMTs and the silicon planes.

The last type of data transfered by means of the CAN bus link are the broadcast. They are packets the satellite sends to all the payloads with information about position, velocity, time and attitude configurations of the satellite itself.

Two pieces of broadcast information (latitude and longitude) are used by the DSP to calculate the position of the satellite, in order to decide the next operation (run or calibration) and the correct configuration of the apparatus. They are also sent to the DAQ that uses them to fit the header/tail structure of each acquisition run.

Two physical buses (CAN bus A and CAN bus B) are used for the CAN communication for redundancy reason. Nevertheless, only one bus must be active at a certain time.

Rigid requirements must be observed on the timing response on the link because it is used for all the payloads to communicate with the satellite. Fig.4.4a and 4.4b show the time windows for the response to telemetry data and tele commands. A telemetry message is composed by multiple CAN frames; in particular, it has been decided to send 20 bytes of data for the most frequent fast telemetry message, and 100 bytes for the slow telemetry message. As shown in Fig. 4.2, the data content on each frame is 8 bytes long, that means at least three CAN frames are required for the fast telemetry and at least thirteen CAN frames are required for the slow telemetry message[4]. According to Fig. 4.4a, T1 is the time between two consecutive frames of a telemetry packet and it must be in the range 0.2 ms $<$ T1 $<$ 0.6 ms. T2 is the time between the telemetry request from the satellite and the first frame of the HEPD response, and it must be in the range 0.2 ms $<$ T2 $<$ 2 ms. T3 is the time between the last frame of a tele command sent from the satellite and the HEPD acknowledge response, and it must be in the same range as T2.

One of the tasks of the CPU-DSP is to control the flow and the timing of data exchange on the BUS. In order to manage the CAN bus, the registers of the two CAN bus controllers (A and B) are memory mapped in the FPGA memory. The DSP uses the I/O space interface to access and configure these registers.

The FPGA provides also two interrupt signals (one for each CAN bus) for the DSP to report the presence of a new message.

A third interrupt is used and generated by the DSP itself to control the timing T1, T2 and T3. A dedicated register of the DSP (TCOUNT register) decrements every n processor cycles and, when it reaches zero, the interrupt is generated and the count register is reloaded. The use of the timing interrupt is necessary to address the time requirement of the communication.

In Fig.4.5 the operations handled by the CAN bus manager application developed for the DSP, are illustrated. When a new message arrives, an interrupt is sent to the DSP and a specific function is invoked. The first operation is to interpret the received message and

[4]To be more precise the HEPD sends 4 frames for fast telemetry and 15 frames for slow telemetry. In fact, it must be considered that, in the 8 byte space of each CAN frame, there are also some auxiliary information like frame index, frame checksum etc.

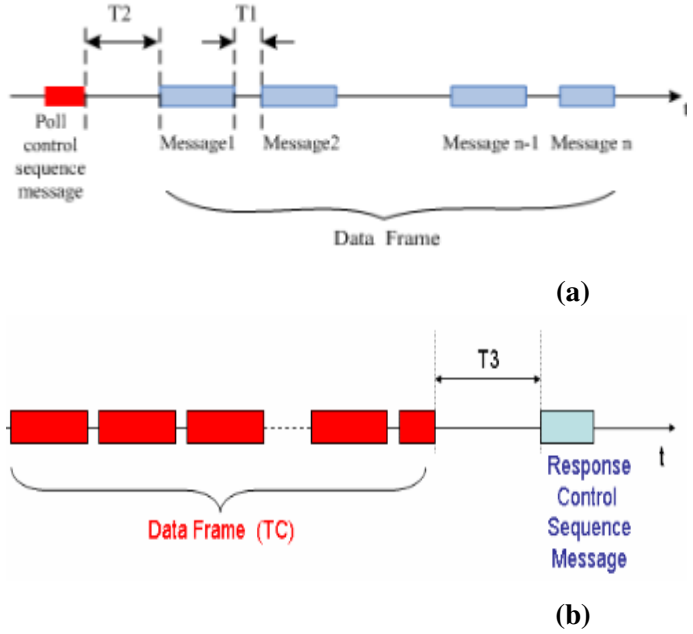

Fig. (4.4) *Scheme of the telemetry (a) and tele commands (b) transmission between the satellite and the HEPD detector.*

distinguish the case of telemetry, tele commands or broadcast data. In case of a broadcast packet, no response is needed and the data are saved on the internal RAM. These data are used to calculate the position of the satellite in the cpu_task in Fig. 4.1, in order to set the correct configuration for the next acquisition run. They are also sent to the DAQ board that uses them to complete the header and tail packets of the runs.

In case the received message is a slow/fast poll request, the TCOUNT register of the DSP is configured to assure the T1 and T2 timings (shown in Fig.4.4a) in the correct range. The telemetry packets are saved in the DSP internal RAM and they are updated in the main application loop every time a board task is invoked. When TCOUNT reaches 0, the telemetry packets are sent.

The case of tele commands is handled in a similar way as the telemetry. After the tele command is received, the TCOUNT register is set, the acknowledge packet is sent and the command is stored in a circular buffer. Later these command will be executed, in the same order they are received, when the $canbus\_task$ (Fig.4.1) is invoked in the main loop of the program.

The interrupts are used only to comply with the timing requirements of the CAN bus, while all the other tasks are executed in the main loop.

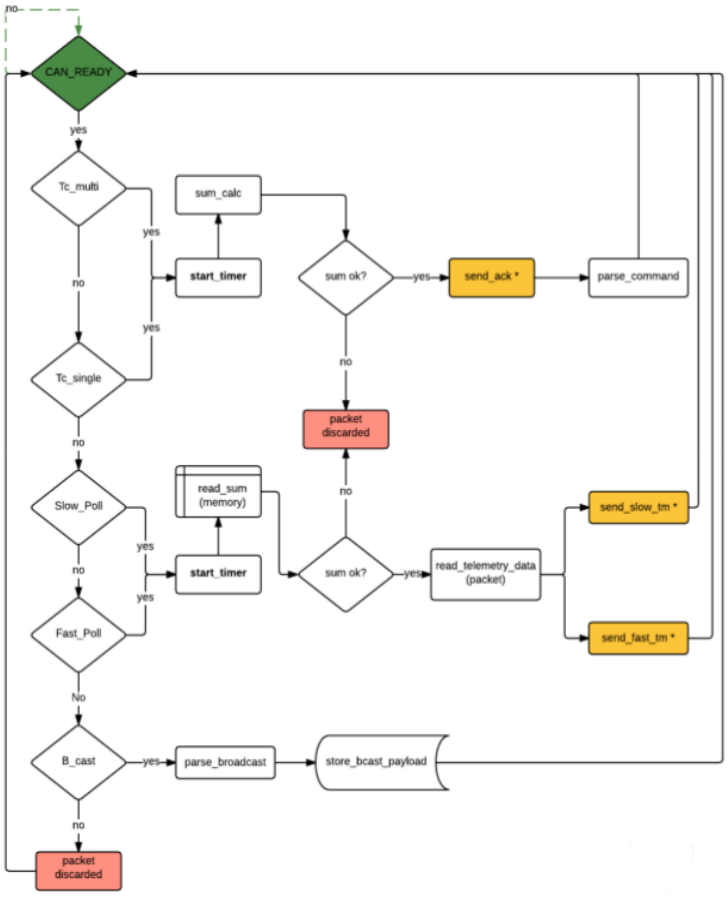

Fig. (4.5) *Scheme of the operations performed by the DSP when a new CAN packet is received. The first operation is to interpret the message (tele commands, telemetry or broadcast), then to verify the correctness and finally to execute the instruction. In case of telemetry or tele commands the timer interrupt is configured to guarantee the response message in the correct time window.*

4.3 Data Acquisition Board Software

The DAQ board is the digital subsystem responsible for the silicon data acquisition, the processing and the management of the scientific data[5] and their format and transmission via the RS-422 channel. The DAQ board manages the following main functionalities:

- configuration of the silicon detector;
- configuration of the acquisition mode;
- management of trigger signal from the trigger board;
- acquisition of silicon plane data and relative signal processing;
- scientific data compression (silicon data) and formatting (silicon + PMT data);
- transmission of the scientific data to the satellite via the RS-422 link.

To achieve all these tasks, a combined work between the two FPGAs and the DSP is required. The DSP is more focused on the computational operations, while the main FPGA has to control the correctness of the flow of all the operations and to monitor the DSP status.

Most of the operations are performed by the DAQ during the two run modes: acquisition and calibration.

4.3.1 Trigger Mechanism

The generation of the trigger pulse is one of the tasks of the trigger board when the HEPD system is in the acquisition mode. However, in order to decide if a new trigger must be accepted, a communication between the DAQ and the trigger board is required. In Fig. 4.6, a scheme of the trigger pulse generation is illustrated.

The standard operation implies that the trigger board sets its fast trigger line to 0 after the trigger reception, then the DAQ responds by setting the hold line to 0 and resetting the line to 1 only at the end of the internal processing of the read-out data. The trigger board does not generate other trigger pulses, until this hold line is returned to 1. During the event processing the trigger board also sends the data acquired from the PMTs to the DAQ. The first level trigger signal (ESR_FL_TRIG_N in the figure) is used by the DAQ in response to the fast trigger to report that the board is ready to receive data. The busy signal (ESR_BUSY_N) is used by the trigger board to start/stop the transmission of PMT data. A timeout of 210 μs is used for this data exchange via a data strobe link that will be described in the next section.

[5]The data from the detectors collected during the acquisitions.

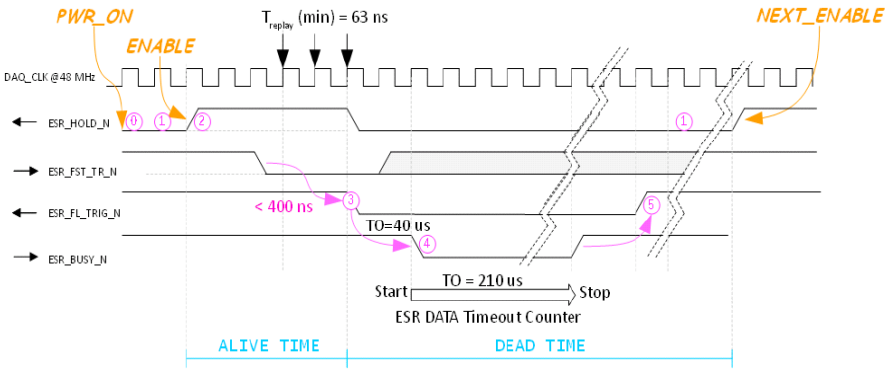

Fig. (4.6) *Scheme of the trigger generation. Right arrows are signals coming from the trigger board to the DAQ, left arrows are signals from the DAQ to the trigger board.*

The time elapsing from the assertion to the end of the hold signal represents the dead time of the apparatus, during which the HEPD is not able to process further physics events. This time is fixed in case of a *virgin run* acquisition, where all the data from the silicon detector are acquired and sent to the satellite without being processed. It varies for each single event in case of a *zero suppressed run*, where a compression algorithm is used in order to reduce the size of the transmitted data.

A more precise discussion on the dead time is presented in section 4.3.8.

4.3.2 Data Strobe Protocol

The data/strobe serial protocol has been specifically adopted for the communication between the DAQ and the trigger board mainly because of its advantages in terms of power consumption with respect to other available serial standards. The necessity of a serial link is clear considering the presence of many electronics boards, segmented into hot/cold redundancy sections, and the consequent request of a large number of links. In fact, the adoption of a serial protocol instead of a parallel one, yields to a drastic decrease in the number of wires and connections, and to a reliability improvement.

On the other hand, the use of a serial communication for the data transfers, affects the overall dead times during the acquisition with respect to a solution with a parallel data exchange, but the data exchange on the data/strobe link is a small contribution to the total dead time while the main contribution is due to DSP operations.

The data/strobe serial transmission needs only two lines for each direction; for our purpose the communication between the DAQ and the trigger boards is mono-directional because the data flow is always from the trigger board to the DAQ board.

The principle of operation of this protocol, in the specific implementation of trigger-

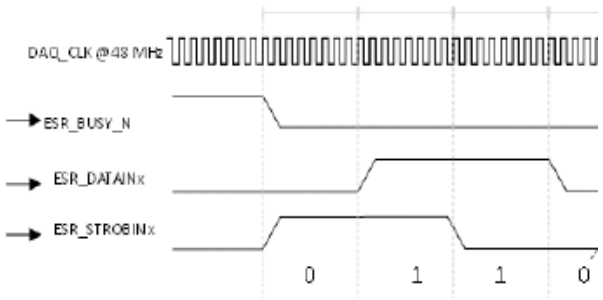

Fig. (4.7) *Principle of operation of the data/strobe protocol in the specific implementation of the trigger-DAQ boards communication. For even-numbered data bits, strobe is the opposite of data. For odd-numbered data bits, strobe is the same as data. Data are valid only when the* ESR_BUSY_N *signal is asserted (active low).*

DAQ boards communication, is illustrated in Fig. 4.7: the data values are transmitted directly, while the auxiliary strobe line changes state whenever the data signal remains constant from one data bit interval to the next. It can be noted that, performing a simple *exclusive or* (XOR) operation on data and strobe, a clock signal is generated. The advantage of this protocol, instead of having an additional clock line, is that the data/strobe is more tough when the signal has to travel on a wire and also immune to clock skew.

In addition to the data and strobe lines, a *busy* signal is implemented and the DAQ accepts the data only when this signal is asserted (active low). The clock used for the communication is 8 times the DAQ clock (48 MHz), because of the necessity to have changes on the bus with a lower frequency respect to the sampling rate. That means a 168 ns clock for the transmission and a throughput of 6 MHz.

The information transmitted with the data/strobe link when the HEPD is in a running state, is reported in Tab. 4.2 and Tab. 4.3, for acquisition and calibration runs respectively. In addition to the read-out of the PMTs, significant parameters of the currently processed event are transmitted, such as the dead time, the number of lost triggers during the dead time window, the live time and the rate meters for the nine pre-defined trigger configurations discussed in 3.6.

Considering the fixed dimension of the data transmitted via the data/stobe link, the small contribution to the HEPD dead time due to the data from the trigger board can easily be calculated and it results as follows:

$$2368\, bits \;:\; 6\, Mbps \;\simeq 400 \mu s.$$

Acquisition Run		
FIELD NAME	**NR WORD (16-bit)**	**NOTE**
PMT ADC data (low gain)	64	PMTs data, low gain channel
PMT ADC data (high gain)	64	PMTs data, high gain channel
Trigger counter	2	Nr. of trigger received
Lost Triggers	1	Nr. of trigger lost during the dead time of the previous event
PMT trigger flags	4	Bitmap of PMTs over threshold 1 means the PMT is above threshold 0 means the PMT is below threshold
Trigger mask rate meter	9	Rate meter of the nine pre-defined trigger configurations
Alive Time	2	Alive time of the previous event
Dead Time	2	Dead time of the previous event

Table (4.2) *Data transmitted from the trigger board to the DAQ board after a trigger signal is generated during an acquisition run.*

Calibration Run		
FIELD NAME	**NR WORD (16-bit)**	**NOTE**
PMT ADC data (low gain)	64	PMTs data, low gain channel
PMT ADC data (high gain)	64	PMTs data, high gain channel

Table (4.3) *Data transmitted from the trigger board to the DAQ board during a calibration run.*

4.3.3 FPGA-DSP Handshake

The handshake between the DSP and the two FPGAs of the DAQ board is at the base of the DAQ functioning.

As described in Chap. 3.4.1 and shown in Fig. 3.6, the communication between the DSP and the two FPGAs of the DAQ board is provided by the I/O memory space interface that supports 2048 locations of 16-bit data. Both FPGAs share the same physical bus; specifying a different address the DSP can select which one to access. Several registers are mapped in both FPGAs and can be accessed by read or write operations depending on the register. In Tab. 4.4, the registers shared between the Main FPGA and the DSP are reported. During its normal working, the DSP configures the DSP_STATUS register with its current status while the FPGA is continuously monitoring it. Every unexpected change will be reported to the CPU board via the slow control link and can cause the restart of the DAQ board. The 8 possible states for the DSP are described in the next paragraph.

These memory mapped registers in the Main FPGA are also used by the DSP to communicate with the DSP of the CPU board by a specific protocol called *mail box* that has been developed and is described in detail in section 4.3.4.

As can be seen in Fig. 4.8, the Main FPGA also controls the two external level sensitive interrupts for the DSP: the DPRAM interrupt is used to report that a new event during an acquisition is ready to be processed by the DSP (IRQL0), the second one is used when a new command from the CPU is received in the mail box registers and must be executed (IRQL1). A third interrupt is generated by the DSP itself at the end of each Byte DMA memory transfer, used to access the two non-volatile memories (FRAM) and the SRAM.

The external interrupts have been configured to level sensitive although they are used like an edge sensitive interrupt. The decision to use level sensitive interrupts has been taken since they are safer from noise and less susceptible to transients.

When the Main FPGA has to notify the presence of a new event to be processed (a CPU command in the mail box or a trigger), the interrupt level is set to the low value; the DSP Interrupt Service Routines (ISRs) are called and the DSP writes the SWRST register (see Tab. 4.4) to reset the interrupt level with a high value again.

It is good practice to have very few instructions inside the ISR because, while executing it, the DSP is not sensible to new interrupts. For this reason inside the two ISRs the DSP just increases a counter of received events, then in the main loop of the application it checks if the number of received events is equal to the processed events and, if not, it starts processing the next one.

In addition to the I/O space, FPGA and DSP exchange data by means of the Dual Port RAM. The characteristic of this memory is that it can read and write different memory cells simultaneously at different addresses. For the DSP point of view, the DPRAM is mapped as an external overlay page of data memory (see section 3.4.1) that can be

DAQ FPGA I/O memory map			
ID	**OFFSET**	**TYPE**	**DESCRIPTION**
REV	00	RO	Main FPGA Revision
SWRST	01	RW	FPGA-DSP Interrupt Reset
DSP_STATUS	02	RW	DSP status
SIL_DET_CONF	03-08	RO	Configuration for the silicon detector
SI_PED_CNR	09	RO	Number of event used for silicon pedestal calculation in calibration (step 1)
SI_RMSRAW_EV	10	RO	Number of event used for silicon raw RMS calculation in calibration (step 2)
SI_RMS_EV	11	RO	Number of event used for silicon RMS calculation in calibration (step 3)
SI_GCHK_EV	12	RO	Number of event used for the Gaussian check of the silicon channel in calibration (step 4)
PMT_PED_EV	13	RO	Number of event used for PMT pedestal calculation in calibration (step 1)
PMT_RMS_EV	14	RO	Number of event used for PMT raw RMS calculation in calibration (step 2)
SI_PED_CNT	15	RW	Number of event left to end silicon pedestal calculation in calibration (step 1)
SI_RMSRAW_CNT	16	RW	Number of event left to end silicon raw RMS calculation in calibration (step 2)
SI_RMS_CNT	17	RW	Number of event left to end silicon RMS calculation in calibration (step 3)
SI_GCHK_CNT	18	RW	Number of event left to end silicon Gaussian check in calibration (step 4)
PMT_PED_CNT	19	RW	Number of event left to end PMT pedestal calculation in calibration (step 1)
PMT_RMSRAW_CNT	20	RW	Number of event left to end PMT RMS calculation in calibration (step 2)
DSP2CPU_LOW	32	RW	Mail box: data from DSP to CPU (low 16 bit)
DSP2CPU_HIGH	33	RW	Mail box: data from DSP to CPU (high 16 bit)
CPU2DSP_LOW	34	RO	Mail box: data from CPU to DSP (low 16 bit)
CPU2DSP_HIGH	35	RO	Mail box: data from CPU to DSP (high 16 bit)
MBOX_STATUS	36	RO	bit 0 = 1 $\Rightarrow$ A message from CPU must be read bit 1 = 1 $\Rightarrow$ A message from DSP must be read

Table (4.4) *Main FPGA memory mapped register in the I/O space of the DSP with a description of their functionalities. RO and RW mean that the register can be accessed by the DSP in read only or read and write modality, respectively.*

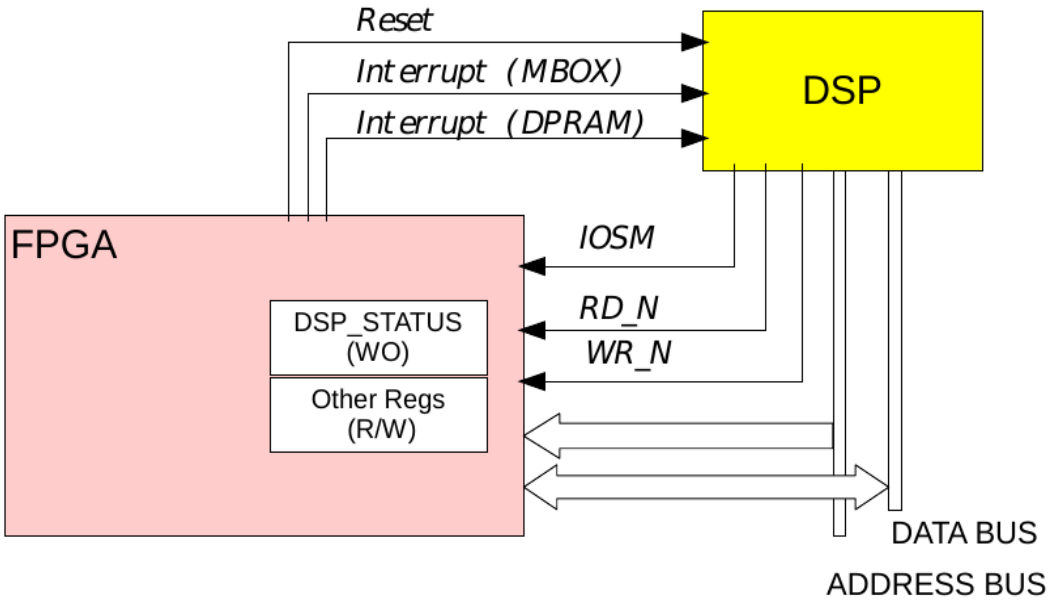

Fig. (4.8) *A scheme of the communication between the FPGA and the DSP of the DAQ board. The FPGA controls the two external interrupts and the reset line for the DSP and has a sequence of memory mapped registers the DSP can access through the I/O space interface.*

addressed up to 16 kB because of the 14-bit address bus. The total dimension of the DPRAM is 128 kB (17-bit required for the address); for this reason it has been divided into 8 "pages" for the DSP.

The FPGA sets the 3 Most Significant Bits (MSBs) of the address bus and selects which of the eight pages the DSP can access.

When a trigger signal is generated from the trigger board the FPGA starts the read-out of the silicon detector channels; at the end of this process the trigger board sends the PMT data and the other parameters discussed in 4.3.2 via the data/strobe link and, once this transmission is over, the Main FPGA writes all the scientific data on a DPRAM page.

At this moment the FPGA sets the 3 MSBs in order to allow the DSP to read the data, and at the same time is capable to write on a different page in the case a new trigger is received.

This procedure permits to have an 8-event buffer with the Main FPGA and the DSP working in parallel during the event processing although on different events. The buffer acts like a FIFO where the first event written by the FPGA will be the first event processed by the DSP.

On the other hand, once all the eight pages are full, the FPGA has to wait the end of the DSP operations before writing new data on the DPRAM.

4.3.4 CPU-DSP Handshake

The CPU-DSP and the DAQ-DSP can exchange data through a *mail box* protocol (MBOX) implemented by means of the Main FPGA of the DAQ board. The MBOX uses two 32-bit data registers and two control bits. The CPU accesses these registers via the slow control link, while the DSP uses the memory mapped space with the I/O interface reported in Tab. 4.4.

The two bits are used to notify when a message from the CPU/DAQ must be read and can be read (i.e. the mail box is not busy), while the two data registers are used to store data from the DAQ to the CPU (DAQ2CPUMBOX register), and to store data from the CPU to the DAQ (CPU2DAQMBOX register). The content of the data registers is used as follows: the most significant 16-bits are used as a command ID to specify the operation, the lower 16-bits are an optional data. The CPU is considered as the master of the protocol, because the DAQ-DSP can only send response to a previous CPU command. Before accessing the data registers the CPU has to verify that the control bits are not set to a busy status to avoid a conflict accessing the same register at the same time. Then it can write the information in the CPU2DAQMBOX registers; an interrupt is generated for the DAQ-DSP that gets the data content, processes the command and writes a response in the DAQ2CPUMBOX registers.

The MBOX protocol is used to handle two groups of commands:

- software upgrade commands;
- application commands.

The first group includes all the commands developed for a potential upgrade of the software for the data acquisition board. In fact, while an update of the CPU-DSP can be done by sending proper CAN bus tele commands, the DSP of the DAQ board can not access the data content of the tele commands by itself, and the use of the mail box protocol is necessary. By means of this set of predefined commands it is possible to rewrite a small section or the whole portion of the FRAMs where the DSP software is saved. Several commands have been implemented to set the address of the content that must be changed, to transfer the new content or to notify the end of the upgrade. In Tab. 4.5 all the commands used in the software upgrade procedure are reported with a small description.

The upper 16-bits of the data register CPU2DAQMBOX are used to specify the operation to be applied, while the lower 16-bits are used to transfer the new data content. After receiving each command the DSP answers with the 1's complements (bit inversion) of the received message in the DAQ2CPUMBOX. The CPU checks the returned value and, if it is correct, continues the sequence.

Mail Box: Software Update Commands		
Command Name	**Value (hex)**	**Note**
DWNL_SETBASE	0xFE00XXXX	sets the 16 MSBs of the address in the FRAM memory with the value expressed by the 16 LSBs of the message (XXXX)
DWNL_SETOFF	0xFE01XXXX	sets the 16 LSBs of the address in the FRAM memory with the value expressed by the 16 LSBs of the message (XXXX)
DWNL_WRITE	0xFE04XXXX	writes the XXXX content at the address previously set by DWNL_SETBASE and DWNL_SETOFF
DWNL_READ	0xFA00	reads the FRAM data at the address previously set by DWNL_SETBASE and DWNL_SETOFF
DWNL_END	0xFEFFXXXX	when the software update is completed, sets the checksum value of the program. The DSP writes it on a fixed FRAM location
DWNL_ALIGN	0xFE05	copies FRAM0 content to FRAM1. In this case FRAM0 refers to the memory used for the software boot.

Table (4.5) *List of commands used in the mail box protocol to update the program of the DSP stored in the non-volatile memories. Each message in the mail box is composed by 32-bits where the 16 MSBs are the command and the 16 LSBs are an auxiliary parameter. For the message where only 16 bits are reported, the LSBs are not used.*

Considering that the DSP program for the DAQ is about 120 kB, and with the mail box protocol every 16-bit data requires a command from the CPU, the upgrade protocol is a relatively slow procedure. In fact, to complete the upgrade of the whole DSP software, approximately two minutes are necessary. It is worth noting that a minimal version of the DSP program (called *miniboot*) is stored in the DAQ Main FPGA non-volatile memory, and is not writable by this procedure. In case of any error that can corrupt the FRAM content during the upgrade operations or because of a SEU[6], it is always possible for the DSP to boot from the FPGA and execute the software upgrade commands.

The second group of commands is used from the CPU to order some specific operation to the DSP of the DAQ board. These operations include a self-test of the memories on the boards, the start of the acquisition/calibration operations or a DAQ pre-power off. This latter command is used for example before a hardware power-off of the DAQ board because the DSP, whether it is in an acquisition state, has to properly close the current run and dump the content on its internal RAM before its power-off.

The execution of a specific mail box command depends on the current DSP status. In each state, there is a list of allowed or forbidden commands.

4.3.5 DSP: Boot and Finite State Machine

After the power on of the DAQ board the reset signal of the DSP is de-asserted and the upload of the software will start automatically from the non-volatile memory to the internal DSP RAM with the same mechanism described in 4.2.1.1. For a safer working condition, the code of the program is stored in two copies, one for every FRAM memory, with the addition of an error detecting code (see DWNL_END mail box command in 4.5). When the upload is completed a self-check is performed by the DSP to validate the software; if no errors occur and the error detecting code is verified, the DSP will update the status register of the FPGA (DSP_STATUS) notifying a correct boot; otherwise if the calculated error detecting code is different from the one saved in the FRAM, an error message is notified in the status register. In this case, or if the status register is not updated after 80 ms from the boot, the Main FPGA selects the second FRAM as a different source for the boot[7].

If the boot failed also on FRAM2, a recovery solution has been implemented; a minimal version of the DSP software, stored on the Main FPGA flash memory, is used for the boot. This minimal version, called *miniboot*, is not able to operate acquisition runs but it

[6] A Single Event Upset is a change of state in an electronic device, such as a random access memory, caused by the passage of an ionizing particle through the device.

[7] The time required for the boot has been measured and it is 40 ms; 80 ms has been considered safe enough as an upper limit for the time required during the boot

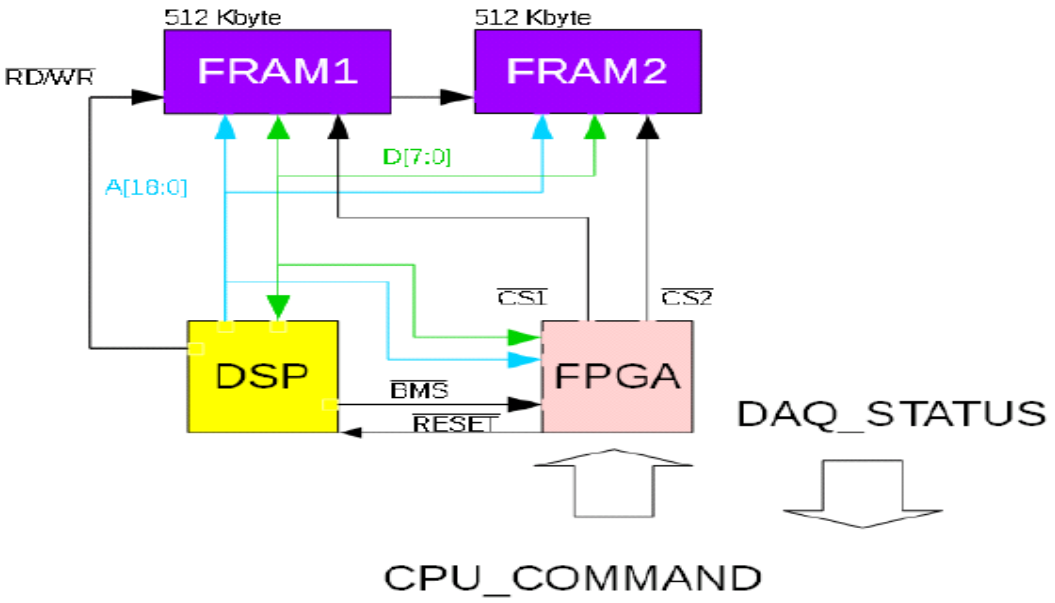

Fig. (4.9) *The DSP can boot from three different sources: FRAM1, FRAM2 or FPGA. The Main FPGA selects which source must be used and, if an error occurs or the 80 ms timeout expires, will switch to the next source. The CPU board knows which source has been used by monitoring the status register of the FPGA, and sends this information in the telemetry data.*

is used only to communicate with the CPU board with the mail box protocol and is used to overwrite both FRAMs with a correct version of the software. In Fig. 4.9 there is a scheme of the three boot sources.

After the boot is completed and the DSP program is loaded in the internal memory, the status register will reach the INIT state. In Fig. 4.10, all the 8 possible logical states for the DSP are shown. This scheme, called *finite state machine*, represents the flow of the operations that has been implemented for the DSP during the main loop after its power on.

The finite state machine follows a fixed sequence of logical states, represented by different codes in the status register. The transition from one state to another depends on both the current state and the external received interrupt. The end of an internal operation for the DSP can cause a change of state as well. The Main FPGA has the task to control the transitions and reset the DSP in case of an unexpected change of state. A timeout has been implemented for each state, with the exception of the no-operation state (IDLE) to avoid a possible situation where the DSP is stuck.

In the INIT state the DSP has reduced functionalities and it is sensitive to only mail box interrupts that means a CPU command to be processed. Depending on the received command the transition can be to the SELF_TEST state, if the CPU asked for some in-

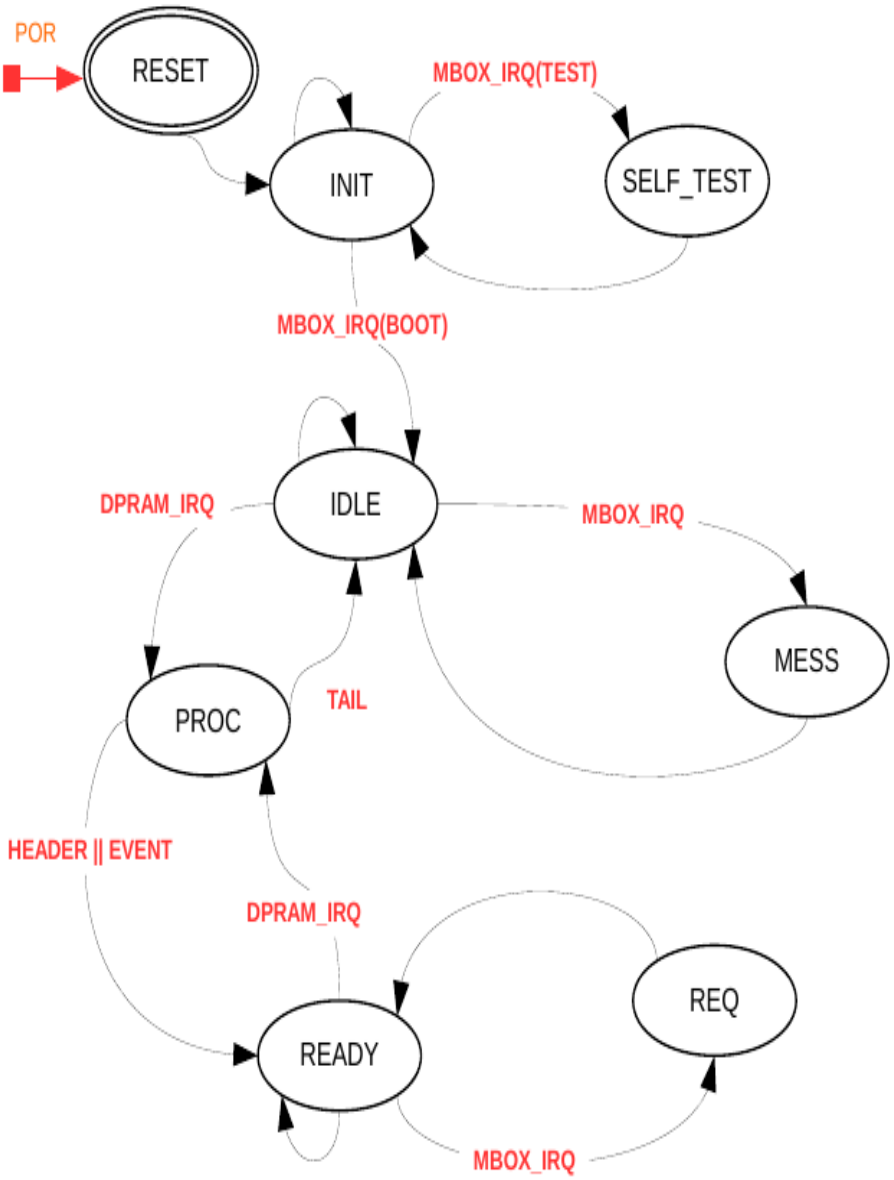

Fig. (4.10) *Finite State Machine for the DSP: 8 different states are possible. The current state can be changed after an external interrupt (like a new trigger or a command from the CPU) or after the completion of the current operation.*

tegrity check, or to the IDLE state if the CPU started the main application of the DSP.

The main task of the DSP is the compression, the formatting and the transmission of the scientific data of the HEPD apparatus. In the IDLE state the DSP is waiting for starting a new acquisition run. This happens when the Main FPGA, that was previously set in acquisition state from the CPU, writes in a free DPRAM page the header packet containing all the configurations for the next run. In section 4.3.6.4 the data content of a run packet is illustrated into details. These configurations will be used by the DSP in the event processing. For instance, this header packet specifies which part of the detector is powered on, or the threshold used to consider a 'signal' on a silicon strip.

Although all these parameters have been studied during the test phase of the apparatus in order to estimate the best value to be used (see Chap. 5), it has been decided to keep the possibility to modify them with a specific command from the ground stations if further analysis of the in-flight data will suggest a change.

When a new run is started, the DSP reaches the PROC state, a temporary state indicating the DSP is busy and processing data. At the completion of the processing operation there is a transition to the READY state, waiting for a new event to be processed in a new DPRAM page.

As seen before, the FPGA uses the DPRAM interrupt to notify there are new data to be processed in the DPRAM. The information about what kind of data they are, and consequently which operation is required on them, is contained in the data themselves. All the possible data packets that can be written in a DPRAM page are reported in Fig. 4.11. In the first memory address the Main FPGA writes the number of packets contained in the current page and in the next one the type of the packet is specified.

When the type field indicates a tail packet, the DSP will stop the current run and return in the IDLE state, waiting to execute a new start run command from the CPU.

It can be noted from Fig. 4.10 that also in the IDLE and in the READY states the DSP can receive a mail box interrupt and process a command from the CPU. On the other hand, not all the mail box commands are allowed in those states (software update commands are possible only in the INIT state).

4.3.6 DSP: Acquisition Software

In this section the operations of the DSP in the PROC state, i.e. during a run (acquisition or calibration) are described in detail.

4.3.6.1 Data Compression

As reported in Chap.1.4, the total mass memory size for the satellite is 160 Gbit; the X band is used for the data transmission with the ground stations with a downlink rate of

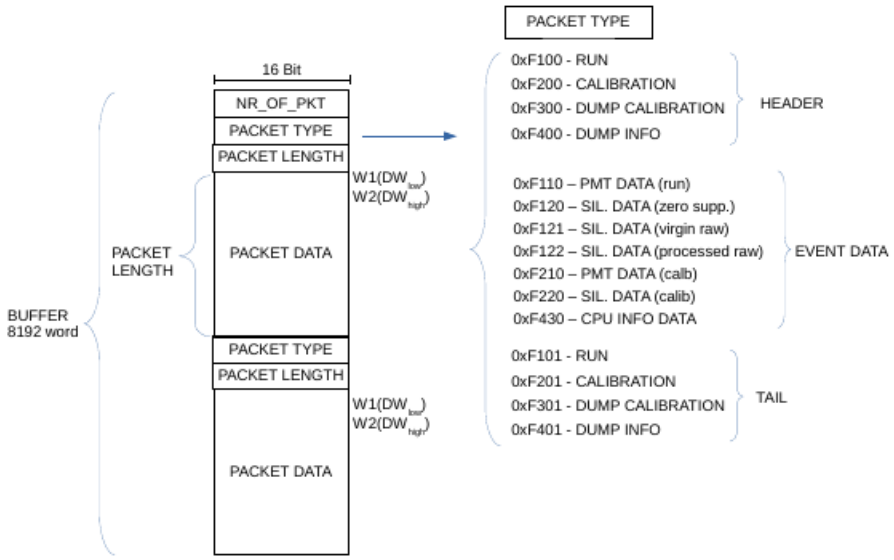

Fig. (4.11) *Structure of the data in a DPRAM page. The packet type information is used to inform the DSP which operation must be performed on the data.*

120 Mbps. At the moment, only 5 ground stations are provided and all of them are located within the Chinese territory; therefore, the downlink is possible only for a limited time window. Considering the number of ground stations and the allowed area for the downlink (see Fig. 4.12), the CSES downlink rate has been estimated around 260 Gbit/day. On board CSES, the HEPD is the detector that produces the largest amount of data, for this reason 50 Gbit/day are dedicated to the HEPD only.

An estimation of the in-flight HEPD trigger rate has been calculated by using a set of data taken from the PAMELA[46] experiment.

The PAMELA apparatus is a particle detector on-board the Resurs-DK1 satellite with an elliptic orbit ranging from 350 to 600 km. It is composed by three planes of plastic scintillators for the TOF system, a magnetic spectrometer for the tracking system and an electromagnetic calorimeter. The first plane of plastic scintillator (S1) is placed on the top of the apparatus and is composed of two layers (S11 and S12), each one with a similar thickness compared to the HEPD trigger plane (7 mm instead of 5 mm).

I have selected PAMELA orbits with an altitude in the range 490 km $<$ altitude $<$ 520 km, comparable to that of CSES satellite (500 km), then the hit rate on the 2nd layer of S1 has been taken into account and scaled to the dimension of the HEPD plane. In fact, after a correct normalization for the plane area, the number of particles passing S11 and hitting the second layer of the PAMELA TOF, can be considered as a rough estimation of the number of particles passing the HEPD trigger plane and hitting the fist plane of the HEPD calorimeter. Fig. 4.13 shows the calculated hit rate for the HEPD, by using the

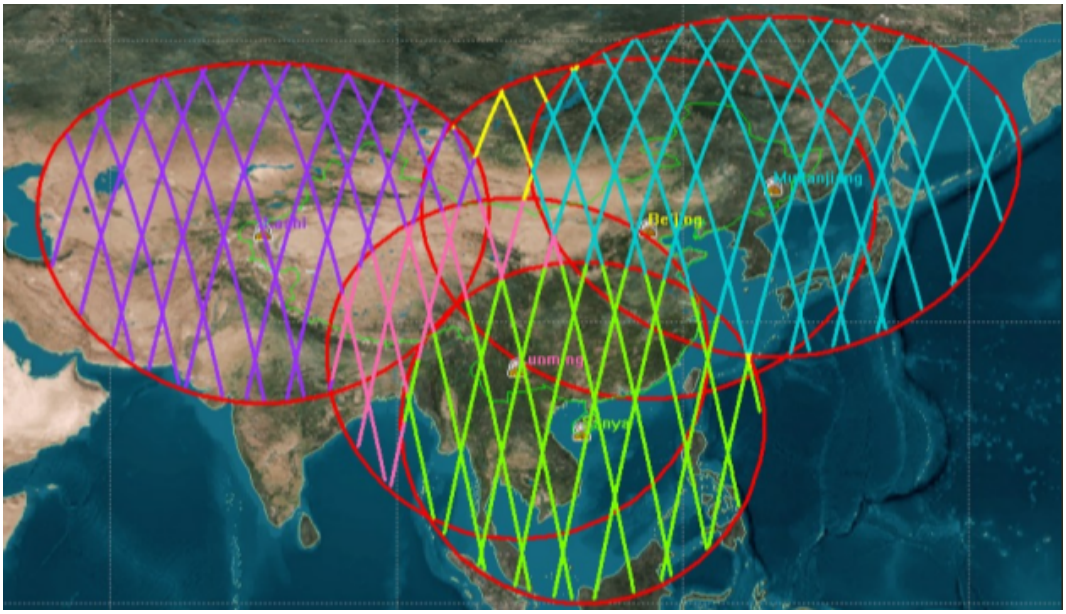

Fig. (4.12) *Allowed area for the downlink of the satellite data.*

PAMELA data. The numbers reported in the figure are the mean value of the trigger rate, calculated by taking into account all the passage of PAMELA in that specific bin.

The cuts at latitude above 60° and below −60° are due to the stand-by of the HEPD in the polar region because of the satellite attitude adjustment.

Considering a mean value of 100 triggers per second and a daily working time around 17.6 h, it is possible to estimate approximately 6 $\times 10^6$ event/day. The 4608 16-bit channels of the silicon detectors and the 128 PMT channels (high-gain and low-gain channel of every PMT), yield to a total dimension of $\simeq$ 9.5 kB for one event, that means not sustainable 50 GB/day if no compression is applied. This number is 8 times larger the daily storage dedicated to the HEPD.

For this reasons, it is necessary to perform a compression of the online data in order to avoid a saturation of the satellite memory. Due to the small size of the PMT data compared to the silicon detector data, it has been decided to not compress the information coming from the trigger board.

In conclusion, one of the main tasks of the DSP is an efficient compression of the data read-out from the silicon detector. A specific compression algorithm has been developed to eliminate the 16-bit readout channels associated with all the strips whose signals do not significantly differ from the expected value, considering the contribution of the baseline (the pedestals), the average noise for that channel, and the common noise for all the channels related to the same silicon sensor. Pedestal, noise and common noise parameters for all the channels are determined during a dedicated calibration procedure.

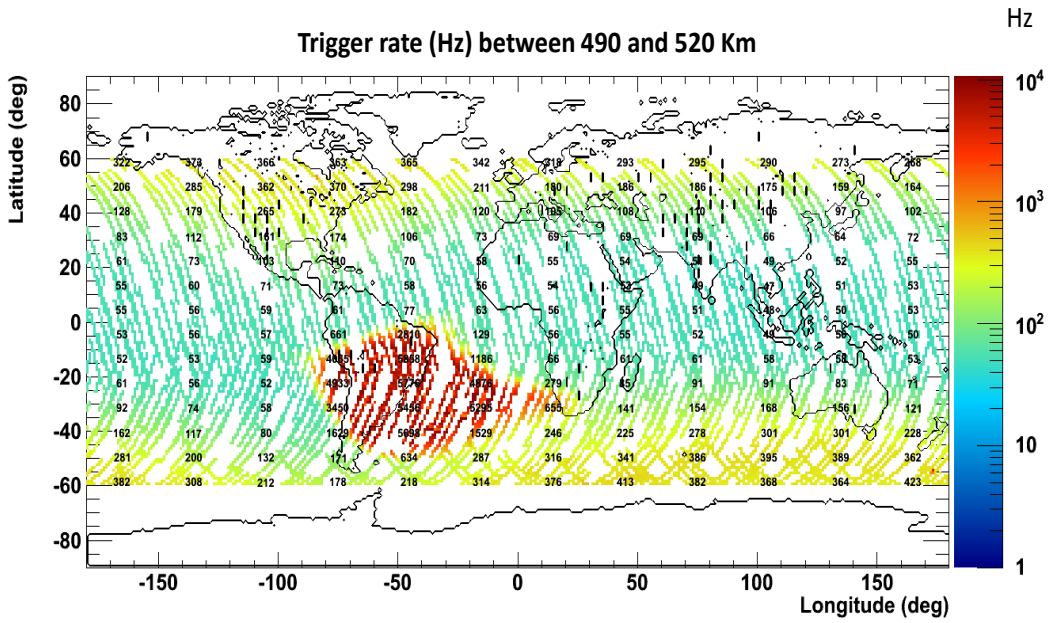

Fig. (4.13) *Estimated trigger rate for the trigger plane of the HEPD detector. The rate has been calculated starting from a sample of data acquired by the PAMELA detector and selecting orbits close to the 500 km altitude of HEPD. The cuts at latitude above 60° and below −60° are due to the standby of the HEPD in the polar region because of the satellite attitude adjustment.*

4.3.6.2 Online Calibration

A in-flight calibration procedure is required in order to perform a data compression.

Each silicon strip (and also each PMT channel) fluctuates around a mean value (pedestal) with a certain variance (RMS^2). The calculation of these two values is the aim of the online calibration. For this purpose, it is needed to acquire a fixed number of events, without the signal of a particle crossing the apparatus that will affect the pedestal measure. To accomplish this requirement a special procedure has been developed for the trigger board that, in the calibration mode, generates and sends false trigger to the DAQ with the maximum possible frequency. This means that, as soon as an event is processed and the hold signal is released by the DAQ, a new false trigger is generated. Then, the calibration algorithm can be considered as a four step procedure:

1. Pedestal calculation:
   1024 false triggers are used to evaluate the pedestal of each channel. Assuming ADC_{ij} is the signal registered on the channel *i* for the event *j*, the pedestal of channel *i* is defined as $ped_i = \frac{1}{N}\sum_{j=1}^{N} ADC_{ij}$.

   An example of the pedestals of a silicon ladder is shown in Fig.4.14 for the central ladder of the two silicon planes.

2. Raw Sigma calculation:
   1024 false triggers are used to evaluate the channel fluctuation to characterize the channel stability. The raw noise is calculated according to:

$$\sigma_i^{RAW} = \sqrt{\frac{1}{N}\sum_{j=1}^{N_j}(ped_i - ADC_{ij})^2}. \tag{4.1}$$

   The σ^{RAW} parameter is very important for the calibration purpose; it is used to calculate which channels are *dead* channels and which ones are *hot* channels, in order to exclude them in the next calibration step. A *dead* channel is a channel with $\sigma^{RAW} < 5$ ADC counts and is considered to be a not working channel. This could be, for example, a channel not connected to the read-out electronics because of a damaged bonding of the kapton wire. The value of 5 ADC counts for the threshold has been selected considering that 5 ADC counts is the common value for the $sigma$ for the DAQ only, without the silicon detectors connected to the electronics system.

   An *hot* channel is a channel with $\sigma^{RAW} > 30$ ADC counts and is considered to be related to a noisy strip.

3. In addition to the noise of every channel, a *common mode* noise is present on all channels related to the same VA chip used for the read-out. It is possible to separate the common mode fluctuation from the individual channel fluctuation, and consequently remove the former from the raw sigma. The common noise is calculated for each event *j* by the following equation:

$$CN_j = \frac{1}{N}\sum_{j=1}^{N_j}(ADC_{ij} - ped_i), \tag{4.2}$$

where N_j is the number of good channels (excluding dead or noisy channels, according to the criteria defined in the previous step). Once the common noise calculation is performed, it is possible to calculate the individual fluctuation of every channel without the contribution of the common mode noise:

$$\sigma_i^{TRUE} = \sqrt{\frac{1}{N}\sum_{j=1}^{N_j}(ADC_{ij} - ped_i - CN_j)^2} \tag{4.3}$$

The third step of the calibration procedure consists in 1024 events used to calculate the value in the equation 4.3. The common mode noise is induced by fluctuations of the silicon sensor itself. An analysis has been done by calculating the σ^{TRUE} with a common noise evaluated over a single VA chip, or over all the six chips in charge to read-out the same silicon sensor. No significant differences have been found with the two different approaches.

4. The last step of the calibration is used to identify those strips that do not have a Gaussian distribution of the signal/noise ratio in empty event. The estimator chosen to determine whether a channel is Gaussian or not, is the fraction of events giving counts outside $\pm$ 3 σ^{TRUE}. These strips, plus the dead ones, are the only strips that are not considered as a cluster seed in the compression algorithm. Noisy strips, with a Gaussian behaviour, are perfectly suitable to trigger a cluster.

Considering the 16-bit word length for the data memory of the DSP and the small values for the σ^{TRUE} (typically below 10 ADC counts), and in order to reduce the size of the calibration, the three MSBs of the sigma variable are used to flag if the current channel is dead, noisy or does not have a Gaussian behavior. Fig. 4.15 shows how the sigma information are stored in a 16-bit variable.

For what concerns the calibration of the scintillator detector data, only the first two steps of the calibration are applied. The same number of events are used for silicon and scintillator detectors.

It must be noted that, during the calibration, it is important to reduce the possibility of having real events, especially for the PMT data. In fact, a particle crossing the apparatus will affect few silicon channels (approximately 20 over 4608) but most PMT channels (especially the PMTs of the first planes of the calorimeter). For this reason, during the calibration phase two precautions have been taken:

- calibrations are possible only in the equatorial[8] region (excluding SAA[9]) where the trigger rate is lower;
- in case of real trigger, the trigger board will wait for few microseconds before generating a false trigger.

The CPU board, by reading the broadcast information sent from the satellite on the CAN bus, calculates in which orbital position the satellite stands, and starts a calibration only if the satellite is in the right zone. In this way, the calibration will be repeated periodically every orbit where the HEPD crosses the equator region, to take into account variations of the parameters with working conditions, such as temperature.

Once the online calibration is computed, pedestals and sigmas must be saved on the DSP RAM (on two dedicated overlay pages) and on both the non-volatile FRAM memories. Data in the DSP RAM are used for the event compression since accessing the internal page is faster compared to accessing an external memory provided by the Byte DMA port. The calibration data are also sent to the satellite via the RS-422 bus for the subsequent downlink.

The reason to store the calibration data in the two non-volatile memories came from the working mode of the satellite. In the polar region (latitude $> 65°$ or latitude $< -65°$), because of the platform adjustment operations, all the payloads on board the CSES satellite have to reduce the power consumption. For the HEPD, this modality of power consumption reduction called *stand-by configuration* implies a reduction from 35 W down to 8 W in the polar region. To accomplish this power consumption, most of the electronics boards, including the DAQ, must be powered off. Therefore, it is necessary to save the calibration data in the non-volatile memories. In this way, after a subsequent power on, they can be uploaded again in the DSP RAM and used for the acquisition in the compression mode, until the equatorial region is reached again and a new calibration is performed. In particular, for redundancy reason, the calibration data are stored on both FRAMs with an integrity check code (see 4.3.7). When the CPU commands the start application to the DSP, the calibration data are uploaded from the FRAM0 and the error code is checked.

[8]The equatorial region is defined as the region with a latitude value in the range $[-30°; +30°]$ while the SAA region has been approximated to a square with latitude in the range $[-50°; +0°]$ and longitude in the range $[-90°; +20°]$

[9]The South Atlantic Anomaly (SAA) is an area where the Earth Inner Van Allen radiation belt is closer to the Earth surface, leading to an increase of the energetic particle fluxes.

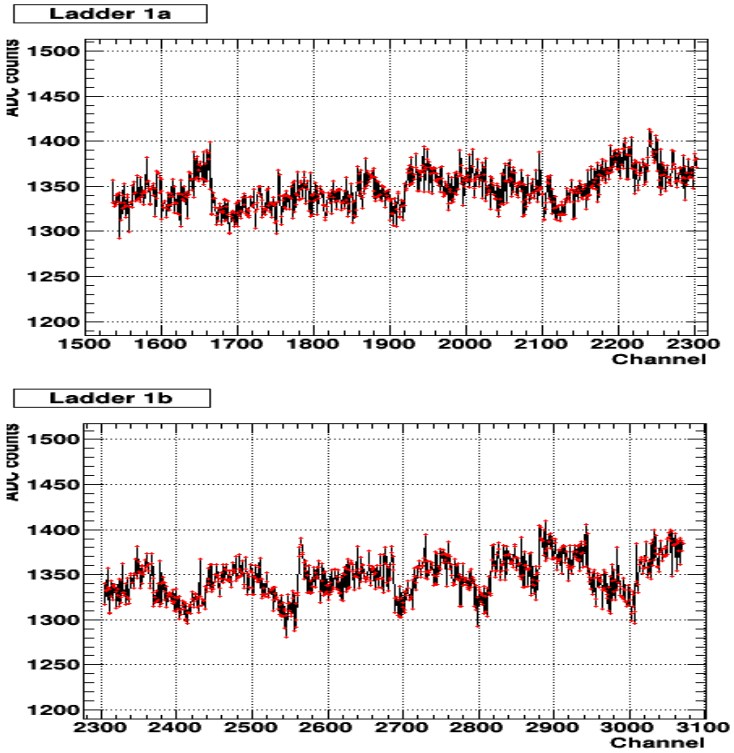

Fig. (4.14) *Pedestals calculated with the online procedure, for the central ladders of the silicon detector: external plane (top) and internal plane (bottom).*

In case the calculated code differs from the read one saved in the FRAM, the calibration data will be discarded and the data stored in FRAM1 will be uploaded. In the unlikely case of an error even on the data saved on FRAM1, an error message will be sent to the CPU by means of the mail box protocol, and only virgin raw acquisition (i.e. without compression) will be allowed until the next calibration.

NC	NG	DC	Sigma value
15	14	13	12	11	10	9	8	7	6	5	4	3	2	1	0

Fig. (4.15) *Structure of the variable containing information about the σ^{TRUE} of a single channel. The three Most Significant Bits are set to "1" to flag the current channel as Noisy, Dead or Not Gaussian. The lower bits are used for the sigma value.*

4.3.6.3 Zero Suppression

Once the calibration data are in the DSP RAM, event compression of the silicon data will be possible and only useful signal information will be transmitted. The first step to remove empty channels is to perform a pedestal and a common noise subtraction for each strip, then a cluster finding procedure will be applied. A cluster is defined as a group of adjacent strips related to the passage of a particle. For each strip *i* and event *j* the signal is:

$$S_i = ADC_{ij} - ped_i - CN_j.$$

The program will search if there is a strip passing the condition

$$S_{ij} > \sigma_i^{TRUE} \times N_\sigma,$$

where N_σ is a threshold expressed in number of RMS. The value of N_σ has been set to 3, but can be modified by specific can bus tele commands. When a strip over threshold is found, the program searches for the relative maximum in the adjacent strips. This maximum is considered as the seed of the cluster and will be transmitted with the content of *N* previous strips and *N* following strips, in addition to its index in order to reconstruct the position of the affected strip in the silicon detector. To distinguish between the peak index and the data content, the 16^th bit is set to 1 in case of the index and 0 in case of a strip signal. This can be done considering that, to address 4608 strips, only 13 bits are required.

The number *N* is another parameter that can be modified with a tele command and its value can be one, two or three. The total number of strips that compose a cluster is called the *multiplicity* of the cluster and it is: $2N + 1$. A scheme of one cluster is shown in Fig.4.16 in the case of three adjacent strips per side and a multiplicity of 7 strips.

A compression factor of 20 is achieved for the silicon data using a value of two adjacent strips per side (5 channels per cluster), that decreases to 15 in case of three adjacent strips per side.

4.3.6.4 Data Formatting and RS422 Interface

The RS422 is the interface used by the HEPD to transfer the scientific data (compressed or not) to the satellite. The characteristics of the interface have been decided by the Chinese company responsible for the CSES construction.

In Fig. 4.18 the electrical scheme of the RS422 interface is shown. The data must be transmitted in serial from the HEPD, only when the gate signal is asserted or they will be considered as invalid by the satellite. The clock frequency is 6 MHz and the distance between two gate signals (T3 in Fig.4.18) must be at least $10\mu s$. Furthermore, the packet

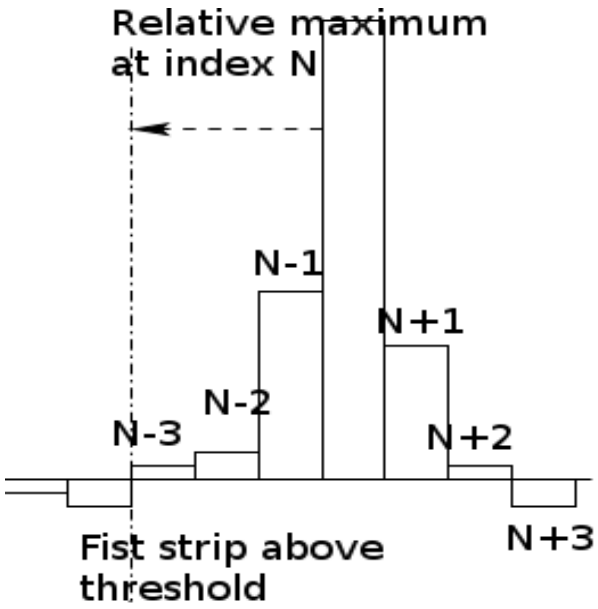

Fig. (4.16) *Scheme of a cluster with three adjacent strips per side.*

sent via RS422 must be all of the same dimension (4124 bytes) and the HEPD must send data on two RS422 channels at the same time to assure redundancy on the scientific link.

To satisfy all these strict requirements, a second FPGA that works asynchronously with the DSP is needed. All the data processed and formatted by the DSP are saved on the SRAM with a specific format depending on the data content. This SRAM is accessed by the DSP by means of the BDMA port as shown in Fig. 3.8.

The choice of the BDMA port to map the SRAM has been taken into account considering the DSP structure. In fact, the BDMA circuit of the DSP is able to access the byte memory space while the processor is performing other operations that do not require the use of the address and data buses. This yields to a parallelization of the operations that slightly reduces the dead time. When an event is processed by the DSP, the processed data are stored in two internal RAM pages and added to a queue structure used for the transmission to the SRAM memory. Each queue element contains the source address where the processed data are stored in the internal DSP RAM, the destination address in the SRAM memory, and the data length that must be transferred. Then the BDMA port is properly configured, and it works on background while the buses are not busy. When all the data of a queue element are transferred, an interrupt is automatically generated by the BDMA port and the DSP configures the port for the transmission of the next element in the queue. In Fig. 4.17 the use of the data memory pages for the DSP is summarized.

The output data are organized by the DSP in several runs. Each run has a duration of 400 s to keep into account possible variations of the configuration during the orbit (for instance the trigger configuration according to the satellite position). A run starts with a

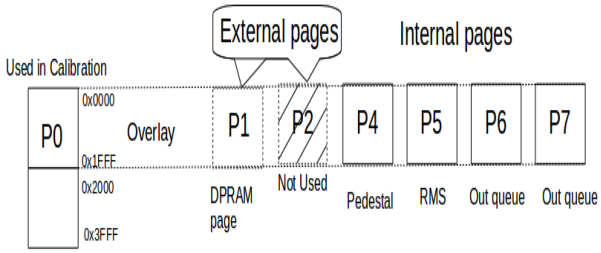

Fig. (4.17) *Scheme of the data memory usage of the DSP. Page 0 is used to store temporary data during the calibration algorithm, page 1 is the external DPRAM page, page 4 and 5 are used to store the calibration data, and pages 6 and 7 are used as a FIFO buffer before sending the processed data to the SRAM.*

header packet that contains all the information about the current run (high voltage value, trigger configuration used etc.) and the broadcast data from the satellite (GPS information, attitude parameters etc.) that are needed in the offline data analysis to reconstruct the temporal information and the satellite coordinates of each triggered event. At the end of a run other auxiliary information are sent, such as the mean value of the single PMT rate meter, and a tail packet that has the same structure as the header packet.

As soon as the DSP writes 4110 bytes on the SRAM, the download FPGA sends the frame to the satellite via the RS-422 link after adding a frame header containing an ID code and an index, and a checksum at the end of the frame. In this way, the requirement of the fixed size of the frame sent to the RS-422 is satisfied. The SRAM is used as a circular FIFO: when the end of the memory is reached, the DSP starts writing at the first address. Considering the asynchronous process, a situation where the DSP writes data on the SRAM faster than the 6 Mbps available for the download, must be taken into account to avoid a possible overwrite of the data. Two registers are memory mapped in the download FPGA the DSP accesses by the I/O port: the first one is written by the DSP to report the number of bytes copied in the SRAM, the second one is written by the download FPGA to report the number of data transferred to the satellite. Before copying data to the SRAM, the DSP has to verify that there is enough empty space to store them.

It must be noted that the SRAM is a volatile memory. Before a power-off of the DAQ board it must be emptied to not lose the data. For this reason, the pre-power off mail box command is sent by the CPU to the DSP to notify that the system is going to be powered-off. The DSP fills the SRAM with 0 to have an integer number of frames, then the memory content is dumped. This operation is repeated at every passage to the pole.

Tests have been done to verify the correct timing of the transmission by means of an oscilloscope as shown in Fig. 4.20.

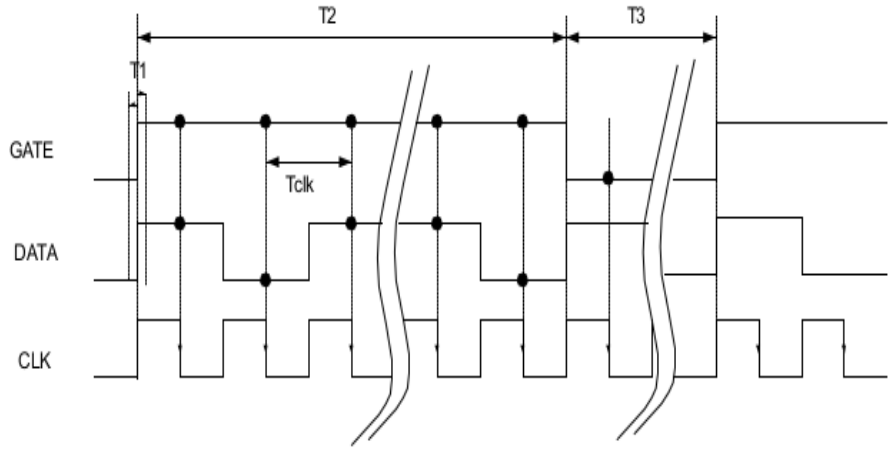

Fig. (4.18) *RS-422 protocol. Data are accepted from the satellite only when the gate signal is asserted. T2 is the gate window and must be 5.5 ms while T3 is the difference between two gate windows and must be* $> 10\mu s$.

PACKET CODE	PACKET	PACKET DATA		
0x8badcafe	RUN HEADER (Start)	Run ID and Mode		RUN
		Configuration settings		
		CPU telemetry & broadcast		
0xd3ead10c	RUN EVENT	EVENT HEADER	EVENT #1	
		TIME Info data (RUN EVENT)		
		PMT data (RUN EVENT)		
		Silicon data (RUN EVENT)		
		EVENT TAIL		
0xd3ead10c	RUN EVENT	EVENT HEADER	EVENT #2	
		TIME Info data (RUN EVENT)		
		PMT data (RUN EVENT)		
		Silicon data (RUN EVENT)		
		EVENT TAIL		
..... RUN EVENT....			... EVENTS...	
0xd3ead10c	RUN EVENT	EVENT HEADER	EVENT #N	
		TIME Info data (RUN EVENT)		
		PMT data (RUN EVENT)		
		Silicon data (RUN EVENT)		
		EVENT TAIL		
0xc01055e0	RUN SCIENTIFIC DATA	Single PMT Rate meters		
		Temperatures @ start/stop run		
		CPU time @ start/stop run		
0xcadec5c5	RUN TAIL (Stop)	Run ID and Mode		

Fig. (4.19) *Data content of an HEPD run. Each run starts with a header packet, containing all the configurations of the current run, a set of events and a tail packet.*

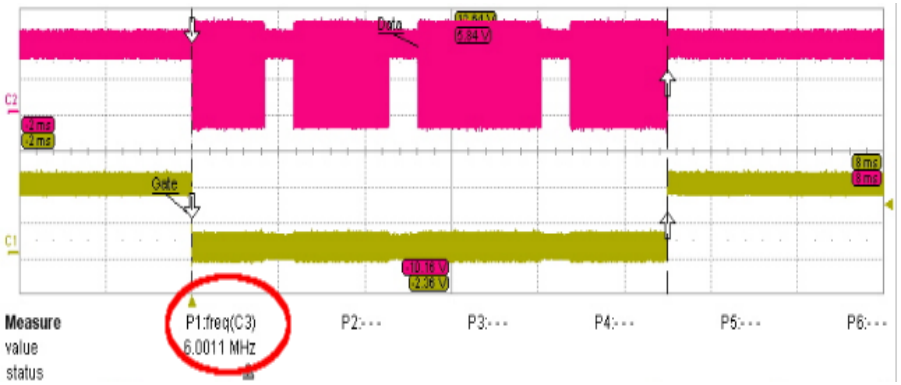

Fig. (4.20) *A picture from the oscilloscope during the verification of the timing requirement on the RS422 interface.*

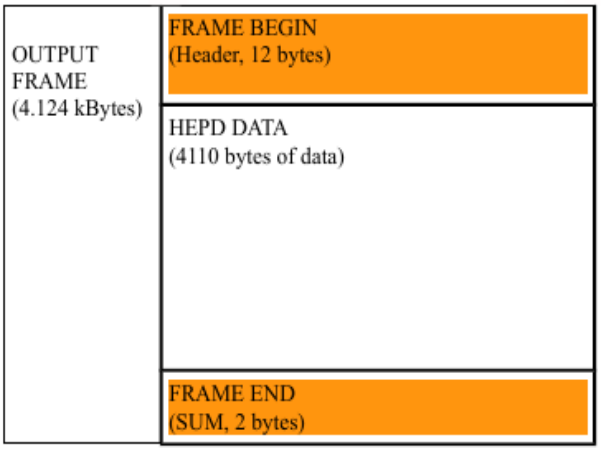

Fig. (4.21) *Structure of a HEPD frame transferred to the satellite. Each frame is 4124 bytes long and contains a header with an identifier code and a frame counter, and a tail with a checksum code to validate the goodness of the FRAME.*

4.3.7 Data Integrity Check

Several different scientific payloads are installed on board the CSES satellite. All the data from these payloads are stored in the same memory on board the satellite. Due to the necessity of reconstructing the HEPD runs once the data have been downloaded to the ground stations, it is required to add identifier codes and check codes in the scientific data. Furthermore, the downlink of a certain amount of data from the CSES satellite to the ground stations can be performed only once and no re-transmission is possible. For this reason, it is particularly important to check the data integrity with some specific code associated to the data.

In the HEPD scientific data this can be done with two different methods depending on the data length. As mentioned before, there are two different run modalities: calibration and acquisition. Whereas the calibration event size is fixed (9472 bytes considering PMTs and silicon data), during a normal acquisition the size of one event is around 500 bytes (as estimated in sec. 4.3.6.3).

Due to the small dimension of the compressed event compared to the calibration event and the necessity to keep the dead time during the event processing as low as possible, a simple algebraic sum of the event data (checksum) is used as integrity code. In the offline analysis this checksum is used in order to decide if the current event must be discarded or not. The same algebraic checksum is used by the CPU to verify the correctness of the CAN bus frames, in order to decide if the received message from the satellite can be accepted.

On the contrary, for the calibration data, a more complex *cyclic redundancy check* (CRC-16) algorithm [47] has been implemented due to the larger size of the event and the fact that the calibration is calculated only once per orbit. The same CRC algorithm is used to validate the program for the two DSPs of the DAQ and CPU boards.

Another checksum is added in the RS-422 frame by the download FPGA, as shown in Fig. 4.21, to validate the transmission from the HEPD and the satellite.

4.3.8 Dead time of the HEPD apparatus

As seen in the previous paragraphs, there are many factors, involving the trigger and DAQ boards, that contribute to the overall dead time of the HEPD apparatus. The silicon detector contributes to most of the dead time, because of the large amount of data that has to be read-out and compressed. The scheme illustrated in Fig. 4.6 shows the total dead time during the processing phase of one event, that corresponds to the time window when the HOLD signal from the DAQ is asserted. This time period includes different operations:

- read-out of the silicon data by the FPGA and write operation of those data in the

dual port memory;

- data transfer of PMT data to the DAQ;
- DSP operations: read-out of PMT+silicon data from dual port ram, data compression, formatting and transmission of the final packet to the SRAM.

In order to reduce the dead time, in the first implementation of the acquisition chain, the first two steps operated in parallel. As a result of an analysis I have performed on the first data acquired during the integration test, it has been observed that the transmission of data from the trigger board via the data/strobe link induced a noise on the first acquired silicon channels. In fact, the first silicon ladder showed a significant worsening of the RMS values, also in the case of absence of the signal. For this reason, it has been decided to serialize the two operation despite of a slight increase of the dead time. Therefore, in the current implementation, the trigger board starts sending data as soon as all the data from the silicon detector have been acquired. As calculated in section 4.3.2, the time required for the transfer of the PMT data is $\simeq 400\ \mu$s. The contribution of the FPGA to the dead time is also fixed because of the fixed number of silicon channels. A simulation of signal exchange between the trigger and the DAQ boards, excluding the DSP operations, has been done with the ModelSim software [48]. The results are reported in Fig. 4.22a. The space between the two yellow cursors is the time necessary to copy all the detector data in the dual port ram, ready to be read-out and processed by the DSP. It can be noted that the most expensive contribution is the silicon data acquisition. This simulated time has been found to be 2.605 ms.

In addition to this simulation, the FPGA dead time has been calculated during the acquisition of cosmic muons. This can be done because of the buffer structure in the DPRAM (illustrated in section 4.3.3) that can contain up to eight events. In fact, when the FPGA copied the data to the DPRAM, it is capable to process a new trigger in parallel with the DSP processing the previous event. Only in case all the eight DPRAM pages are full, the DSP dead time contributes to the total dead time. In case of a low particle rate (as it is for cosmic muons), in particular when the temporal distance between two events is lower than the dead time of the apparatus, the resulting dead time will contain only the FPGA contribution.

An acquisition with cosmic muons, has been launched with the trigger configuration T $\&$ P1, i. e. a signal on the trigger plane and on the first calorimeter plane is required to generate the trigger pulse. The muon flux at sea level is about 1 particle cm^{-2} min^{-1} for horizontal detectors [49] and a rough estimation of the HEPD event rate can be obtained if only considering the dimensions of the smaller plane P1 = 15 $\times$ 15 cm^2. This yields to 3.75 events s^{-1} or about 1 event every 260 ms that is huge compared to the apparatus dead time.

Fig. 4.22b clearly shows this behavior. The measured dead time between two events is a delta function; it is fixed by the number of silicon channels and the clock used by the involved electronics for the data transmission. It can also be seen that the value of 2.52 ms is in a good agreement with the value of 2.6 ms as obtained from the FPGA simulation.

Calculating the DSP contribution to the overall dead time is a little bit more complicated. This is because the time required for the compression is not fixed, but depends on the number of clusters found in each event. Therefore, the compression time and the size of the data to transmit will slightly change from one event to another. An event due to a particle crossing the silicon planes will produce at least four clusters (one for each view and for each plane) and the number of channels above a three sigma threshold is about seven if the assumption of a Gaussian behavior is valid for all the silicon channels and if considering the total number of 4608 channels.

To estimate the DSP dead time a procedure similar to a calibration run has been used. The HEPD has been set in acquisition mode with the trigger board generating ”fake” trigger pulses at the maximum possible rate. By means of a dedicate FPGA register, the times required for the transitions of the DSP status register from the READY state to PROC and to READY again, have been measured. The maximum value for the DSP dead time obtained with such procedure is 6 ms, for a maximum overall dead time of the apparatus equals to 8.5 ms.

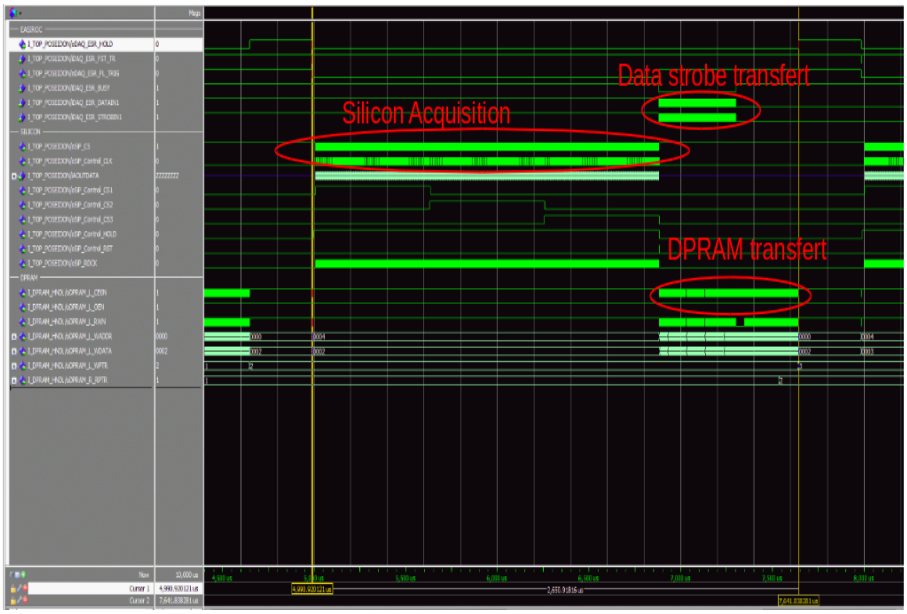

(a) *Simulation of FPGA dead time. The total value is the sum of three contributions: silicon data acquisition, data transfer of PMT data and transmission to DPRAM.*

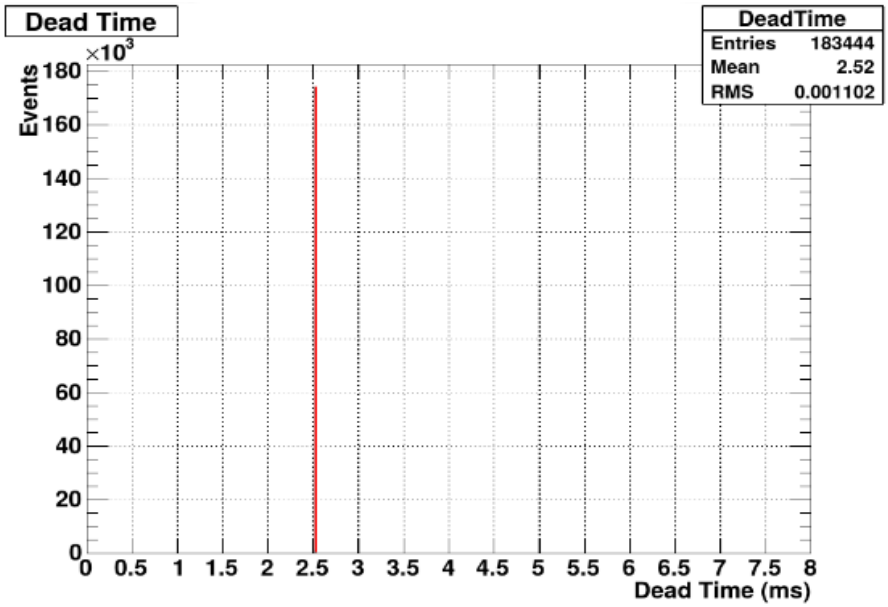

(b) *Measured dead time with cosmic muons.*

Fig. (4.22) *Dead time of the HEPD apparatus, excluding the DSP contribution.*

Chapter 5

Acceptance Tests and Preliminary Data Analysis

During my Ph.D. work, in the framework of the Limadou collaboration, I participated to the realization of three different models for the HEPD detector: Electrical Model (EM), Qualification Model (QM) and Flight Model (FM). The main purpose of the EM was to verify the compatibility between the satellite and the payload and to validate the payload functional performance. For this reason, it was tested only with our Electrical Ground Support Equipment (EGSE) and on board the satellite.

On the other hand, the QM and the FM are almost equivalent, and the purpose of the Qualification Model is actually to demonstrate that the detector is fully compliance with the specifications. For this reason, an intense space qualification campaign on both the Qualification Model and Flight Model was performed at the SERMS Laboratory in Terni (Italy) for the qualification and acceptance tests. Then the physical performances were studied with an electron beam test at the DAFNE Facility in Frascati (Italy). The FM was also tested with protons, at the Proton Therapy Center in Trento (Italy).

This test phase lasted several months, from May 2016 to November 2016. During this period we were involved in testing the Qualification Model while working at the Flight Model assembly in parallel. I took part to the whole space qualification campaign and the beam tests, during which I was the responsible of the software procedures.

The present chapter contains the description of these tests and an overview of the program I developed for a quick data analysis, in order to check the status of the apparatus during and after the tests. The last sections are dedicated to a preliminary data analysis based on data collected with cosmic rays and protons.

5.1 Space Environment Tests

Space-borne apparatus must have a high level of performance and stability during all the duration of the mission in a space environment. The extreme variation of temperature that may occurs, requires an apparatus with excellent stability over a broad range of temperatures. Furthermore, other effects such as the radiation the electrical system undergoes or the shocks and vibrations during the launch phase must be considered. For these reasons, all the components of the apparatus (electronics boards and mechanical components) must be tested in order to assure persistence to space environment.

For the HEPD detector we performed thermal and vibrational tests with both Qualification and Fligh Models. We used to call qualification tests those performed on the Qualification Model and acceptance tests, those performed on the Flight Model.

5.1.1 Setup Configuration

The setup configuration during the qualification and acceptance tests, foresaw the use of the Electrical Ground Support Equipment (EGSE) to provide the voltage to the HEPD, a storage for the scientific data acquired during the tests, and the CAN interface for sending tele commands to the HEPD, in order to change status and configurations according to the test requirements.

The EGSE is composed by different devices such as:

- a power supply module;
- the EGSE central module;
- the PC-HOST module;
- a LCD console.

The EGSE central module is based on a Zynq Evaluation Board (ZC702) by Xilinx and a daughter board, directly plugged on the Zynq, that provides two tranceivers for the RS-422 scientific data channel and two CAN bus transceivers. The Zynq board integrates a dual core ARM based processor, with a set of development tools that allows to build, develop and test embedded Linux system. By means of an ethernet interface, the EGSE central module communicates with the PC-HOST, that is used for a graphical interface and as a storage for the scientific data.

In order to make the test operations user-friendly, I developed an application with a simple graphic interface for the EGSE, to send specific CAN bus tele commands to the HEPD: by typing the specific letter on the PC-HOST keyboard, a specific packet is sent. The graphic interface of the application is shown in Fig. 5.1.

As described in section 4.2.1.3, the CPU can not send CAN bus packets without a previous request from the satellite/EGSE. For this reason, to check the HEPD status during these tests, a specific 'debug' operation mode was developed for the CPU software. In this debug mode, the CPU can always send information to the EGSE via CAN bus packets, containing for example the values of the status registers of each electronics board. By means of this EGSE application it is also possible to load a pre-defined file containing a list of tele commands, to schedule consecutive operations and automate specific procedures.

5.1.2 Thermal-Vacuum and Thermal Balance Tests

Qualification and Flight Models of the HEPD were tested in thermal and thermal-vacuum chambers with slightly different conditions, for the qualification and acceptance tests. These tests took place at the SERMS laboratory in Terni (Italy).

To perform the thermal tests of the HEPD, the top panel of the box that surrounds the detector was removed in order to place eight temperature sensors in different relevant points, such as the power supply, the CPU board, the silicon ladder etc. An additionl sensor was placed externally to the HEPD in order to monitor the chamber temperature.

The temperature cycle started with the chamber at ambient temperature, then hot and cold phases lasting several hours alternated with each other with temperature gradients of $2°$C/min and $1°$C/min for the heating and the cooling, respectively. Each cycle is composed by different steps that correspond to different operations for the HEPD, such as data acquisition, calibration, stand-by, or power off, in order to simulate the in-flight procedures. The thermal profile of each cycle inside the thermal and thermal-vacuum chambers is illustrated in Fig. 5.2. During these operations the telemetry packets sent by the HEPD were monitored to check the presence of anomalies in the detector as well as in the scientific data.

In Tab. 5.1 and 5.2, the test conditions for the Flight Model during the thermal cycling and thermal-vacuum tests are reported. For the QM, stronger conditions (such as $+55°$C for the hot temperature and $-30°$ C for the cold temperature) and more cycles were required. Two pictures of the Flight Model inside the thermal and thermal-vacuum chambers are shown in Fig. 5.3.

A graph summarizing the temporal evolution of all the temperature sensors placed on the HEPD-FM during the thermal-vacuum test is reported in 5.4. All the tests were considered successful since the test conditions were applied and no structural or functional damage was found.

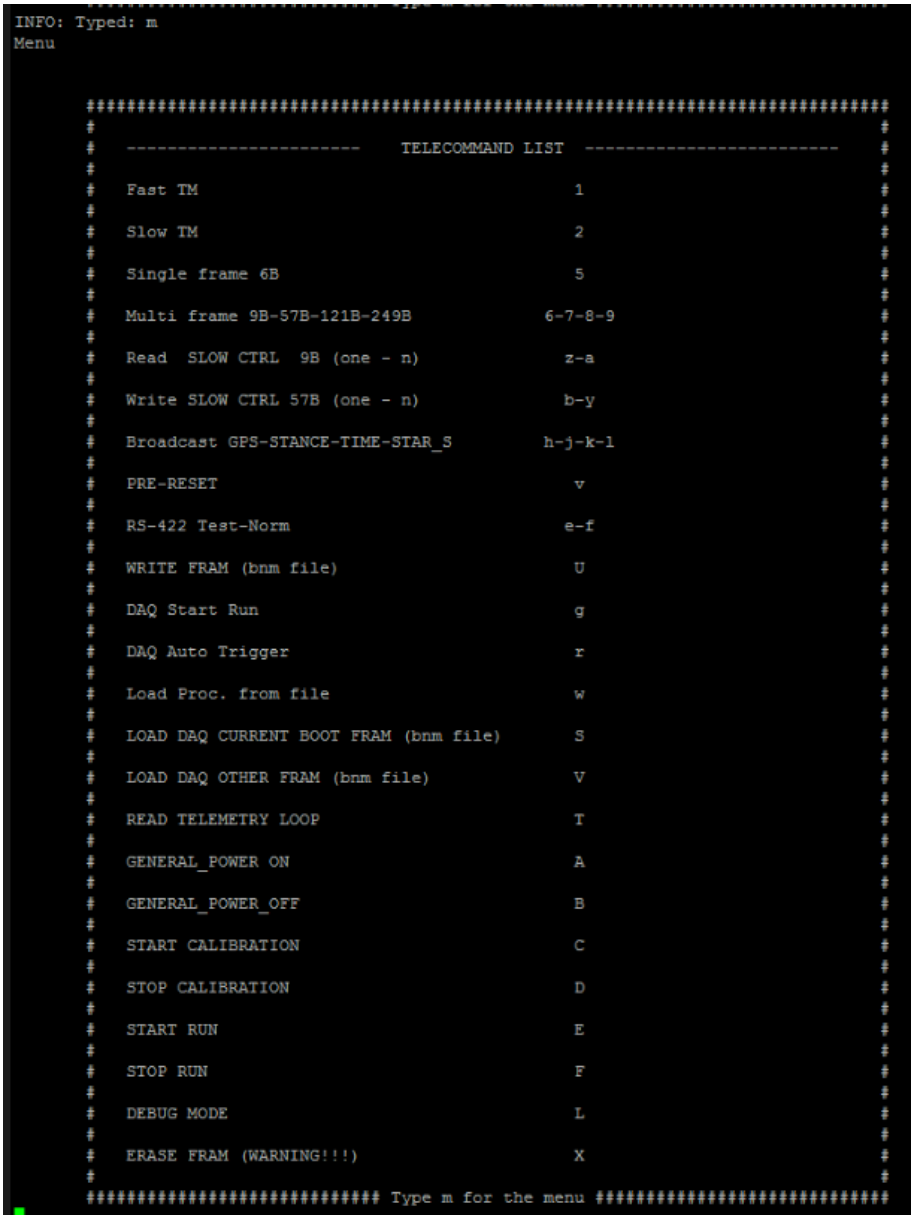

Fig. (5.1) *Picture of the simple graphic interface of the 'dummyEGSE' application, used to test the entire functionalities of the HEPD detector during the thermal and thermal-vacuum tests. By typing the correspondent letter on the keyboard, a specific CAN bus command is sent.*

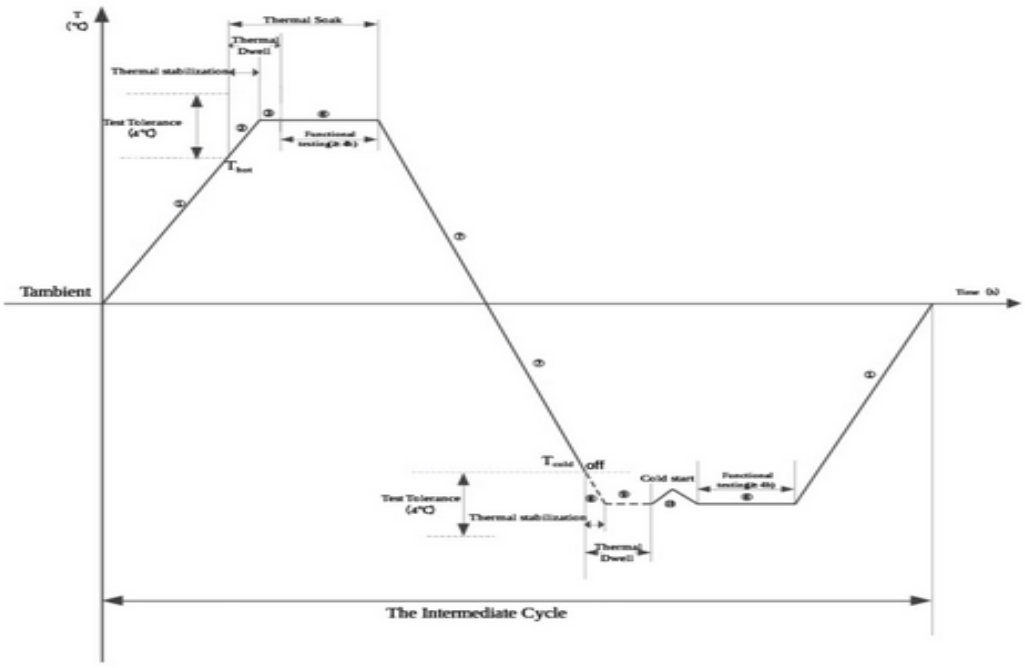

Fig. (5.2) *Profile of the thermal cycle during the test.*

PARAMETER	TEST CONDITION
Pressure	ambient
Hot Temperature	$+45°$ C
Cold Temperature	$-20°$ C
Number of cycles	17.5
Time at T_{hot} and T_{cold}	$\geq$ 4 hr

Table (5.1) *Thermal Cycling test conditions for the FM*

PARAMETER	TEST CONDITION
Pressure	$< 6.6 \times 10^{-3}$ Pa
Hot Temperature	$+45°$C
Cold Temperature	$-20°$C
Number of cycles	4.5
Temperature rate of change	$> 1°$C/min

Table (5.2) *Thermal-Vacuum test conditions for the FM*

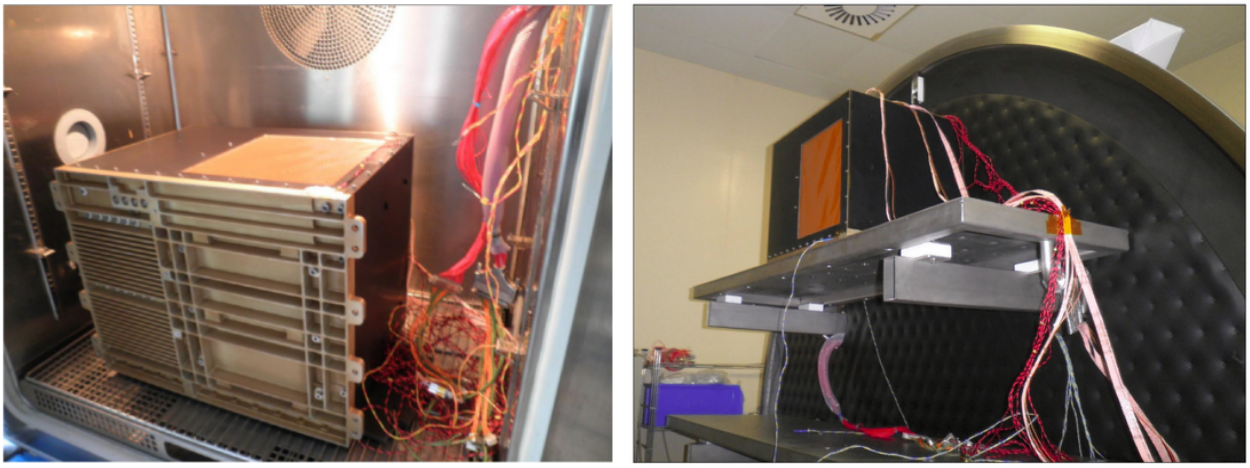

(a) *Thermal chamber at the SERMS Laboratory in Terni (Italy).*

(b) *Thermal-vacuum chamber at the SERMS Laboratory in Terni (Italy).*

Fig. (5.3) *Pictures of the HEPD-FM during the thermal cycling and thermal-vacuum test.*

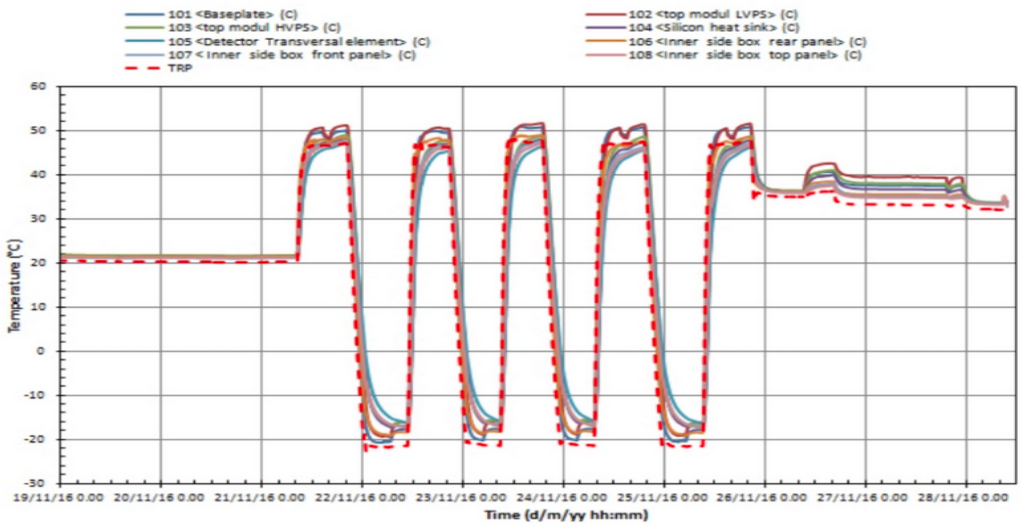

Fig. (5.4) *The chamber and HEPD-FM temperature profiles during the thermal-vacuum test. Each colour represents a different temperature sensor; the dashed red line is the one placed externally to the detector.*

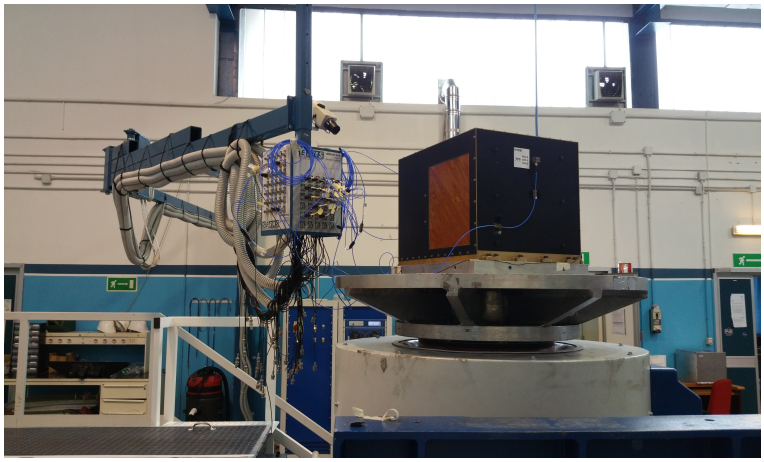

Fig. (5.5) *A picture of the HEPD-FM on the shaker system at the SERMS facility in Terni (Italy).*

5.1.3 Mechanical Tests

Space-borne apparatus encounter mechanical shocks and vibrations from a variety of sources (shipping, satellite launch). Components must be designed and tested accordingly to ensure reliability.

The mechanical space qualification test for the HEPD was performed at the SERMS Laboratory in Terni (Italy). At first, a mock-up of the entire apparatus was produced, reproducing the geometrical characteristics of the HEPD such as dimension and total mass. The detector component, like the plastic scintillator planes or the LYSO crystals, were simulated with dummy aluminum blocks. This mock-up was initially exposed to vibrational spectra verifying that the structural integrity was maintained, then the HEPD-QM was exposed along the three directions to pyroshock with a shock frequency ranging from 600 to 4000 Hz and an acceleration up to 1000 g. Vibration tests were also performed along the three axis in order to search a possible dangerous resonance, in the frequency range from 20 to 100 Hz and corresponding to a 12 g acceleration. A similar vibrational test followed on the HEPD-FM (3 axis, 20-100 Hz, 8 g) as illustrated in Fig. 5.5.

After and before each vibration test, an acquisition run with cosmic muons was performed, in order to test the detector response. No evident structural or functional damage was found.

After passing acceptance tests for space operations, the HEPD-FM was finally shipped to the DFH Satellite Company, Ltd. in Beijing (China), where vibrational and thermal tests were successfully repeated on board the CSES satellite.

5.1.4 The Quicklook Software

To check the detector during the thermal tests and to verify the test success criteria were satisfied, I also developed a *quicklook* software, for a very preliminary analysis on the raw data. This software contains a very preliminary analysis of the HEPD raw data for a quick interpretation of the scientific data transmitted via RS-422. Its aim was to check detector functioning and status during and after the acceptance tests.

The quicklook output consists in three *pdf* files with plots for the silicon tracker, the trigger detector and the range calorimeter and several *xml* files for the housekeeping component, i.e. all the data related to the configuration and functioning of the detector. The tracker plots, one for each silicon ladder, show the sigma evaluated for each channel and the common noise evaluated for each VA chip. The range of expected values for these known quantities, and a relevant difference from them can be easily noted. A map of *hot*, *dead* and *non-gaussian* channels (according to the definition given in section 4.3.6.2) is also reported.

The scintillator part, developed to monitor the PMT response, contains the ADC count distribution for each channel (high gain and low gain) and correlation plots between ADC count signals collected by the two PMTs of the same paddle/plane. An example of these plots can be seen in 5.6.

The trigger output of the quicklook software was developed to keep under control the HEPD trigger configurations. This part will be more useful with data collected in flight, since it produces plots such as the number of lost triggers, alive and dead time, single PMT rate meter or trigger configuration rate meter as a function of the UTC time. The idea is to produce fast plots in order to have the possibility to choose the best trigger configuration, once the satellite will be fully operating in orbit.

The output of the housekeeping component is reported in several xml tables containing:

- **Run information** i.e. duration, algorithm used for the silicon detector, satellite position at the start run;
- **Silicon Configuration**;
- **Scintillator Configuration**;
- **High Voltage Configuration** i.e. the set voltages for PMTs and silicon detectors;
- **Monitored High Voltage** i.e. the real high voltage values read from the HV board;
- **Time Information** i.e. satellite and HEPD-CPU time at run start/stop used to reconstruct the UTC time;

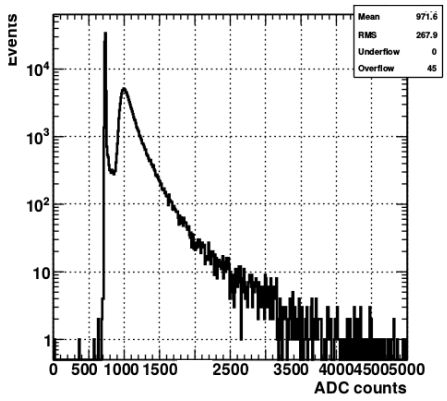

(a) *The signal distribution for a PMT on the P3 plane during the electrons test beam. It is possible to see the pedestal peak and the peak due to the particle passage.*

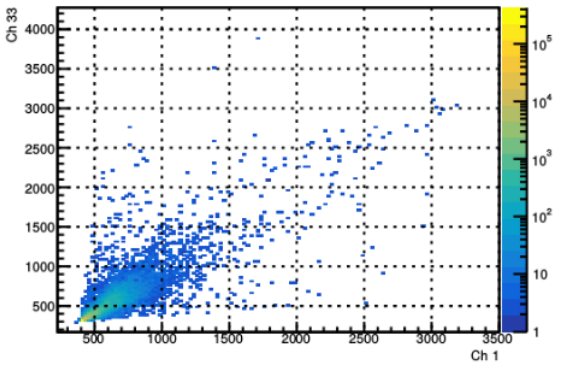

(b) *Correlation plot between ADC count signals collected by two PMTs of the same trigger paddle T2, during cosmic muons acquisition with the HEPD in the thermal chamber.*

Fig. (5.6) *Example of plot produced by the quicklook software for the scintillator detector. This program is run on the raw data as a first glance of the detector response.*

- **Position Information** i.e. satellite position and velocity at run start/stop;
- **Telemetry Information** i.e. status register of each board at run start/stop;
- **Temperature Information** i.e. the temperature measured at start/stop for the two sensors placed on the CPU and the trigger board.

In these tables, in case a cell contains a value that differs from the expected one, a coloured alert (yellow or red depending on the discrepancy) was implemented (see Fig. 5.7). In this way, any unexpected value can be easily noted.

5.2 Physics Performance

After the final assembly of the Qualification and Flight Models, we started to collect data with cosmic rays and with electrons and protons at the beam tests.

In the following analysis only data from the FM were considered. I reported here two different preliminary methods I developed to perform a position correction on the raw ADC counts measured on the silicon detector, and a PMT equalization for the PMT data. Some results of this analysis have been used for the determination and optimization of the parameters used in the data handling online software.

Run ID		DAQ Board		PMT/Trigger Board		TM/TC Power Board		HVPS Control Board		CPU Board Boot Status		CPU Board Status FSM	
Boot nr.	Run nr.	Start	Stop	Start	Stop	Start	Stop	Start	Stop	Start	Stop	Start	Stop
Default Status Values (Approximate Values)		0X50A1	0X80A3/70A2/60A2	0X0D00/0D05	0Xxx1F/xx2F	0XFFD/75C	0XFFD/75C	0x000/004	0x000/004	0x704/705	0x704/705	0X300/100/200	0X001/301 /302/002
18	1	0X50A1	0X70A2	0XD00	0X2C2F	0X75C	0X75C	0X4	0	0X705	0X705	0X300	0X1
19	1	0X50A1	0X70A2	0XD00	0X252F	0X75C	0X75C	0X4	0	0X705	0X705	0X300	0X1
20	1	0X50A1	0X70A2	0XD00	0XD2F	0X75C	0X75C	0X4	0	0X705	0X705	0X300	0X1
21	1	0X50A1	0X70A2	0XD00	0XD2F	0X75C	0X75C	0X4	0	0X705	0X705	0X300	0X1
21	2	0X50A1	0X80A3	0XD05	0XF1F	0XFFD	0XFFD	0	0	0X704	0X704	0X300	0X1
21	3	0X1000	0X80A3	0XF00	0XF1F	0XFFD	0XFFD	0	0	0X704	0X704	0X300	0X1

Fig. (5.7) *An example of the Telemetry Information XML table produced by the quick-look software. The table summarizes the status registers of the HEPD electronics boards with their expectation values; in case some value differs from its default value, a yellow alert is drawn in the corresponding cell.*

5.2.1 Proton beam test

Unfortunately, when the HEPD was tested at the DAFNE beam test facility, the silicon detector system was not assembled yet. On the other hand, the whole apparatus was tested with several proton energies in the range between 36 MeV and 228 MeV at the Proton Therapy Center (APSS) in Trento (Italy).

During the beam test, the HEPD was placed in front of the beam on a movable platform in order to change the incident beam position to hit all the trigger paddles composing the trigger plane, and all the silicon ladders. All the data were acquired with the virgin raw run mode mentioned in section 4.3.1 and 4.3.6.2. This allowed a more detailed data analysis for the detector characterization, without the risk of information loss because of the data compression. The standard data acquisition procedure consists in performing a calibration run before each beam energy, and then in acquiring the data, reading out all the 4608 silicon channels. The offline data analysis starts by subtracting the pedestal for each channel and computing and subtracting the common mode noise for each VA, calculated as described in section 4.3.6.2. After this, a cluster finding procedure is performed. The used algorithms are the same as implemented on the DAQ online software; as a consequence, it was possible to evaluate the performance and reliability of the online data compression by applying it offline.

The setup configuration was similar to the qualification/acceptance tests, with the HEPD connected to the EGSE that provided the power and sufficient data storage for all the acquired data. A picture of the setup during the proton beam test can be seen in Fig. 5.8.

Fig. (5.8) *Picture of the HEPD-FM during the proton beam test.*

5.2.1.1 Eta Correction

The first study I did on the data collected during the proton beam test was on the cluster multiplicity, i.e. the number of strips involved in the cluster signal due to the particle passage in the silicon plane. For proton runs, because of the high energy deposited due to the incident particle energy far below the MIP region, a $5\sigma_i$ threshold can been used for each channel to identify the cluster seed. The adjacent strips have been considered part of the cluster if they have a signal $S_i > 3\sigma_i$. According to this selection, the cluster multiplicity was studied at different beam energies. Fig. 5.9 shows that the number of strips with a signal above the threshold, is always one or two for all the beam energies. For the lower energies, it can be seen that there is a probability of $\sim 50\%$ to have clusters composed by one or two strips. On the contrary, at higher energies, most of the clusters seem to be composed by only 1 strip.

The reason of this behaviour can be found if considering the silicon detector structure discussed in 2.1: not all the strips are directly connected to the read-out electronics, but there is an alternation of read-out and floating strips. At lower energies for the incident beam, the energy deposited in the detector is higher according to the Bethe and Bloch curve, and the signal on the strips adjacent to the seed is above the 3σ threshold even if the particle crosses a floating strip. Since read-out and floating strips are present in the same number, a 50% frequency for a multiplicity equals to 1 is expected when the particle tracjectory is close to a read-out strip and all its charge is collected by the read-out strip. On the other hand, a 50% frequency for a multiplicity equals to 2 is also expected when the particle tracjectory is close to a floating strip and its charge is collected by the two adjacent read-out strips by means of capacitive coupling effects. In an ideal situation, the charge collected on the neightbouring read-out strips via the interstrip capacitance C_s is $Q/2$, where Q is the charge released on the floating strip. However, in a more realistic

situation, the probability of a charge loss increases if the particle hits the floating strip and must be considered.

There are several reasons for the floating strip presence in a silicon detector. At first, for an experiment on board a satellite where power consumption and volume occupation are a concern, the reduction of read-out channels is a requirement. Furthermore, a better spatial resolution can be achieved if the charge is shared between two strips and the hit position is calculated with some center of gravity algorithm, respect to the case of all the charge released in only one strip where the resolution is given as:

$$\sigma^2 = \frac{1}{p}\int_{-\frac{p}{2}}^{\frac{p}{2}} x^2 dx = \frac{p^2}{12},$$

with p the distance between two read-out strips.

Referring to the behaviour shown in Fig. 5.9, it must be considered that, at higher beam energies the charge deposited in the silicon sensor decreases. When the charge loss effect for the floating strips is taken into account, the signal measured on the cluster with multiplicity = 2 (i.e. the signal measured on the neightbouring strips of a floating strip) can be below the 3σ threshold used to consider the current strip as part of the cluster. This is the reason why no 3σ cut on the strips adjacent to a cluster seed has been used in the online software. In the zero suppression online algorithm, when a seed is found, the read-out value of the seed and its adjacent strips are always transmitted without any other check. Although this could increase the size of the HEPD data causing some fake clusters to be transmitted, the noisy flag calculated during the calibration procedure allowed an offline suppression of these events.

It must also be noted that, during the beam test, the beam was perpendicular to the silicon planes and the particles crossed a small thickness of the silicon sensor. An inclined trajectory of the incoming particle would result in a ”larger” cluster in the detector since more strips can be physically hit. For this reason, the cluster multiplicity was also studied with muon runs as reported in Fig. 5.10a and 5.10b for the *p* and *n* side, respectively.

It can be observed that the multiplicity value is always below seven; this is the reason why, in the online cluster finding algorithm, a maximum value of three adjacent strips per side can be selected as discussed in section 4.3.6.3.

In Fig. 5.11 a plot of raw ADC counts as a function of the silicon channels is reported for 70 MeV beam energy. The presence of two well separated clusters confirms the charge loss for events where a floating strip is hit. A profile along the Y axis shows two clear peaks at 50 ADC counts and 180 ADC counts: by selecting only events with multiplicity = 1 or multiplicity = 2, one of the two distributions disappears.

Before proceeding, it is useful to introduce some common terminology for silicon detectors. Let us assume a cluster is composed by one or two strips (we have seen from

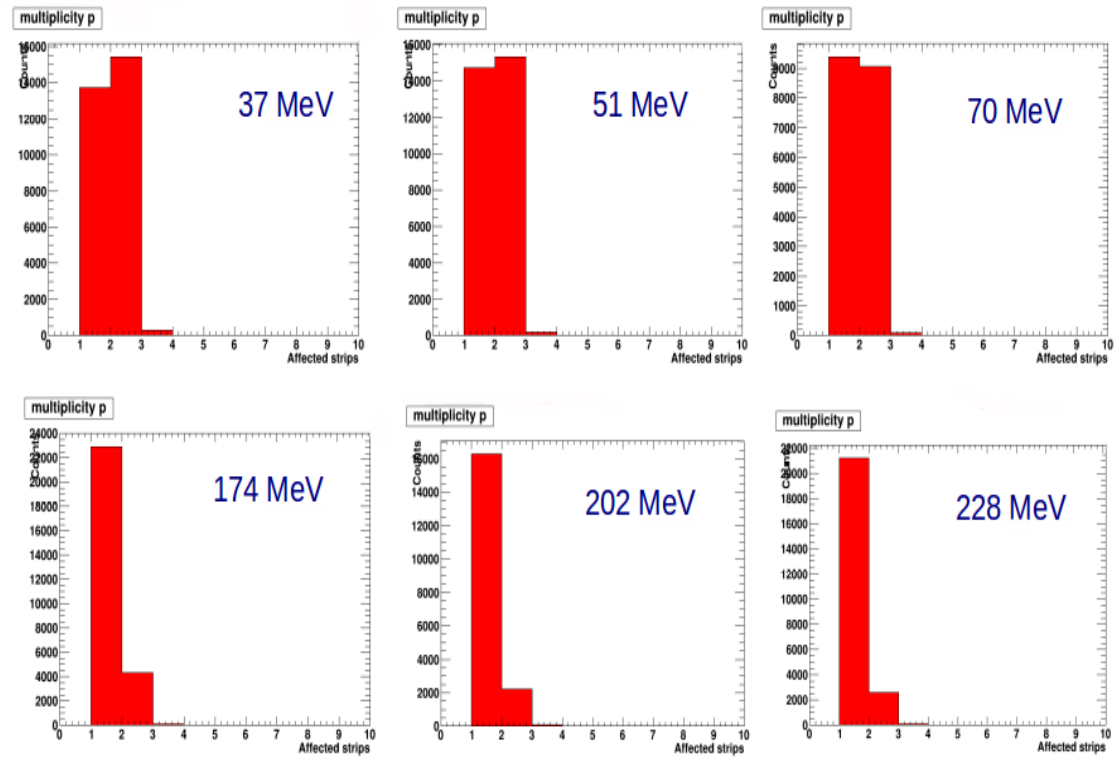

Fig. (5.9) *Variation of the cluster multiplicity for the P side of the central ladder at different beam energies.*

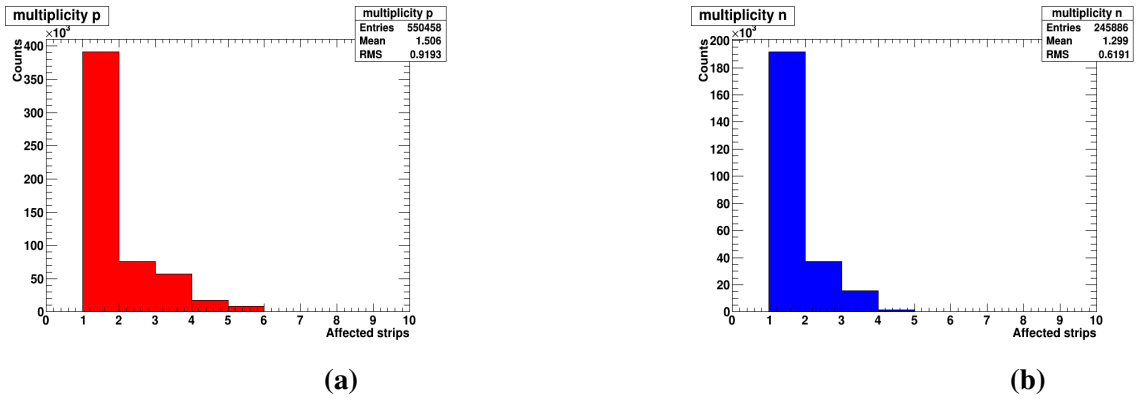

(a) **(b)**

Fig. (5.10) *Cluster multiplicity calculated with a muon run for the P view (a) and the N view (b) of the silicon detector.*

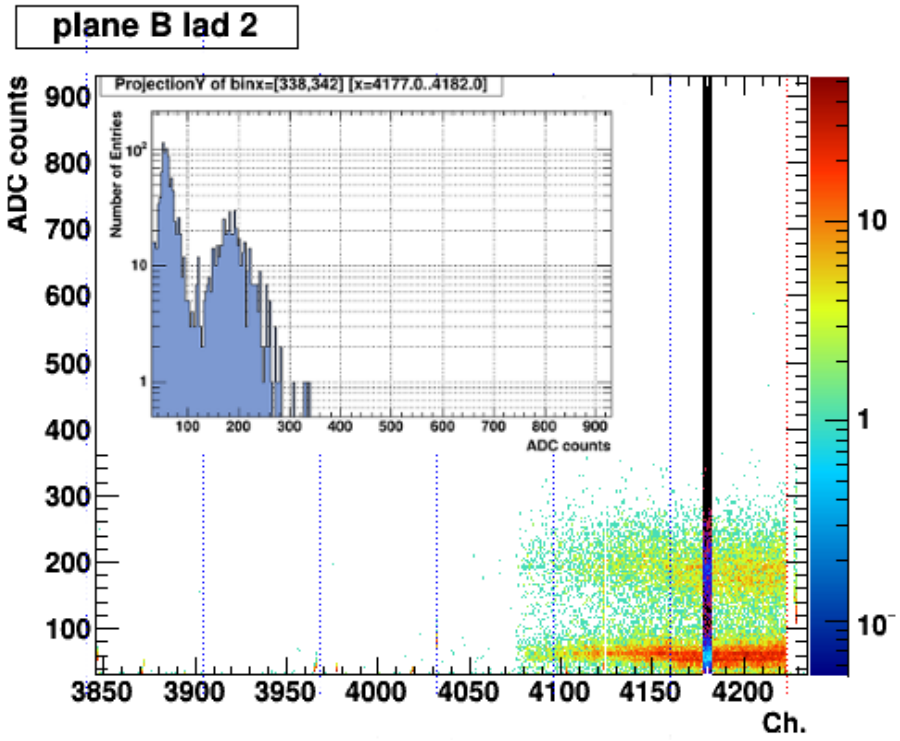

Fig. (5.11) *Raw ADC counts vs silicon channels after pedestal and common noise subtraction. Data are taken from a 70 MeV proton run on the bottom silicon ladder of the internal plane (B). The two distributions related to hits on readout strips and floating strips are clear. A projection on the Y axis shows the two peaks at* $\sim$ 50 $ADC\ counts$ *and* $\sim$ 180 $ADC\ counts$.

5.9 that is more than reasonable), we can define the η variable as:

$$\eta = \frac{S_{right}}{S_{right} + S_{left}},$$

where S is the signal relased on the strip, and right/left means the highest/lowest channel in the read-out order. It is always possible to calculate η with a multiplicity higher than two, just considering only the two strips with the highest signals. On the other hand, with a multiplicity equal to 1, there is a signal only on the seed and its two neighbouring strips will have a value close to zero. In this case, the adjacent strip with the highest value is used to calculate η, that will be 0 or 1, depending on the position of this adjacent strip with respect to the seed.

The η variable is always in the range $0 \leq \eta \leq 1$ and can be used to calculate the impact point of the incident particle as follows:

$$x = x_L + \eta \cdot p,$$

where p is the read-out pitch and x_L is the position of the left strip. This linear η algorithm generates systematic errors on the true impact point reconstruction [50], for this reason a more precise non-linear algorithm is used:

$$x = x_L + f(\eta) \cdot p,$$

where $f(\eta)$ is an arbitrary monotonic growing function of η with $f(0) = 0$ and $f(1) = 1$.

In Fig. 5.12 the η distribution measured for a HEPD silicon ladder is shown for a 36 MeV proton run. As already mentioned, the peaks at $\eta = 0$ and $\eta = 1$ refer to a situation where all the signal is collected by one strip. We expect a simmetric distribution beacause the right and left tag is only a convention. The peak around 0.5 refers to a situation where a particle crosses a floating strip and the charge is collected by the two neighbouring strips. As expected, for a detector with one floating strip between two read-out strips, the number of occurrences for the three peaks is the same, since the number of floating and read-out strips is the same.

At this point I have considered that the charge released by the passage of a particle must be independent on which strip has been hit. In particular, I have looked for a correction in order to reconstruct the total deposited charge, independently on the hit position. I have started from the assumption that, if the hit strip is a read-out strip, there is no charge loss and the ADC read-out value is the correct one.

Fig. 5.13 (a) shows a 2-dimensional histogram with the ADC count values as a function of η, for all the events of a 100 MeV proton run. Most of the events is concentrated at $\eta = 0$, $\eta = 0.5$ and $\eta = 1$.

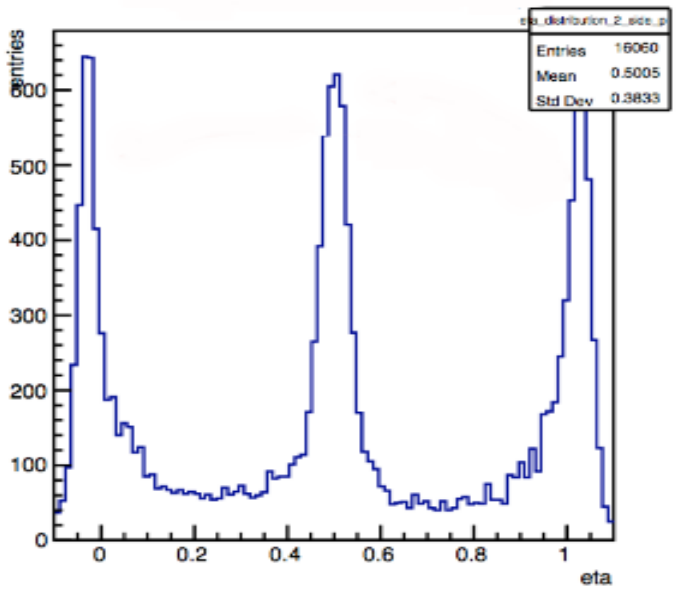

Fig. (5.12) *η distribution for the central ladder (external plane) calculated with 36 MeV protons. The distribution contains three peaks as expected for a silicon ladder with a floating strip between two read-out strips.*

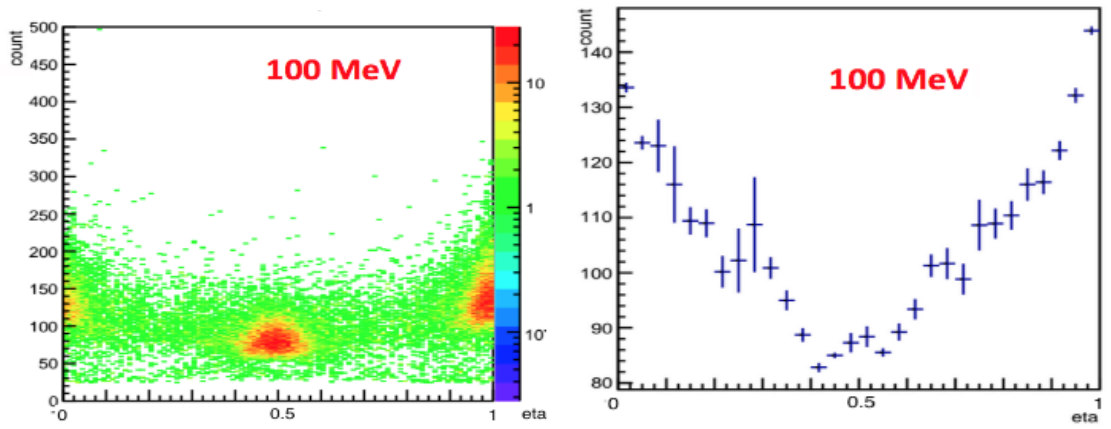

(a) **(b)**

Fig. (5.13) *(a) ADC counts vs η distribution for the central ladder (external plane) for a 100 MeV proton run. (b) Longitudinal profile of the ADC counts vs η distribution.*

A parabolic behaviour can be seen in the profile along the Y axis of the previous distribution (see Fig. 5.13 (b)).

Due to the poor statistics and the large error bars in the intermediate regions, it has been decided to consider only the most populated bins around the three peaks ([-0.1;

0.1], [0.3; 0.5], [0.5; 0.7] and [0.9; 1.1]) to perform a parabolic fit. Fig. 5.14 shows the parabolic fit obtained with the aforementioned procedure, starting from the ADC_{raw} vs η bi-dimensional distribution.

The $P(\eta)$ function obtained in such a way, shows how the charge loss depends on the incident position, and can be used to apply a correction on the raw ADC counts as follows:

$$ADC_{true} = ADC_{raw} \cdot P^{norm}(\eta), \tag{5.1}$$

where ADC_{true} is the corrected value of ADC counts, we should have without energy loss, and $P^{norm}(\eta)$ is the function as obtained from the fit after its normalization in order to satisfy:

$$P^{norm}(\eta = 1) = P^{norm}(\eta = 0) = 1, \tag{5.2}$$

since no correction is required if the hit strip is a read-out strip (I started assuming no charge loss is present in this case).

The correction effect in eq. 5.1, applied on a 36 MeV proton run, is illustrated in Fig. 5.15. The left panel (a) contains the number of entries as a function of the ADC_{raw}, measured by one silicon ladder. It is possible to see the two peaks for events with cluster multiplicity = 1 and 2. The right panel (b) shows the same plot after that, event by event, the raw cluster signal has been corrected with the corresponding $P^{norm}(\eta)$ function. It can be noted that the second peak at $\sim$ 180 ADC counts disappears after the correction is applied. The final resulting peak in (b) has been fitted with a Landau distribution, in order to obtain the mean value for the measured ADC counts ($< ADC >_{true}$) at that energy.

All these steps have been repeated for all the beam energies and for all the ladders and views of the silicon detector, in order to estimate the correction function $P^{norm}(\eta)$ for all the sensors and for all the energies of the beam test.

To determine the ADC_{true} for each cluster signal at every energy, a calibration function is required. For this reason, a study on the variation of the $P^{norm}(\eta)$ as a function of the energy has been performed.

The parabola can be parameterized as:

$$P^{norm}(\eta) = a\eta^2 - a\eta + 1 \tag{5.3}$$

where the dependence on the incident particle energy is expressed only by the *a* free parameter. The previous equation follows once we impose the vertex coordinates $V = (\frac{1}{2}; y_v)$ and the passage through (0;1) and (1;1) points as in the equation 5.2. To study the behaviour of the *a* parameter as a function of the energy, a plot of *a* vs the $< ADC >_{true}$, reconstructed for each beam energy, has been drawn. Different functions have been used

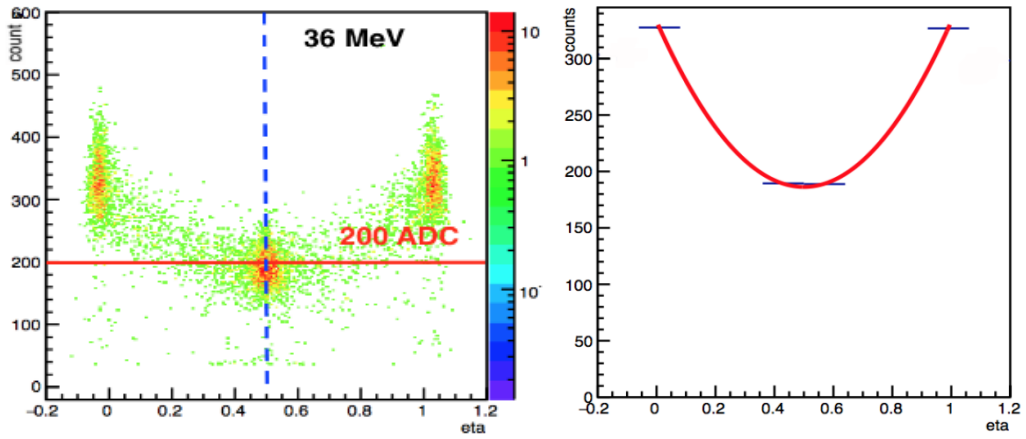

(a) **(b)**

Fig. (5.14) *(a) ADC counts vs η distribution for the central ladder (external plane) for a 36 MeV run. (b) The function $P(\eta)$ obtained with a parabolic fit of the longitudinal profile of the distribution in (a), considering only the four most populated bins.*

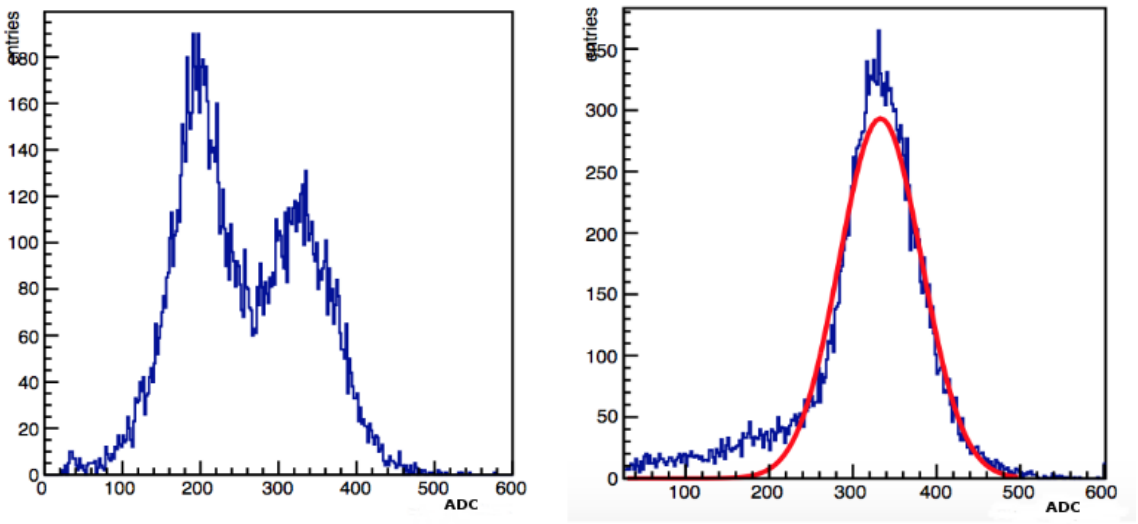

(a) **(b)**

Fig. (5.15) *(a) Number of entries vs ADC counts for the 36 MeV proton run. The two peak distribution is due to different hits on floating and read-out strips. (b) After applying the η correction the two peaks are merged into one, with the "true" number of ADC counts, independent on the hit position.*

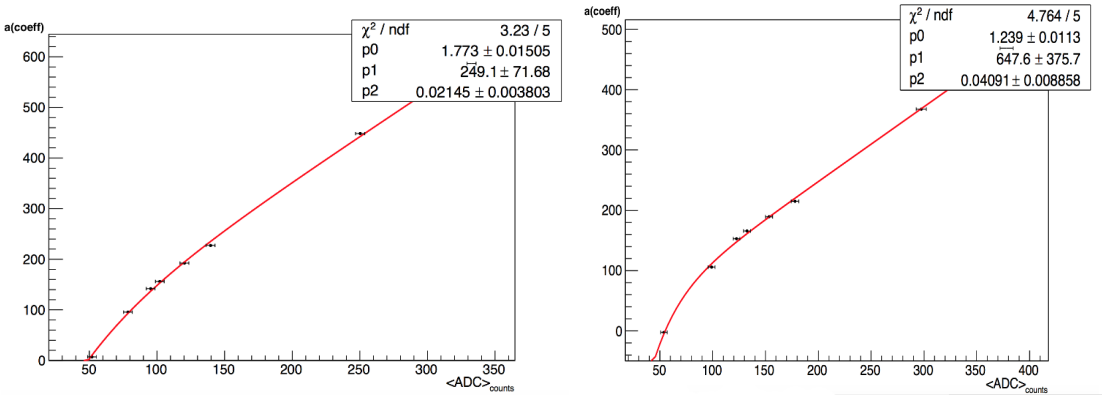

(a) **(b)**

Fig. (5.16) *η correction function for the central ladder: p side (a) and n side (b). The seven points have been obtained by calculating P^{norm} and $< ADC >_{true}$ for each beam energy.*

to fit this point distribution; among these, the function giving the best χ^2 value is the following:

$$f(x) = p0 \cdot x - p1 \cdot e^{-p3 \cdot x}. \tag{5.4}$$

The plots of *f(x)* obtained for the *p* and *n* sides of the central ladder (external plane) are shown in Fig. 5.16 (a) and (b).

Once the *f(x)* functions have been calculated for each silicon ladder, it is possible to obtain the $P(\eta)$ distribution for every possible value of the $< ADC >$ counts or, on the other hand, for every incident energy. This allows to produce a Look Up Table (LUT) that provides the ADC_{true} value, starting from the ADC_{raw} and η information for a single cluster.

The LUTs obtained for the central ladder of the external plane are illustrated in Fig. 5.17 and 5.18 for the *p* and the *n* sides, respectively. All the points along a parabola refer to the same incident energy. Given a couple of ADC_{raw} and η, the value of the true ADC counts is simply obtained from the Z coordinate of the LUT. These tables have been calculated for all the ladders, have been successfully tested and are currently used for the hit position correction.

5.2.2 Cosmic Muon Runs

The present section refers to an analysis based on cosmic rays collected between November 2016 and March 2017, in the laboratories of Rome and Beijing, during the tests of the HEPD in its final flight operation mode. At altitudes close to the sea level, the cosmic

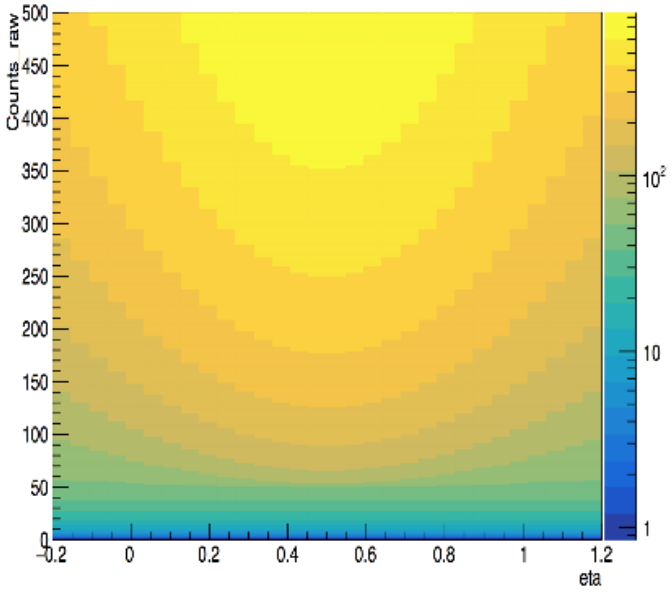

Fig. (5.17) *Look Up Table used to correct the ADC counts of a cluster, starting from the raw ADC counts and η value (p side). The value of the corrected ADC counts is obtained from the Z coordinate.*

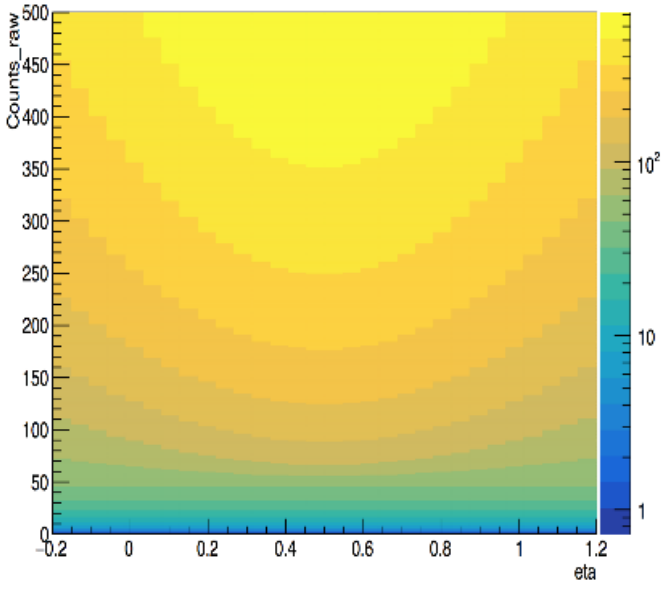

Fig. (5.18) *Look Up Table used to correct the ADC counts of a cluster, starting from the raw ADC counts and η value (n side). The value of the corrected ADC counts is obtained from the Z coordinate.*

ray flux is mostly composed of muons that can be considered minimum ionizing particles (MIPs). During these acquisitions the HEPD was always set in a vertical position, with the entrance window pointing towards the zenith, as in the thermal chamber in Fig. 5.1. It must also be noted that, in this position, the distribution of the incident direction for cosmic muons at earth is expected to cover all the acceptance window of the HEPD apparatus.

Many different combinations of high voltage, trigger configuration and discriminator thresholds have been tested during the qualification sessions of the detector, in order to verify the HEPD functioning and to find the best configuration that will be adopted in flight. The present analysis is performed on a sample of data collected after the in-flight configuration has been set.

The trigger configuration has been set to the one used in flight in the equatorial region:

$$T\&P1, \tag{5.5}$$

requiring the AND condition of the trigger plane and the first calorimeter plane. For the segmented trigger plane, the condition T requires the OR of all the 6 paddles. The generation of a trigger happens in presence of a signal from correspondence of at least one of the PMTs of each paddle/plane.

Before the acquisition run, a calibration has been calculated by means of fake trigger generation. Instead of using the previously discussed online calibration run, that provides the pedestal and σ values for each PMT, we have collected thousand events generated with these fake triggers. This procedure allows to have a more precise measurement for the pedestals since it permits to exclude those events where a muon crosses the apparatus.

5.2.2.1 Scintillator Plane Efficiency

The first study on cosmic muons has been done in order to estimate the efficiency of each calorimeter plane.

We define the efficiency of a plane as the fraction of events that can be detected, respect to the total number of events passing through it:

$$\epsilon = \frac{N}{N_{tot}}.$$

The N_{tot} number must be selected excluding the plane of which we want to calculate the efficiency. For example, to calculate the efficiency for P2 plane, a sample of vertical muons has been selected by using the information of all the other scintillator planes.

The selection cuts used for the calculation of N_{sample} are:

- a signal $> 5\sigma$ on the high gain channel of T3 OR T4;

- a signal $> 5\sigma$ on the high gain channel of P1 & P3 & P4 ... & P16;
- a signal $> 5\sigma$ on the the high gain channel of the bottom veto;
- no signal on the lateral vetoes.

With these conditions, we are pretty confident the selected muons also crossed the P2 plane of which we want to calculate the efficiency. Applying the cut

$$S_{P2} > 5\sigma_{P2}$$

to the muons on the N_{sample}, it is possible to obtain the number of particles surviving the P2 signal cut (N_{P2}) and calculate the efficiency as:

$$\epsilon_{P2} = \frac{N_{P2}}{N_{sample}}.$$

The efficiency of each scintillator plane has been calculated by this method, and is reported in Tab. 5.3. As expected, its value is always close to 1. These numbers suggest us that a 5σ threshold is always a suitable cut to discriminate the signals on the scintillator planes, since it works also with minimum ionizing particles.

To calculate the efficiency for P1 plane, that is involved in the trigger, a special run with a different trigger condition has been necessary.

5.2.2.2 Calorimeter PMT Equalization

The present section is dedicated to the description of a preliminary method I have developed, for the determination of the calorimeter PMT equalization factors, by using the stand-alone scintillator detectors.

This is the first step in order to reconstruct the energy released in each scintillator plane, starting from the raw ADC counts. This program is a part of the *event reconstruction* software, that I am currently developing in collaboration with the Limadou group, in order to produce the so called level2 data, from the raw data downlinked from the satellite. These level2 data are meant to be easily readable for data analysis, without technical knowledge requirements of the apparatus functioning. They will contain the reconstructed energy of the particle, the particle direction and some other information, such as the timing and coordinates of the satellite for each event.

The PMTs of the scintillator tower may show a different response to the same amount of deposited energy in the plane, because of a different scintillator efficiency, gain differences among the PMTs and fluctuations in the light collection. Therefore, an equalization procedure needs to be applied in the offline analysis, by studying the individual response of each PMT to the same input energy, as a MIP can be.

After the pedestal remotion, I have selected vertical central muons with the following selection criteria:

PLANE	ϵ
P1	0.999
P2	0.995
P3	1
P4	1
P5	0.984
P6	0.999
P7	0.997
P8	1
P9	1
P10	0.999
P11	1
P12	1
P13	0.996
P14	0.999
P15	0.997
P16	1

Table (5.3) *MIP passage efficiency of each calorimeter scintillator plane.*

- a signal $> 5\sigma$ on T3 OR T4 (the central trigger paddles);
- a signal $> 5\sigma$ on L5 (the central LYSO crystal);
- no signal on the other LYSO crystals;
- a signal $> 5\sigma$ on the bottom veto;
- no signal on the lateral vetoes.

By selecting central muons in this way, we expect that the two PMTs placed at the opposite corners of each plane, will see approximately the same number of photons. Acquiring a large number of events, we expect a similar distribution for the signals measured on both PMTs. A difference on those signals will be due to a different PMT gain.

The MIP energy distribution for each PMT is fitted with a Landau function and the most probable values are used as coefficients to weight the signal in a given PMT. The equalization coefficient K_i^{MIP} of the $i-th$ PMT has been obtained by scaling the peak to the arbitrary value of 100 ADC counts, as follows:

$$K_i^{MIP} = 100/MPV_i, \tag{5.6}$$

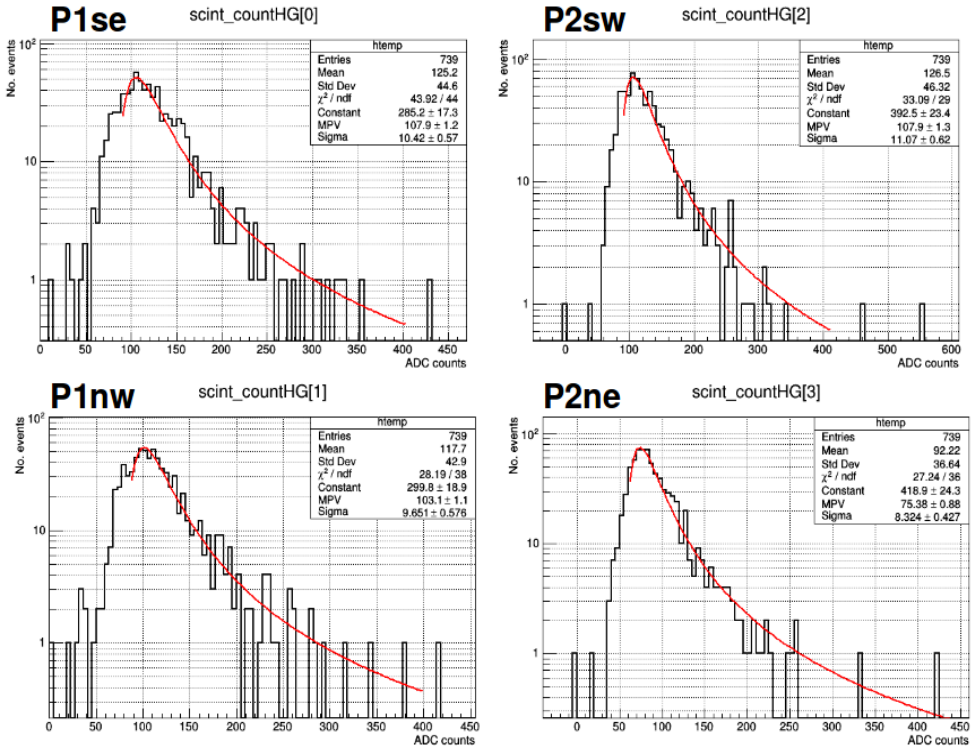

Fig. (5.19) *MIP signal distributions for the four PMTs of the first two scintillator planes. A Landau fit has been used to obtain the most probable values (MPVs) used for the determination of the equalization factors.*

where MPV_i is the most probable value obtained from the Landau fit for each distribution.

In Fig. 5.19 the distributions and the fits for the four PMTs of the first two planes are reported as example. The convention for the nomenclature of the PMTs is illustrated in the scheme in Fig. 5.20.

Using the fit results, the raw data have been equalized on event by event basis, according to the following formula:

$$S_i^{EQ} = K_i^{MIP} \cdot S_i^{RAW}, \tag{5.7}$$

where S_i^{RAW} is the raw signal measured for the PMT i, and S_i^{EQ} is the signal after applying the equalization.

A plot of the S_i^{EQ} distribution compared to the S_i^{RAW} distribution is reported in Fig. 5.21, for the same four PMTs as in Fig. 5.19. The equalized distributions are reported in blue.

In order to test the accuracy of the equalization factors, the following procedure has been applied: the muon sample has been divided into two subsamples; one selecting

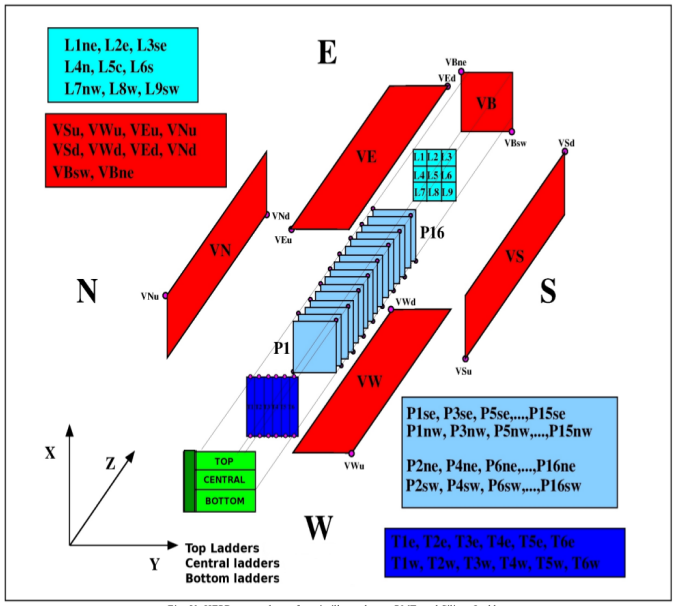

Fig. (5.20) *A scheme of the reference system for the HEPD, with coordinates and PMT nomenclature.*

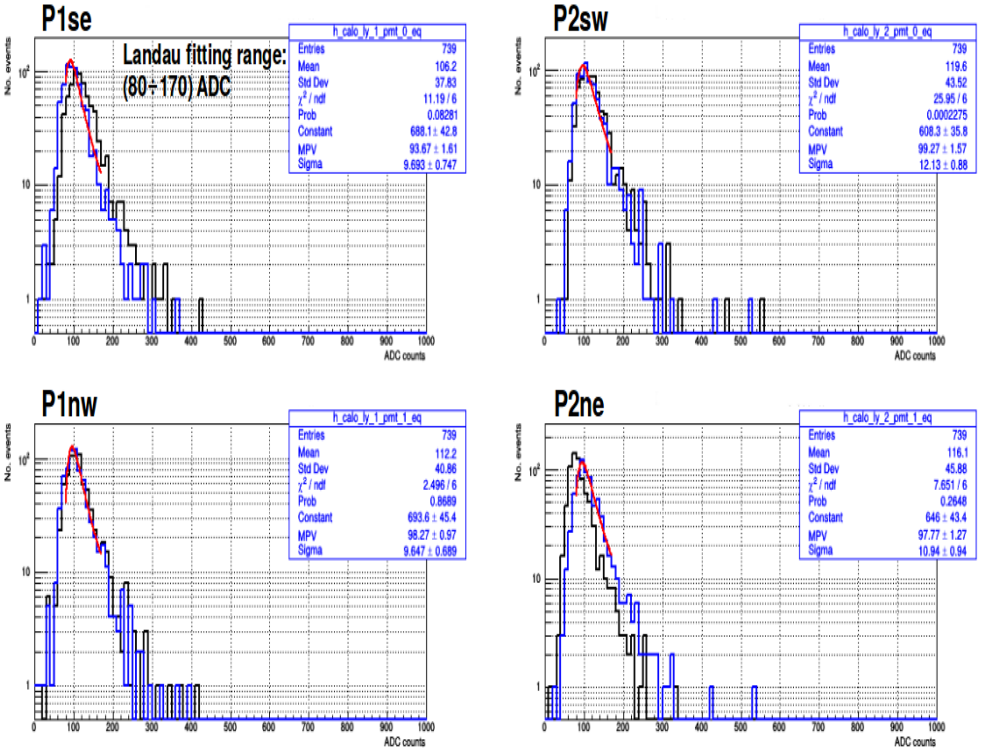

Fig. (5.21) *MIP signal distributions for the four PMTs of the first two scintillator planes, after applying the equalization procedure.*

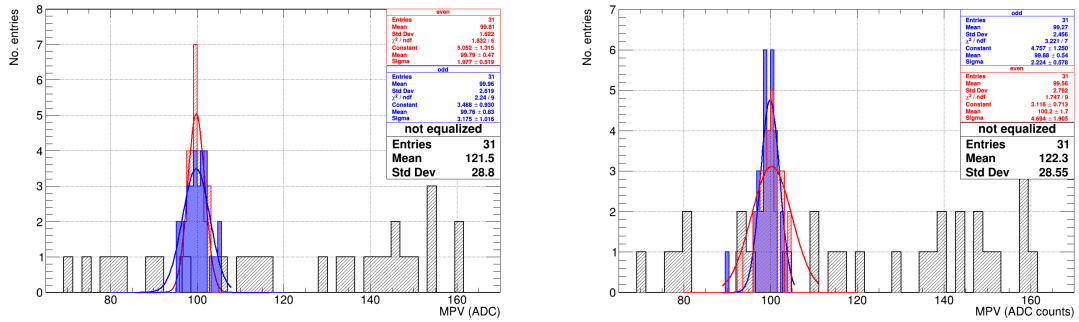

(a) *MVP distributions from the Landau fit of the not-equalized data (black) and the even (red) and odd (blue) equalized data. The even sample has been used for the equalization factor calculation (K_i^{even}).*

(b) *MVP distributions from the Landau fit of the not-equalized data (black) and the even (red) and odd (blue) equalized data. The odd sample has been used for the equalization factor calculation (K_i^{odd}).*

Fig. (5.22) *Test of the equalization procedure.*

events with an odd index and one selecting events with an even index. Then, the equalization factors have been calculated with the previously discussed method, separately on the two subsamples to acquire a couple of equalization factors K_i^{odd} and K_i^{even}.

Finally, the equalization as in eq. 5.7 has been applied four times as follows:

- K_i^{even} equalization factors applied to the "even" subsample;
- K_i^{even} equalization factors applied to the "odd" subsample;
- K_i^{odd} equalization factors applied to the "even" subsample;
- K_i^{odd} equalization factors applied to the "odd" subsample.

Again, a Landau fit has been applied for the signal distribution of each PMT, and the resulting MPVs are shown in Fig. 5.22, with respect to the not equalized ones (black). As expected, when the equalization factors are calculed and applied on the same subsample, the resulting distribution is narrower (red distribution in Fig. 5.22 (a) and blue distribution in Fig. 5.22 (b)) respect to the case of equalization factors calculated from a subsample and applied on the other one (blue distribution in Fig. 5.22 (a) and red distribution in Fig. 5.22 (b)).

The MPV distribution obtained after the equalization is centered around 100 MeV as expected. It can be noted that a broadening on the distribution is still present. This can be explained with the following consideration: we expected the energy released in a scintillator plane to be the same after selecting vertical MIPs particles, since the thickness of the crossed scintillator is the same for those muons. However, the selection cuts used to

choose vertical muons with only the calorimeter information, are not accurate. Using the central LYSO crystal and the two central paddles for the trigger allows a set of different angles for the incident particles. For this reason, the assumption of the same energy deposited for all the events is not completely correct. The equalization factors, applied event by event, produce a MPV that is centered around 100 ADC counts but with a certain spread.

This method will be improved by using the tracker impact point, in order to reconstruct the particle direction and obtain a more reliable sample of vertical muons.

Conclusions

The work accomplished in this thesis concerns the development for the control and data handling online software for the HEPD apparatus on board the CSES mission, dedicated to the study of ionospheric perturbations associated with earthquakes. A brief description of the main features of the mission and more specifically the characteristics of the HEPD have been reported in the first two chapters.

During the three years of my Ph.D., in collaboration with the CSES-Limadou team, I participated to the development of three of the four HEPD models (with the exception of the Structure and Thermal Model), as required by the Chinese space procedures, in order to test the hardware and software design of the payload, the compatibility with the satellite as well as the scientific performances.

Several months have been needed for the final assembly of the fourth version, the Flight Model (FM), of the apparatus, for the software tests and for the space qualification campaign. All the tests were successfully completed, and the software I wrote showed a high reliability, with good performances for what concerns the dead time of the data acquisition software. A good versatility is assured by the possibility to modify via tele commands almost all the parameters used during the online data processing and the possibility to update the software if some critical issues appear. The preliminary data analysis is also encouraging for what concerns the subdetectors performances and our understanding of their response.

In September 2016, the FM was delivered to China. In January, February and March 2017, I was involved, with a small group of colleagues, in the integration tests of the HEPD with the satellite at the DFH Satellite Co, Ltd. (Beijing). During these months, the thermal balance and thermal-vacuum tests with the whole satellite, including all the scientific payloads, have also been repeated. These tests have been successfully passed and our Italian payload has been accepted for the launch.

The satellite launch, initially scheduled for August 2017, has been postponed to February 2018, because of further checks on the launch system. The HEPD detector is currently in Beijing, installed on board the satellite and ready for the launch. In January 2018, the transfer of the satellite to the launch site is scheduled. I should be present at the launch site in Jiuquan, located in the Gobi Desert (Inner Mongolia region, China), for the latest

tests of our apparatus before the launch. After these final checks, CSES will be launched and the following days will be spent for the health-check activities of all the payloads and the satellite subsystems. Then a commissioning phase, lasting a period from two to four months, will begin, for a constant monitoring of the satellite and the scientific payloads during this first period after the launch. An Italian team will always be present during the commissioning to check the HEPD status.

In conclusion, during these three years, the Limadou group designed, realized and tested a perfect functioning detector. The work on the data analysis is ongoing and we are now working on the event reconstruction software, in order to provide level2 data (containing high level information such as particle energy, identification, pitch angle etc.) once the satellite will be in orbit and fully operating. For this purpose, a parallel work on the Monte Carlo data, combined with the beam test data, is under development.

Publications

Here follows a list of articles and conference proceedings, published by the author during his PhD years:

Panico B., **Palma** F., **Sotgiu** A., **2016.** " Study of the performance of the HEPD apparatus for the CSES mission". *XXV European Cosmic Ray Symposium, Turin*

Sparvoli R., **Palma** F., **Panico** B., **Sotgiu** A., **Vitale** V., **2016.** "The High Energy Particle Detector on Board of the China Seismo-Electromagnetic Satellite". *Living Planet Symposium, Proceedings of the conference held 9-13 May 2016 in Prague, Czech Republic.* **Volume** 740.

Vitale V., **Palma** F., **Sotgiu** A.,**2017.** "The High-Energy Particle Detector on board of the CSES mission". *RICAP16, 6th Roma International Conference on Astroparticle Physics, Roma* **Volume** 136.

Alfonsi L. *et al.*, **2017.** "The HEPD particle detector and the EFD electric field detector for the CSES satellite". *Radiation Physics and Chemistry* **Volume** 137.

Bibliography

[1] V. Sgrigna. ESPERIA Experiment: Phase A Report Submitted to the Italian Space Agency (ASI). *AGU Fall Meeting Abstracts*, December 2001.

[2] O. Adriani, G. C. Barbarino, G. A. Bazilevskaya, R. Bellotti, M. Boezio, E. A. Bogomolov, M. Bongi, V. Bonvicini, S. Borisov, S. Bottai, A. Bruno, F. Cafagna, D. Campana, R. Carbone, P. Carlson, M. Casolino, G. Castellini, M. P. De Pascale, C. De Santis, N. De Simone, V. Di Felice, V. Formato, A. M. Galper, L. Grishantseva, A. V. Karelin, S. V. Koldashov, S. Koldobskiy, S. Y. Krutkov, A. N. Kvashnin, A. Leonov, V. Malakhov, L. Marcelli, A. G. Mayorov, W. Menn, V. V. Mikhailov, E. Mocchiutti, A. Monaco, N. Mori, N. Nikonov, G. Osteria, F. Palma, P. Papini, M. Pearce, P. Picozza, C. Pizzolotto, M. Ricci, S. B. Ricciarini, L. Rossetto, R. Sarkar, M. Simon, R. Sparvoli, P. Spillantini, Y. I. Stozhkov, A. Vacchi, E. Vannuccini, G. Vasilyev, S. A. Voronov, Y. T. Yurkin, J. Wu, G. Zampa, N. Zampa, V. G. Zverev, M. S. Potgieter, and E. E. Vos. Time Dependence of the Proton Flux Measured by PAMELA during the 2006 July-2009 December Solar Minimum. *ApJ*, 765:91, March 2013.

[3] O. Adriani, G. C. Barbarino, G. A. Bazilevskaya, R. Bellotti, M. Boezio, E. A. Bogomolov, M. Bongi, V. Bonvicini, S. Bottai, A. Bruno, F. Cafagna, D. Campana, P. Carlson, M. Casolino, G. Castellini, C. De Donato, C. De Santis, N. De Simone, V. Di Felice, V. Formato, A. M. Galper, A. V. Karelin, S. V. Koldashov, S. Koldobskiy, S. Y. Krutkov, A. N. Kvashnin, A. Leonov, V. Malakhov, L. Marcelli, M. Martucci, A. G. Mayorov, W. Menn, M. Mergè, V. V. Mikhailov, E. Mocchiutti, A. Monaco, N. Mori, R. Munini, G. Osteria, F. Palma, B. Panico, P. Papini, M. Pearce, P. Picozza, M. Ricci, S. B. Ricciarini, R. Sarkar, V. Scotti, M. Simon, R. Sparvoli, P. Spillantini, Y. I. Stozhkov, A. Vacchi, E. Vannuccini, G. Vasilyev, S. A. Voronov, Y. T. Yurkin, G. Zampa, N. Zampa, M. S. Potgieter, and E. E. Vos. Time Dependence of the e^- Flux Measured by PAMELA during the July 2006-December 2009 Solar Minimum. *ApJ*, 810:142, September 2015.

[4] T. Zharaspayev, S. Aleksandrin, A. M. Galper, and S. Koldashov. High-energy electron bursts in the inner Earth magnetosphere caused by precipitation from radiation belt. *ArXiv e-prints*, January 2017.

[5] F. Němec, O. Santolík, M. Parrot, and J. J. Berthelier. Spacecraft observations of electromagnetic perturbations connected with seismic activity. *Geophysical Research Letters* , 35:L05109, March 2008.

[6] M. E. Aleshina, S. A. Voronov, A. M. Gal'Per, S. V. Koldashov, and L. V. Maslennikov. Correlation between earthquake epicenters and regions of high-energy particle precipitations from the radiation belt. *Cosmic Research*, 30:65–68, July 1992.

[7] A. Balogh, L. J. Lanzerotti, and S. T. Suess. *The Heliosphere through the Solar Activity Cycle*. Springer-Praxis Books and Springer Science+Business Media, 2008.

[8] A. B. Struminsky and I. V. Zimovetz. Observations of the December 6, 2006 solar flare: Electron acceleration and plasma heating. *Astronomy Letters*, 36:430–437, June 2010.

[9] O. Adriani, G. C. Barbarino, G. A. Bazilevskaya, R. Bellotti, M. Boezio, E. A. Bogomolov, L. Bonechi, M. Bongi, V. Bonvicini, S. Borisov, S. Bottai, A. Bruno, F. Cafagna, D. Campana, R. Carbone, P. Carlson, M. Casolino, G. Castellini, L. Consiglio, M. P. De Pascale, C. De Santis, N. De Simone, V. Di Felice, V. Formato, A. M. Galper, L. Grishantseva, W. Gillard, G. Jerse, A. V. Karelin, S. V. Koldashov, S. Y. Krutkov, A. N. Kvashnin, A. Leonov, V. Malakhov, L. Marcelli, A. G. Mayorov, W. Menn, V. V. Mikhailov, E. Mocchiutti, A. Monaco, N. Mori, N. Nikonov, G. Osteria, F. Palma, P. Papini, M. Pearce, P. Picozza, C. Pizzolotto, M. Ricci, S. B. Ricciarini, R. Sarkar, L. Rossetto, M. Simon, R. Sparvoli, P. Spillantini, Y. I. Stozhkov, A. Vacchi, E. Vannuccini, G. Vasilyev, S. A. Voronov, J. Wu, Y. T. Yurkin, G. Zampa, N. Zampa, and V. G. Zverev. Observations of the 2006 December 13 and 14 Solar Particle Events in the 80 MeV n^{-1}-3 GeV n^{-1} Range from Space with the PAMELA Detector. *ApJ*, 742:102, December 2011.

[10] D. Lario, A. Aran, R. Gómez-Herrero, N. Dresing, B. Heber, G. C. Ho, R. B. Decker, and E. C. Roelof. Longitudinal and Radial Dependence of Solar Energetic Particle Peak Intensities: STEREO, ACE, SOHO, GOES, and MESSENGER Observations. *ApJ*, 767:41, April 2013.

[11] S. Della Torre and AMS-02 Collaboration. Results on Solar Physics from AMS-02. *ArXiv e-prints*, December 2016.

[12] M. Storini, K. Kudela, E. G. Cordaro, and S. Massetti. Ground-level enhancements during solar cycle 23: results from SVIRCO, LOMNICKY STIT and LARC neutron monitors. *Advances in Space Research*, 35:416–420, 2005.

[13] O. Adriani, G. C. Barbarino, G. A. Bazilevskaya, R. Bellotti, and M. Boezio. Ten years of pamela in space. *La Rivista del Nuovo Cimento*, 40:473521, Sep 2017.

[14] O. Adriani, G. C. Barbarino, G. A. Bazilevskaya, R. Bellotti, M. Boezio, E. A. Bogomolov, M. Bongi, V. Bonvicini, S. Bottai, U. Bravar, A. Bruno, F. Cafagna, D. Campana, R. Carbone, P. Carlson, M. Casolino, G. Castellini, E. R. Christian, C. De Donato, G. A. de Nolfo, C. De Santis, N. De Simone, V. Di Felice, V. Formato, A. M. Galper, A. V. Karelin, S. V. Koldashov, S. Koldobskiy, S. Y. Krutkov, A. N. Kvashnin, M. Lee, A. Leonov, V. Malakhov, L. Marcelli, M. Martucci, A. G. Mayorov, W. Menn, M. Mergé, V. V. Mikhailov, E. Mocchiutti, A. Monaco, N. Mori, R. Munini, G. Osteria, F. Palma, B. Panico, P. Papini, M. Pearce, P. Picozza, M. Ricci, S. B. Ricciarini, J. M. Ryan, R. Sarkar, V. Scotti, M. Simon, R. Sparvoli, P. Spillantini, S. Stochaj, Y. I. Stozhkov, N. Thakur, A. Vacchi, E. Vannuccini, G. I. Vasilyev, S. A. Voronov, Y. T. Yurkin, G. Zampa, and N. Zampa. Pamela Measurements of Magnetospheric Effects On High Energy Solar Particles. *ApJ Letters*, 801:L3, March 2015.

[15] T. Mathews and D. Venkatesan. Unique series of increases in cosmic-ray intensity due to solar flares. *Nature*, 345:600–602, June 1990.

[16] S. E. Forbush. Cosmic-Ray Intensity Variations during Two Solar Cycles. *JGR*, 63:651–669, December 1958.

[17] O. Adriani, G. C. Barbarino, G. A. Bazilevskaya, R. Bellotti, M. Boezio, E. A. Bogomolov, M. Bongi, V. Bonvicini, S. Bottai, A. Bruno, F. Cafagna, D. Campana, P. Carlson, M. Casolino, G. Castellini, C. De Donato, G. A. de Nolfo, C. De Santis, N. De Simone, V. Di Felice, A. M. Galper, A. V. Karelin, S. V. Koldashov, S. Koldobskiy, S. Y. Krutkov, A. N. Kvashnin, A. Leonov, V. Malakhov, L. Marcelli, M. Martucci, A. G. Mayorov, W. Menn, M. Mergé, V. V. Mikhailov, E. Mocchiutti, A. Monaco, N. Mori, R. Munini, G. Osteria, F. Palma, B. Panico, P. Papini, M. Pearce, P. Picozza, M. Ricci, S. B. Ricciarini, R. Sarkar, V. Scotti, M. Simon, R. Sparvoli, P. Spillantini, Y. I. Stozhkov, A. Vacchi, E. Vannuccini, G. I. Vasilyev, S. A. Voronov, Y. T. Yurkin, G. Zampa, and N. Zampa. PAMELA's measurements of geomagnetic cutoff variations during the 14 December 2006 storm. *Space Weather*, 14:210–220, March 2016.

[18] M. S. Potgieter, E. E. Vos, M. Boezio, N. De Simone, V. Di Felice, and V. Formato. Modulation of Galactic Protons in the Heliosphere During the Unusual Solar Minimum of 2006 to 2009. *Solar Physics*, 289:391–406, January 2014.

[19] E. N. Parker. The passage of energetic charged particles through interplanetary space. *Plan. Sp. Sci.*, 13:9–49, January 1965.

[20] M. S. Potgieter. The charge-sign dependent effect in the solar modulation of cosmic rays. *Advances in Space Research*, 53:1415–1425, May 2014.

[21] J. A. van Allen and A. V. Gangnes. On the Azimuthal Asymmetry of Cosmic-Ray Intensity above the Atmosphere at the Geomagnetic Equator. *Physical Review*, 79:51–53, July 1950.

[22] S. B. Treiman. The Cosmic-Ray Albedo. *Physical Review*, 91:957–959, August 1953.

[23] J. Moritz. Energetic protons at low equatorial altitudes. *Zeitschrift fur Geophysik*, 38:701–717, 1972.

[24] J. Alcaraz, D. Alvisi, B. Alpat, G. Ambrosi, H. Anderhub, L. Ao, A. Arefiev, P. Azzarello, E. Babucci, L. Baldini, M. Basile, D. Barancourt, F. Barao, G. Barbier, G. Barreira, R. Battiston, R. Becker, U. Becker, L. Bellagamba, P. Béné, J. Berdugo, P. Berges, B. Bertucci, A. Biland, S. Bizzaglia, S. Blasko, G. Boella, M. Boschini, M. Bourquin, G. Bruni, M. Buenerd, J. D. Burger, W. J. Burger, X. D. Cai, R. Cavalletti, C. Camps, P. Cannarsa, M. Capell, D. Casadei, J. Casaus, G. Castellini, Y. H. Chang, H. F. Chen, H. S. Chen, Z. G. Chen, N. A. Chernoplekov, A. Chiarini, T. H. Chiueh, Y. L. Chuang, F. Cindolo, V. Commichau, A. Contin, A. Cotta-Ramusino, P. Crespo, M. Cristinziani, J. P. da Cunha, T. S. Dai, J. D. Deus, N. Dinu, L. Djambazov, I. D'Antone, Z. R. Dong, P. Emonet, J. Engelberg, F. J. Eppling, T. Eronen, G. Esposito, P. Extermann, J. Favier, C. C. Feng, E. Fiandrini, F. Finelli, P. H. Fisher, R. Flaminio, G. Fluegge, N. Fouque, Y. Galaktionov, M. Gervasi, P. Giusti, D. Grandi, W. Q. Gu, K. Hangarter, A. Hasan, V. Hermel, H. Hofer, M. A. Huang, W. Hungerford, M. Ionica, R. Ionica, M. Jongmanns, K. Karlamaa, W. Karpinski, G. Kenney, J. Kenny, W. Kim, A. Klimentov, R. Kossakowski, V. Koutsenko, G. Laborie, T. Laitinen, G. Lamanna, G. Laurenti, A. Lebedev, S. C. Lee, G. Levi, P. Levtchenko, C. L. Liu, H. T. Liu, M. Lolli, I. Lopes, G. Lu, Y. S. Lu, K. Lübelsmeyer, D. Luckey, W. Lustermann, C. Maña, A. Margotti, F. Massera, F. Mayet, R. R. McNeil, B. Meillon, M. Menichelli, F. Mezzanotte, R. Mezzenga, A. Mihul, G. Molinari, A. Mourao, A. Mujunen, F. Palmonari, G. Pancaldi, A. Papi,

I. H. Park, M. Pauluzzi, F. Pauss, E. Perrin, A. Pesci, A. Pevsner, R. Pilastrini, M. Pimenta, V. Plyaskin, V. Pojidaev, H. Postema, V. Postolache, E. Prati, N. Produit, P. G. Rancoita, D. Rapin, F. Raupach, S. Recupero, D. Ren, Z. Ren, M. Ribordy, J. P. Richeux, E. Riihonen, J. Ritakari, U. Roeser, C. Roissin, R. Sagdeev, D. Santos, G. Sartorelli, A. Schultz von Dratzig, G. Schwering, E. S. Seo, V. Shoutko, E. Shoumilov, R. Siedling, D. Son, T. Song, M. Steuer, G. S. Sun, H. Suter, X. W. Tang, S. C. C. Ting, S. M. Ting, M. Tornikoski, G. Torromeo, J. Torsti, J. Trümper, J. Ulbricht, S. Urpo, I. Usoskin, E. Valtonen, J. Vandenhirtz, F. Velcea, E. Velikhov, B. Verlaat, I. Vetlitsky, F. Vezzu, J. P. Vialle, G. Viertel, D. Vité, H. Von Gunten, S. Waldmeier Wicki, W. Wallraff, B. C. Wang, J. Z. Wang, Y. H. Wang, K. Wiik, C. Williams, S. X. Wu, P. C. Xia, J. L. Yan, L. G. Yan, C. G. Yang, M. Yang, S. W. Ye, P. Yeh, Z. Z. Xu, H. Y. Zhang, Z. P. Zhang, D. X. Zhao, G. Y. Zhu, W. Z. Zhu, H. L. Zhuang, and A. Zichichi. Protons in near earth orbit. *Physics Letters B*, 472:215–226, January 2000.

[25] O. Adriani, G. C. Barbarino, G. A. Bazilevskaya, R. Bellotti, M. Boezio, E. A. Bogomolov, M. Bongi, V. Bonvicini, S. Bottai, A. Bruno, F. Cafagna, D. Campana, P. Carlson, M. Casolino, G. Castellini, C. de Donato, C. De Santis, N. De Simone, V. Di Felice, V. Formato, A. M. Galper, A. V. Karelin, S. V. Koldashov, S. Koldobskiy, S. Y. Krutkov, A. N. Kvashnin, A. Leonov, V. Malakhov, L. Marcelli, M. Martucci, A. G. Mayorov, W. Menn, M. Mergé, V. V. Mikhailov, E. Mocchiutti, A. Monaco, N. Mori, R. Munini, G. Osteria, F. Palma, B. Panico, P. Papini, M. Pearce, P. Picozza, M. Ricci, S. B. Ricciarini, R. Sarkar, V. Scotti, M. Simon, R. Sparvoli, P. Spillantini, Y. I. Stozhkov, A. Vacchi, E. Vannuccini, G. I. Vasilyev, S. A. Voronov, Y. T. Yurkin, G. Zampa, and N. Zampa. Reentrant albedo proton fluxes measured by the PAMELA experiment. *Journal of Geophysical Research (Space Physics)*, 120:3728–3738, May 2015.

[26] V. Sgrigna, L. Carota, L. Conti, M. Corsi, A. M. Galper, S. V. Koldashov, A. M. Murashov, P. Picozza, R. Scrimaglio, and L. Stagni. Correlations between earthquakes and anomalous particle bursts from SAMPEX/PET satellite observations. *Journal of Atmospheric and Solar-Terrestrial Physics*, 67:1448–1462, October 2005.

[27] S.A. Voronov. Maria-2 charged particle magnetic spectrometer. *Pribory i Tekhnika Ehksperimenta*, 1991.

[28] V. V. Akimov, V. M. Balebanov, A. S. Belousov, I. D. Blokhintsev, G. V. Veselova, M. B. Dobrijan, L. F. Kalinkin, S. V. Kovalenko, V. D. Kozlov, N. G. Leikov, N. K. Mordvov, Y. I. Nagornih, V. E. Nesterov, O. F. Prilutsky, V. L. Prohin, V. G. Rodin,

S. R. Tabaldiev, V. N. Chuprov, V. I. Fuks, I. A. Gerasimov, V. S. Ovtchinnikov, V. P. Poluektov, A. V. Serov, V. Y. Tugaenko, L. V. Kurnosova, M. A. Rusakovich, N. P. Topchiev, M. I. Fradkin, I. F. Bugakov, G. M. Gorodinsky, E. I. Chuikin, S. A. Voronov, A. M. Galper, V. A. Grigoriev, M. V. Guzenko, V. G. Kirillov-Ugriumov, S. V. Koldashov, M. G. Korotkov, B. I. Luchkov, A. A. Moiseev, Yu. V. Ozerov, A. V. Popov, V. A. Rud'ko, M. F. Runtso, B. Yu. Chesnokov, B. Agrinier, A. Bouere, M. Gros, J. P. Leray, A. Leconte, P. Masse, B. Mougin, P. Keirle, J. Cretolle, J. Paul, A. Raviart, B. Parlier, M. Poiviller, C. Hugot, F. Soroka, G. Serra, A. R. Bazer-Bachi, C. Doulade, J. Ducros, G. Vedrenne, F. Cotin, Y. M. Lavigne, P. Mandrou, E. Orsal, M. Avignon, J. Durand, J. Joli, F. Gardon, J. Mouli, M. Nobileau, and D. Fournier. The gamma-ray telescope gamma-1. *Space Science Reviews*, 49(1):111–124, Jan 1989.

[29] D. N. Baker, G. M. Mason, O. Figueroa, G. Colon, J. G. Watzin, and R. M. Aleman. An overview of the Solar, Anomalous, and Magnetospheric Particle Explorer (SAMPEX) mission. *IEEE Transactions on Geoscience and Remote Sensing*, 31:531–541, May 1993.

[30] M. Parrot. The micro-satellite Demeter. In J.-P. Paillé, editor, *35th COSPAR Scientific Assembly*, volume 35 of *COSPAR Meeting*, page 652, 2004.

[31] S. Bhattacharya. Investigation of seismo-electromagnetic precursors by data analysis from low earth orbiting DEMETER satellite. In *37th COSPAR Scientific Assembly*, volume 37 of *COSPAR Meeting*, page 275, 2008.

[32] S. A. Pulinets, A. N. Kotsarenko, L. Ciraolo, and I. A. Pulinets. Special case of ionospheric day-to-day variability associated with earthquake preparation. *Advances in Space Research*, 39:970–977, 2007.

[33] Aurora Buzzi. *DEMETER Satellite Data Analysis of Seismo-Electromagnetic Signals*. Doctorate thesis, Roma Tre University of Rome.

[34] V. Sgrigna, L. Carota, L. Conti, M. Corsi, A. M. Galper, S. V. Koldashov, A. M. Murashov, P. Picozza, R. Scrimaglio, and L. Stagni. Correlations between earthquakes and anomalous particle bursts from SAMPEX/PET satellite observations. *Journal of Atmospheric and Solar-Terrestrial Physics*, 67:1448–1462, October 2005.

[35] Roberto Battiston and Vincenzo Vitale. First evidence for correlations between electron fluxes measured by noaa-poes satellites and large seismic events. *Nuclear Physics B - Proceedings Supplements*, 243-244(Supplement C):249 – 257, 2013.

Proceedings of the IV International Conference on Particle and Fundamental Physics in Space.

[36] R. Sparvoli and CSES/HEPD Collaboration. The High Energy Particle Detector on board the CSES China Seismo-Electromagnetic satellite. In *34th International Cosmic Ray Conference (ICRC2015)*, volume 34 of *International Cosmic Ray Conference*, page 567, July 2015.

[37] G Hall. Semiconductor particle tracking detectors. *Reports on Progress in Physics*, 57(5):481, 1994.

[38] Fondazione bruno kessler. https://www.fbk.eu/it/.

[39] Eljen technology. http://www.eljentechnology.com/.

[40] Hamamatsu. https://www.hamamatsu.com/us/en/index.html.

[41] R. Sparvoli, F. Palma, B. Panico, A. Sotgiu, and V. Vitale. The High Energy Particle Detector on Board of the China Seismo-Electromagnetic Satellite. In *Living Planet Symposium*, volume 740 of *ESA Special Publication*, page 315, August 2016.

[42] Serms facility. https://www.sermssrl.com/.

[43] Z. Fei, F. Rui-Rui, P. Wen-Xi, D. Yi-Fan, G. Ke, L. Xiao-Hua, L. Ya-Qing, and W. Huan-Yu. Readout electronics of silicon detectors used in space cosmic-ray charges measurement. *ArXiv e-prints*, July 2013.

[44] Ideas site. http://ideas.no/.

[45] Neat company site. http://www.neat.it/NEAT_EN/index.php.

[46] O. Adriani, G. C. Barbarino, G. A. Bazilevskaya, R. Bellotti, M. Boezio, E. A. Bogomolov, M. Bongi, V. Bonvicini, S. Bottai, A. Bruno, F. Cafagna, D. Campana, R. Carbone, P. Carlson, M. Casolino, G. Castellini, M. P. De Pascale, C. De Santis, N. De Simone, V. Di Felice, V. Formato, A. M. Galper, U. Giaccari, A. V. Karelin, M. D. Kheymits, S. V. Koldashov, S. Koldobskiy, S. Y. Krut'kov, A. N. Kvashnin, A. Leonov, V. Malakhov, L. Marcelli, M. Martucci, A. G. Mayorov, W. Menn, V. V. Mikhailov, E. Mocchiutti, A. Monaco, N. Mori, R. Munini, N. Nikonov, G. Osteria, P. Papini, M. Pearce, P. Picozza, C. Pizzolotto, M. Ricci, S. B. Ricciarini, L. Rossetto, R. Sarkar, M. Simon, R. Sparvoli, P. Spillantini, Y. I. Stozhkov, A. Vacchi, E. Vannuccini, G. I. Vasilyev, S. A. Voronov, J. Wu, Y. T. Yurkin, G. Zampa, N. Zampa, and V. G. Zverev. The PAMELA Mission: Heralding a new era in precision cosmic ray physics. *Phys. Rep.*, 544:323–370, November 2014.

[47] A. S. Tanenbaum. *Computer Networks*. Prentice Hall, 1981.

[48] ASIC and FPGA design. https://www.mentor.com/products/fv/modelsim/.

[49] K. A. Olive et al. Review of Particle Physics. *Chin. Phys.*, 2014.

[50] R. Turchetta. Spatial resolution of silicon microstrip detectors. *Nuclear Instruments and Methods in Physics Research A*, 335:44–58, October 1993.